ABSTRACT

Title of Dissertation: **STRUCTURING A PROBABILISTIC MODEL FOR RELIABILITY EVALUATION OF PIPING SUBJECT TO CORROSION-FATIGUE DEGRADATION**

Mohamed Chookah Alseyabi, Doctor of Philosophy, 2009.

Dissertation directed by: Professor Mohammad Modarres

Department of Mechanical Engineering

Pipelines are susceptible to degradation over the span of their service life. Corrosion is one of the most common degradation mechanisms, but other critical mechanisms such as fatigue and creep should not be overlooked. The rate of degradation is influenced by many factors, such as material, process conditions, geometry, and location. Based on

these factors, a best estimate for the pipeline service life (reliability) can be calculated. This estimate serves as a guide for maintenance and replacement practices. After a long period of service, however, this estimate requires reevaluation due to the new evidence gathered from monitoring the conditions of the pipeline.

Several deterministic models have been proposed to estimate the reliability of pipelines. Among these models is the ASME B31G code, which is the most widely accepted method for the assessment of corroded pipelines. However, these models are highly conservative and lack the ability to estimate the true life and health of the pipeline. In addition to the limitations embedded in these deterministic models are the problems with inspection techniques and tools that may be inadequate and susceptible to error and imprecision. What is needed, therefore, is a best-estimate assessment model that estimates the true life of these pipelines and integrates the uncertainties surrounding the estimate. Hence, this dissertation proposes a probabilistic model that is capable of addressing the limitations of these models (by accounting for model uncertainties), the inspection data (by characterizing limited and uncertain evidence), and subjective proactive maintenance (by involving the decision-making process under uncertainty).

The objective of this research is to propose and validate a probabilistic model based on the underlying degradation phenomena and whose parameters are estimated from the observed field data and experimental investigations. Uncertainties about the structure of the model itself and the parameters of the model will also be characterized. The proposed model should be able to capture wider ranges of pipelines rather than only the network

ones, so that the proposed model will better represent the reality and can account for material and size variability. The existing probabilistic models sufficiently address the corrosion and fatigue mechanisms individually but are inadequate to capture mechanisms that synergistically interact. Given that capturing all degradation mechanisms would be a challenging task, the new model will address two of the most important mechanisms: pitting corrosion and fatigue-crack growth.

The field data is very limited, and the experiments required an extensive and expensive set-up before they could produce suitable results. Hence, relying primarily in the initial stage on the generic data available from the literature facilitated the construction of the empirical degradation model and provided an order-of-magnitude estimate of the parameters of the degradation model. The proposed model in it is simplest form has the capability to estimate the degradation outputs with the least parameter inputs available.

The Bayesian approach was implemented to incorporate the experimental data to further improve the proposed model and estimate the two constants' values. The proposed empirical model can be used to estimate the aging life expended, which will enable inspection and replacement strategies to be developed.

STRUCTURING A PROBABILISTIC MODEL

FOR RELIABILITY EVALUATION OF PIPING

SUBJECT TO CORROSION-FATIGUE DEGRADATION

By
Mohamed Chookah

**Dissertation Submitted to the Faculty of the Graduate School of the
University of Maryland, College Park in partial fulfillment
of the requirements for the degree of
Doctor of Philosophy
2009**

Advisory Committee:
Professor Mohammad Modarres, Chair/Advisor
Professor Ali Mosleh
Professor Mohamad Al-Sheikhly
Professor Shapour Azarm
Associate Professor Abdennour Seibi

PREFACE

A thorough review of the literature on the corrosion-fatigue degradation mechanism reveals noteworthy contributions from many researchers attempting to study the phenomenon as well as develop a physically acceptable describing model. Using this review, the current research explored the possibility of utilizing a widely acceptable model as a benchmark for our intended research. Wei's superposition model was selected for its long established studies and validations. The superposition model has the most advantageous criteria among all the stipulated models in the literature, which is simplicity. To enable probabilistic analysis, it was crucial to opt for a simple benchmark model that would assist in yielding a simple empirical model.

General fracture mechanics models combined with the superposition model provided the foundation from which to launch the computations in this research. The first stage of the computation process produced an initial spectrum for the refinery piping-defect (crack size) after assuming a set of variables sourced generically. This stage involved a large number of input variables, deterministic and distributed, that would need to be condensed to a smaller number. Rigorous attempts based on trial and error allowed us to propose a simple structure for the corrosion-fatigue degradation mechanism from the initial crack-size versus cycles-to-failure plot. A simple general empirical model with only two uncertain parameters was proposed. The model was further challenged to incorporate the pipeline's physical conditions. A correlation analysis enabled us to introduce the pipeline's physical operating parameters into the general empirical model. An updated

model integrated with the selected pipeline stressing factors was cross-checked with Wei's model to reveal satisfactory conformity. Also, the uncertainty of the two parameters in the updated empirical model now was due only to variability in the material properties.

The proposed empirical model's two parameters were estimated for carbon steel pipelines in the refineries, particularly X70 types. To perform this estimation, this research depended on the available generic data to produce enough simulations of the two parameters. However, field or experimental data were necessary to affirm the validity of the two parameters distributions. So, Bayesian approach was implemented to seek the most appropriate estimation for the two parameter distributions. The scarcity of field data, though some were gathered from UAE refineries in Ruwais and Abu Dhabi, motivated us to build a laboratory facility to conduct the necessary corrosion-fatigue experiments. Because the corrosion-fatigue tests were expensive and time-consuming, an outsource laboratory was hired as well to do the necessary experiments. The obtained experimental data was used to estimate the proposed empirical model's two parameters through the Bayesian estimations process. A simple empirical model with only two parameters that have valid distribution has been established.

To demonstrate the advantage of this research's results in the pipeline life assessment, a dry-cut calculation was carried out. The proposed empirical model, having the two parameters that account for the material variability in X70 carbon steel pipelines and epistemic uncertainty of the model, was deployed to assess the remaining life of the

pipeline probabilistically. The results of this estimation revealed a satisfactory assessment, with the expected failure falling within the expected window based on the history of X70 pipelines in this refinery. Hence, the ability of the proposed empirical model to estimate the remaining life of pipelines has been satisfactorily proven. The model will be a great aid in updating the inspection and preventive maintenance programs in the refinery.

TABLE OF CONTENTS

LIST OF TABLES

LIST OF FIGURES

LIST OF NOMENCLATURE

a	Crack size
a'	One half length of major axes of spheroid
a_f	Final crack size
a_{tr}	Transitional crack size
B	Constant bulk dissolution rate
b	One half length of minor axes of spheroid
d	Pit depth
E	Modulus of Elasticity
E_a	Activation energy
E_{pit}	Pitting potential
E_{corr}	Corrosion potential
F	Faraday's constant
F'	Geometrical or shape factor
f	Loading frequency
h	Pit depth
I_p, I_{corr}	Corrosion current
I_{po}	Pitting current coefficient
$i_\circ$	Bare surface current density
K_c	Fracture Toughness
K_{th}	Fatigue threshold stress intensity factor
K'	Effective stress intensity factor

k	Corrosion rate
L	Material resistance to cracking
M	Molecular weight
N	Number of cycles
N_{cg}	Number of cycles for corr-fatigue
N_{pit}	Number of cycles for pit growth
N_f	Total number of cycles for crack failure
n_r	Fatigue exponent
n_c	Corrosion-fatigue exponent
Q_f	Amount of charge
p_o	Gas pressure
q	Charge density
q_s	Charge density of repassivation
R	Universal gas constant
R_p	Polarization resistance
$R´$	Stress ratio
r	Radius
s	Standard Deviation
T	Absolute temperature
t	Time
t_f	Time between rupture events
$t_\circ$	Initial time
t'	Thickness of specimen

V	Volume
V_o	Initial potential
x	Defect depth
x_o	Defect depth Initiation
x_{tol}	Maximum tolerable defect depth
y	Deflection
Z	Number of electrons in oxidation
β	Geometrical or shape factor
β_a	Polarization resistance constant
β_c	Tafel constant
ε_f	Film rupture strain
$\dot{\varepsilon_f}$	Crack tip strain rate
$\Delta\varepsilon_{cT}$	Crack tip strain range
ΔK	stress intensity factor
$\Delta\sigma$	Applied stress range
θ	Surface coverage
μ	Median
η	Valence number
ρ	Density
ν	Loading frequency
σ	Stress Loading
σ'	Effective Stress
φ	Fractional area crack for pure corr-fatigue

ψ_{EAC}	Environmentally fraction of crack growth
κ_o	Reaction rate constant

CHAPTER 1

INTRODUCTION

1.1 *Background and Motivation*

Pipelines are susceptible to degradation over the span of their service life. Corrosion is one of the most common degradation mechanisms, but other critical mechanisms such as fatigue and creep should not be overlooked. The rate of degradation is influenced by many factors such as pipeline material, process conditions, geometry, and location. Based on these factors, a best estimate for the pipeline service life (reliability) can be calculated. This estimate serves as a guide for maintenance and replacement practices. After a long period of service, however, this estimate requires reevaluation in light of new evidence from inspections of the conditions of the pipeline.

A number of deterministic models have been proposed to estimate the reliability of pipelines. Among these models is the ASME B31G code [1], which is the most widely accepted method for the assessment of corroded pipelines [2]. However, these models are highly conservative and do not estimate the true life and health of the pipeline. In addition to the limitations embedded in these deterministic models are the problems with inspection techniques and with tools that may be inadequate and susceptible to error and imprecision. Hence, a best-estimate assessment of the life of these pipelines that integrates the uncertainties surrounding this estimate is needed. The objective of this research, therefore, is to propose and validate a probabilistic model based on the

underlying degradation phenomena whose parameters are estimated from the observed field data and experimental investigations. The proposed probabilistic models would be capable of addressing the limitations of these models (by accounting for model uncertainties), inspection data (by characterizing limited and uncertain evidences) and subjective proactive maintenance (involving the decision-making process under uncertainty).

Uncertainties about the structure of the model itself and parameters of the model should also be characterized by the model. The proposed model should also be able to capture wider ranges of pipelines rather than only the network ones [2-10], so that the proposed model will better represent the reality and can account for material and size variability. The existing probabilistic models sufficiently address the corrosion and fatigue mechanisms individually, but do not adequately capture mechanisms that synergistically interact. Given that capturing all degradation mechanisms would be a challenging task, the new model will address two of the most important mechanisms: corrosion/crack growth and corrosion/fatigue/crack growth.

To build the proposed model structures, its parameters must be estimated probabilistically. The probabilistic estimation requires context-specific data. This research builds the models based on (1) field data, and (2) experimental data. The expectation was that field data would be very limited and in its first stage provide an order-of-magnitude estimate of the parameters of the degradation models.

1.2 *Previous Work*

1.2.1 **Pitting Corrosion Model**

Pitting is a form of localized corrosion that takes the form of cavities on the surface of a metal. Pitting starts with the local breakdown of protective surface film. Pitting may cause the perforation of thin sections, as well as create stress concentrations that may trigger the onset of fatigue cracking or other types of corrosion. Simplistic models for the progression of pitting corrosion are widely available.

The Point Defect Model (PDM) was developed by Macdonald [11] through the concept of passive film breakdown on metals. Figure 1.1 shows the PDM concept schematically. The critical breakdown voltage along with induction time for a single breakdown site were used to devise methods for predicting pitting damage functions; for further details please see [11].

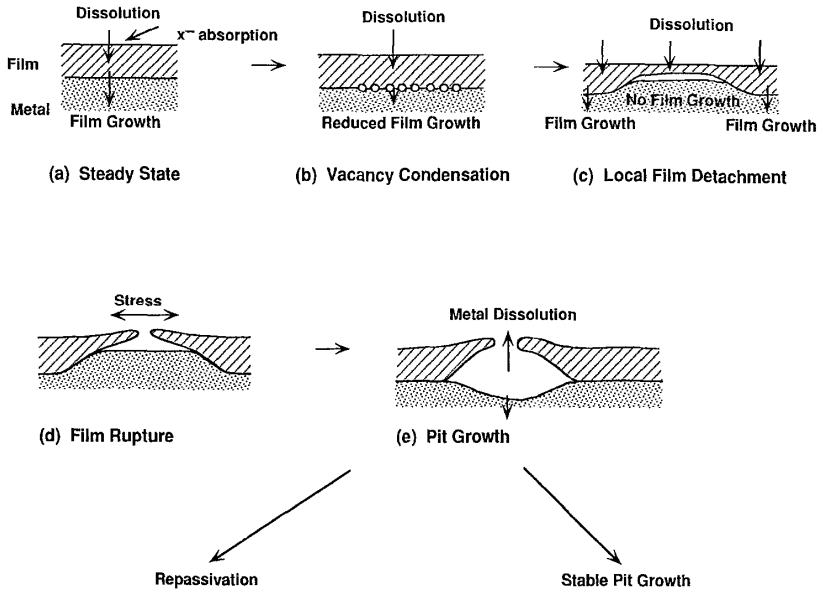

Figure 1.1. Various Stages of Pit Nucleation According to the PDM, adopted from [11].

Kondo [12] investigated the corrosion pit-growth law. By assuming a hemispherical pit, following Hoeppner [13-15], of radius r and a constant bulk dissolution rate B, he concluded that the pit volume increases proportionally to time t:

$$\left(\frac{2}{3}\right)\pi r^3 = Bt \tag{1.3}$$

And hence

$$r \propto t^{1/3} \tag{1.4}$$

Harlow & Wei [16] and Wei et. al. [17] assumed that a pit grows at a constant volumetric rate dV/dt, in keeping with Kondo [12] and Kondo and Wei [18], given by

$$\frac{dV}{dt} = \frac{MI_{p\circ}}{nF\rho} exp\left[-\frac{E_a}{RT}\right] \tag{1.5}$$

where M is the molecular weight of the material, η is the valence, F = 96514, *c/mol* is Faraday's constant, ρ is density, E_a is the activation energy, R = 8.314 *J/mol-K* is the universal gas constant, T is the absolute temperature, and Ip_o is the pitting current coefficient.

Realistically, the shape of a pit is geometrically quite complex; however, a reasonable first approximation of the shape is one half of a prolate spheroid [16] that has volume

$$V = \frac{2}{3}\pi a' b^2 \tag{1.6}$$

where *a'* and *b* are one half the lengths of the major and minor axes, respectively.
The rate of change of the volume V described by Equation (6) is given by

$$\frac{dV}{dt} = \frac{2}{3}\pi\left\{\frac{da}{dt}b^2 + 2ab\frac{db}{dt}\right\} \tag{1.7}$$

a and b are time dependent and it is assumed the growth of the pit to be dependent on the cathodic particle cluster size [16].

Turnbull et. al. [19] observed that pit-growth laws are of the form

$$x = \alpha t^{\beta} \tag{1.8}$$

He assumed that the time-dependent growth of a pit of size $x(t)$ is governed by the relation

$$\frac{dx}{dt} = g(x) \tag{1.9}$$

where g is some function of the pit size that may also be dependent on other quantities which are fixed in time such as the applied stress and temperature. So, $g(x)$ is then of the form

$$\frac{dx}{dt} = g(x) = \beta\alpha^{1/\beta}x^{1-1/\beta} \quad 1.10$$

so that $g(x)$ and the pit growth rate decreases as the pit depth increases.

Kawai and Kasai [20] empirically estimated the pit depth to be

$$h = b \cdot t^n \quad 1.11$$

where h = pit depth, t = time, and b, n = parameters related to material-environment systems [21]. The value of n is nearly constant (n = 0.3-0.5), while b changes widely depending on the material-environmental system. Little information on b is available, but would be best determined by field data. Hence, Kawai and Kasai [22] used extreme-value statics as a useful tool to predict the maximum pit depth at which a corrosion-fatigue crack propagates.

These nucleation and growth models developed by key researchers in this field of study are a just summary of a review of the attainable material. Nevertheless, the literature contribution for pit nucleation and growth modeling is not quite as extensive as it should be due to many factors such as

- Non-uniform shape of the pit.
- Non-stable shape as pit grows.

- Difficulties in defining dimensions of the pit.
- Environmental dynamics that leave the pit-modeling dilemma unsolvable without making some relaxing assumptions, which in turn result in over/under-estimations.

The challenge of modeling pit nucleation and growth is the driving factor in recent and future studies in this field.

1.2.2 **Fatigue Crack Growth Model**

One of the aims in fatigue design is to develop reliable models for characterizing the fatigue crack growth rate (da/dN, where a is crack length and N is the number of cycles of remote cyclic loading applied to the crack), by using proper loading parameters. The fatigue crack growth rate should be able to quantify the intrinsic resistance of the material under different conditions of applied stresses and specimen geometries [23]. Many attempts have been made to characterize the fatigue crack growth in terms of certain combinations of the applied stress range $\Delta\sigma$ and the crack length a, with expressions of the form,

$$\frac{da}{dN} \propto \sigma^p a^q \qquad 1.12$$

where p and q are empirical constants [24]. With the advent of fracture mechanics, more reliable methods became available in the 1960s [25-26].

When the plastic deformation zone ahead of the advancing fatigue crack resulting from the fatigue stresses applied to a component is very small compared to the otherwise

elastic field, linear elastic fracture mechanics solutions provide appropriate continuum descriptions for fatigue fracture. Paris, Gomez and Anderson [25-26] suggested that for a cyclic variation of the imposed stress field, the linear elastic fracture mechanics characterization of the rate of fatigue crack growth should be based on the stress intensity factor range

$$\Delta K = K_{max} - K_{min} \tag{1.13}$$

where K_{max} and K_{min} are the maximum and minimum values, respectively, of the stress intensity factor during a fatigue stress cycle. For any crack configuration,

$$K_{max} = F'\sigma_{max}\sqrt{\pi a} \tag{1.14}$$

$$K_{min} = F'\sigma_{min}\sqrt{\pi a} \tag{1.15}$$

$$\Delta K = F'\Delta\sigma\sqrt{\pi a} = F'(\sigma_{max} - \sigma_{min})\sqrt{\pi a} \tag{1.16}$$

where F' is a geometrical factor which depends upon the crack configuration, and σ_{max} and σ_{min} are the maximum and minimum values, respectively, of the remote fatigue stress during each cycle. Paris, Gomez and Anderson [25-26] showed that the fatigue crack growth rate da/dN is related to the stress intensity factor range by the power law relationship

$$\frac{da}{dN} = A(\Delta K)^p \tag{1.17}$$

where A and p are empirical constants. Equation 1.17 is called the Paris or Paris-Erdogen equation. These constants are influenced by such variables as the material

microstructure, cyclic load frequency, waveform, environment, test temperature, and stress ratio, R', which is defined as

$$R' = \frac{\sigma_{min}}{\sigma_{max}} = \frac{K_{min}}{K_{max}} \tag{1.18}$$

Paris and Erdogan [27] showed the validity of Equation 1.17 on aluminum alloys with different combinations of stress ranges and crack lengths and with different specimen geometries.

Fracture occurs as the maximum cyclic stress intensity approaches some critical value, K_c. Since $K_{max}=\Delta K/(1-R')$, Forman, Kearney, and Engle [28] expanded the simple Paris-Erdogan power law to account for this phenomenon with

$$\frac{da}{dN} = \frac{A(\Delta K)^p}{(1-R')K_c-\Delta K} \tag{1.19}$$

As more and more data generated under constant-amplitude loading at different stress ratios became available, fatigue crack growth rates came to be seen as dependent on the stress ratio. Walker [29] offered one of many ways to deal with this. To incorporate the effect of stress ratio so that all constant-amplitude data of various stress ratios may be represented by a single curve, he introduced the idea of the effective stress, σ', defined as

$$\sigma' = (1 - R')^m \sigma_{max} \tag{1.20}$$

where m is an empirical constant that is material dependent. In terms of the effective stress, the fatigue crack growth equation based on Equation 1.17 can be written as

$$\frac{da}{dN} = A\left[(1-R')\sigma_{max}\sqrt{\pi a}\right]^p$$

$$= A[(1-R')^{m-1}\Delta K]^p \qquad 1.21$$

The constant m is typically around 0.5 but varies from approximately 0.3 to nearly 1 for many materials. Decreasing values of m imply a stronger effect of R'. A value of $m=1$ has no effect on R'. In the case where $R'<0$, ΔK is set equal to K_{max}. This is because the stress intensity factor is not defined for a stress that does not open the crack.

Besides the simple Paris-Erdogan equation, researchers have developed some more sophisticated equations to fit the fatigue crack growth rate data. For example, Hall, Shah, and Engstrom [30] proposed a crack growth rate equation in the form

$$\frac{da}{dN} = A(K_{max} - K_{th})^q(\Delta K)^p \qquad 1.22$$

where K_{th} is the fatigue threshold stress intensity factor, and A, q, and p are empirical constants. Crack growth data for many materials showed the characteristics of the sigmoidal curve when da/dN vs. ΔK was plotted on the log-log chart [25-26].

Chamberlain and Modarres [31] defined K', the effective stress intensity factor, as $K' = \frac{\Delta K}{\sqrt{1-R'}}$, then material resistance to cracking, $\frac{1}{da/dN} = \frac{1}{C(K')^m} = L$, is a relationship between degradation (shown in form of cycles per unit crack growth, 1/(da/dN), where a is the crack size and N is the number of cycles. Therefore,

$$L = \frac{1}{C\left(K'\right)^m} \qquad 1.23$$

The equations mentioned above are just some examples of the fatigue crack growth rate equations that have been developed. Due to the simplicity of the Paris-Erdogan equation, it is the most frequently used expression in the analysis of fatigue crack growth for a wide spectrum of materials and fatigue test conditions.

1.2.3 **Corrosion-Fatigue Crack Growth Model**

Corrosion-fatigue is a process resulting from interactions among the environment, material microstructure, and cyclic loads as shown in Figure 1.2.

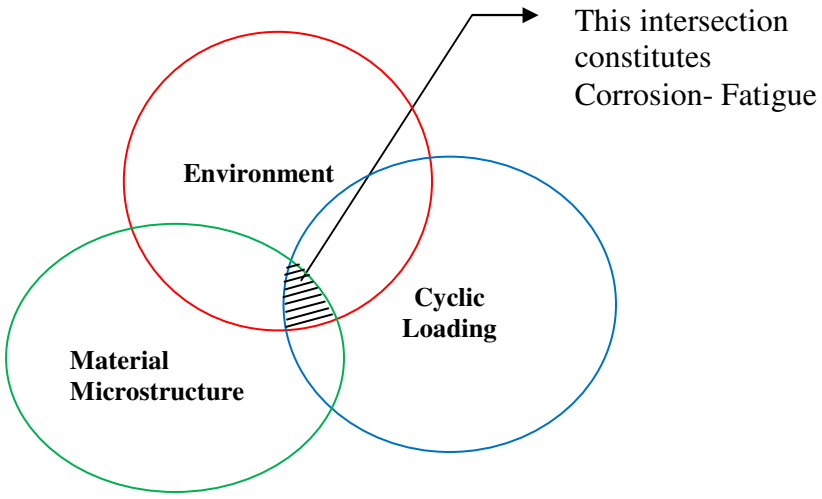

Figure 1.2. Interactions Between Three Main Elements for Corrosion-Fatigue.

While debate continues on the microscopic and atomistic details of corrosion-fatigue, and while mechanisms are often specific to each material-environment system, several common concepts have been developed over the past 25 years. The following five

qualitative descriptions of the mechanisms for corrosion-fatigue propagation were developed by Gangloff [32]:

1. Hydrogen environment embrittlement
2. Film rupture
3. Surface films
4. Adsorbed atoms
5. Anodic dissolution and plasticity

Quantitative modeling for corrosion-fatigue has been considered only for the first two quantitative mechanism descriptions, hydrogen embrittlement and film rupture, since the remaining mechanisms have not been developed quantitatively and tested experimentally. Models can successfully predict the time (frequency) dependence of corrosion-fatigue and the effects of electrode potential, solution composition and gas activity. All are, however, hindered by uncertainties associated with crack tip processes and the fundamental mechanisms of environmental embrittlement. A process zone model has not been developed for corrosion-fatigue; as such, stress intensity, yield strength and microstructure effects are not predictable. Furthermore, absolute rates of hydrogen-assisted crack growth are not predictable, and the film rupture formulation is under debate. Nevertheless, successes to date indicate that a new level of mechanistic understanding is achievable.

1.2.3.1 **Corrosion-Fatigue Modeling by Hydrogen Embrittlement**

The modeling effort should consider both mechanical and chemical influences. The mechanical factors that affect the crack growth of corrosion-fatigue include cyclic frequency, loading condition, and waveform. The chemical processes that may enhance the fatigue crack growth include [33]:

(i) Transport of the gas or gases, or electrolyte, to the crack tip;

(ii) The reactions of the gases/electrolytes with newly formed crack surfaces to evolve hydrogen (viz physical and dissociative chemical adsorption in sequence);

(iii) Hydrogen entry (or absorption);

(iv) Diffusion of hydrogen to the fracture (or embrittlement) sites;

(v) Hydrogen-metal interactions leading to embrittlement (i.e. the embrittlement sequence, or cracking).

These processes operate in sequence and represent the hydrogen embrittlement model [32-35] as shown in Figure 1.3.

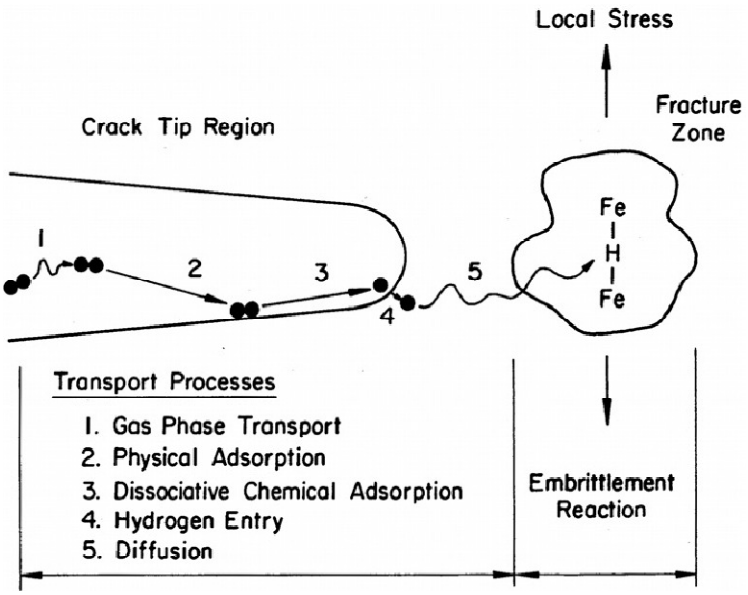

Figure 1.3. Schematic Representation of the Hydrogen Embrittlement Model [33].

The overall crack growth response depends on one or more of these processes in conjunction with the mechanical driving force for crack growth.

The actual processes depend on the mechanism of crack growth enhancement, active path dissolution or hydrogen embrittlement. For a dissolution mechanism, only the first two steps, (i) and (ii), in the sequence need to be considered, while the anodic (dissolution) reactions in the second step are directly responsible for crack growth enhancement. On the other hand, if hydrogen embrittlement is the responsible mechanism, then the reaction step serves only as the source for hydrogen. All of the remaining processes (3 through 5) must be considered.

That hydrogen embrittlement is the dominant mechanism for corrosion-fatigue has been effectively argued for several systems [32]. However, the role of hydrogen has not been directly revealed. The difficulty is the lack of probes of crack-tip chemistry, surface reactions and process zone damage.

The challenge in modeling is to derive equations that incorporate the processes shown in Figure 1.3. Quantitative hydrogen embrittlement models for corrosion-fatigue are summarized in Table 1.1.

Table 1.1. Corrosion-Fatigue Model Postulations.

Model	Postulation	Limitation/Strength
Scott [36]	Assumes that the "plateau" corrosion-fatigue crack growth rate, specifically for steels in aqueous chloride, is limited by hydrogen supply to the process zone.	This model is an extension of crack chemistry and is not based on a specific damage criterion.
Gangloff [37]	Assumes that the increment in growth rate for environment cracking, da/dN_{cf}, is proportional to the amount of hydrogen produced per loading cycle by H^+ reduction at the crack tip for steel in aqueous chloride.	The weaknesses of this model are similar to those discussed for the Scott model.
Wei et al. [38]	Relates corrosion-fatigue crack growth rate to the amount of hydrogen produced per loading cycle, which is proportionate to the extent of transient crack tip surface reaction.	The success of these models in correlating corrosion-fatigue crack growth rate data is significant.
Holroyd and Hardie [39]	Assumes that da/dN_e is determined by the extent of hydrogen diffusion, Δx, within the plastic zone and during the time of a single loading cycle. Argues that cycle-time-dependent crack growth in the aluminum-seawater system occurs by this process and at rates which are much greater than those of mechanical fatigue.	Presents no direct evidence to support the hypothesis that the growth kinetics are controlled by hydrogen diffusion.

Austin and Walker [40]	Postulates that corrosion-fatigue crack growth rates are Determined by an enhancement of the mechanical propagation rate due to hydrogen diffusion within the plastic zone and are countered by a reduction due to crack-tip blunting by corrosion. Physically, da/dN_e is equated to the mechanical fatigue rate when the extent of hydrogen diffusion spacing is less than one striation.	While the model reasonably predicts some experimental observations of corrosion-fatigue for steels in aqueous chloride, the approach is not firmly established for two reasons: (1) The basis for the model is speculative, particularly the assumption that the environmental crack growth rate equals, or may be no faster than, the maximum crack tip opening displacement scaled by that proportion of the plastic zone which is penetrated by hydrogen. (2) No evidence is provided that hydrogen diffusion occurs over a substantial portion of the plastic zone to cause discontinuous crack propagation, whose rate limits corrosion-fatigue.

A detailed discussion of each model in Table 1.1 is beyond the scope of this dissertation literature review, and readers are encouraged to consult reference [32]. However, due to its successful application and acceptance in the field of corrosion-fatigue, the superposition model by Wei et al. will be summarized.

The superposition model was first suggested by Wei and Lands [33, 41] to predict the corrosion-fatigue crack growth behavior of metals; their model was later modified by Wei and Gao [42]. This model recognizes that mechanical (or "pure") fatigue and cycle-dependent corrosion-fatigue is followed by different micro-mechanisms and occurs concurrently or in parallel, whereas the stress corrosion term is treated as a sequential contribution. The model is based on the proposition that the rate of crack growth in a

deleterious environment $(da/dN)_e$ is composed of the sum of three components given in Equation 1.25:

$$\left(\frac{da}{dN}\right)_e = \left(\frac{da}{dN}\right)_r (1-\varphi) + \left(\frac{da}{dN}\right)_c \varphi + \left(\frac{da}{dN}\right)_{scc} \quad 1.25$$

In this equation, $(da/dN)_r$ is the rate of fatigue crack growth in an inert (reference) environment and is interpreted as the mechanical fatigue (or "pure" fatigue) crack growth rate; $(da/dN)_{scc}$ is the contribution by stress corrosion cracking; $(da/dN)_c$ represents the cycle-dependent contribution which requires the interaction of fatigue and environmental attack and is identified as the "pure" corrosion-fatigue crack growth rate; and φ is the fractional area crack that is undergoing pure corrosion-fatigue. Only the cycle dependent terms are considered in this research, thus the stress corrosion cracking term is not considered, Equation 1.25 can be rewritten into the following form:

$$\left[\left(\frac{da}{dN}\right)_e - \left(\frac{da}{dN}\right)_r\right] = \left[\left(\frac{da}{dN}\right)_c - \left(\frac{da}{dN}\right)_r\right]\varphi = \left(\frac{da}{dN}\right)_{cf} \quad 1.26$$

Equation 1.26 indicates that, in the limit, for φ = 0 or for a test in a inert environment, $(da/dN)_e$ is equal to $(da/dN)_r$, which corresponds to pure fatigue. For φ = 1, $(da/dN)_e$ is equal to the maximum or "saturation" growth rate and is equal to $(da/dN)_c$, the pure corrosion-fatigue rate.

Recognizing that chemical processes occur in corrosion-fatigue crack growth, the modeling effort assumed [33] that environmental enhancement of fatigue crack growth

resulted from embrittlement by hydrogen that is produced by the reactions of hydrogenous gases with the freshly produced crack surfaces. Models for transport and surface reaction-controlled fatigue crack growth were proposed. An analogous model for electrochemical reaction-controlled crack growth has been proposed by Wei [43] for steels in aqueous environments, where the kinetics of reaction are deemed to be slow. In these models, the environmental contribution is assumed to be proportional to the extent of reaction per cycle, which is given by the fractional surface coverage θ, and the crack growth rate $(da/dN)_{cf}$, which is given as follows:

$$\left(\frac{da}{dN}\right)_{cf} = \left[\left(\frac{da}{dN}\right)_{c} - \left(\frac{da}{dN}\right)_{r}\right]\theta \qquad 1.27$$

In essence, the parameter φ in the microstructurally based model represents the material's response to changes in environmental conditions. It is directly related to its counterpart (the fractional surface coverage, θ) in chemical modeling, namely $\varphi = \theta$.

1.2.3.2 **Corrosion-Fatigue Modeling by Film Rupture**

Corrosion-fatigue modeling by film rupture is based on a sequence of passive film rupture at the crack tip, oxidation and progressive repassivation of the exposed metal, and a new rupture of the freshly formed film. The elements of this approach include crack-tip strain rate, transient metal dissolution, film formation kinetics, and film ductility. This mechanism was originally developed for stress-corrosion cracking and was extended to

corrosion-fatigue based on the common role of crack-tip strain rate [44]. Figures 1.4 and 1.5 describe the mechanism of this model.

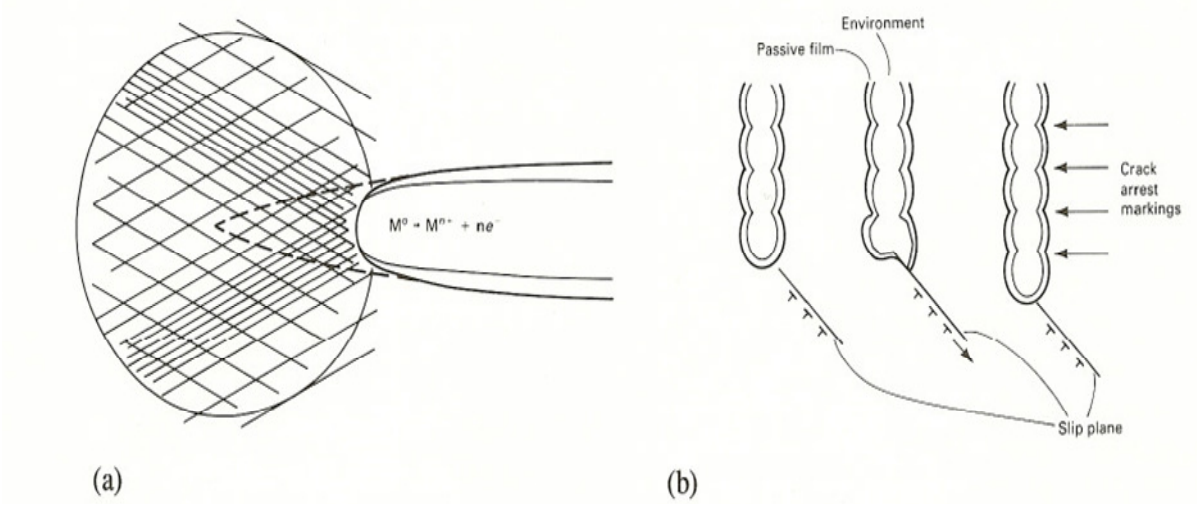

Figure 1.4. Schematic Representation of the Film Rupture Model [45]; (a) Crack tip stays bare as a result of continuous deformation [46]; (b) Crack tip passivates and is ruptured repeatedly [47, 48].

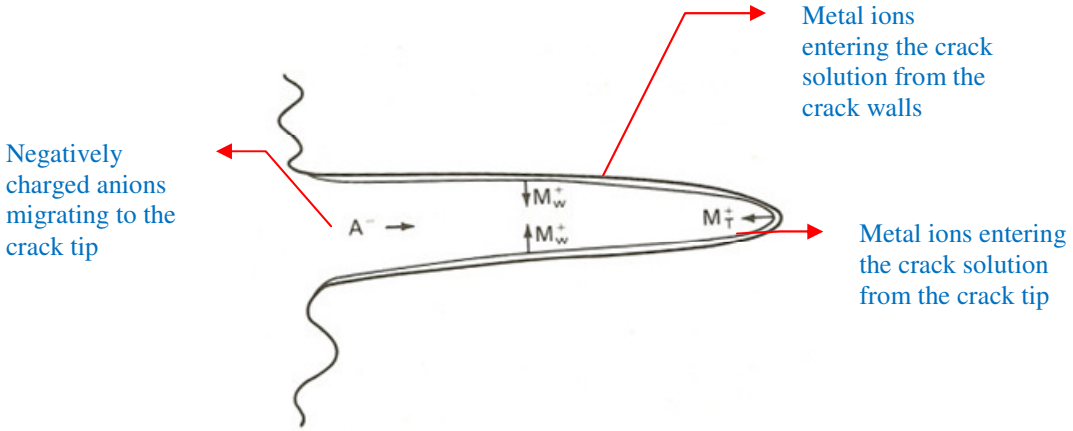

Figure 1.5. Schematic of the Thermodynamic Requirement of Simultaneous Film Formation and Oxidation [45]. The ratio of the corrosion currents from the walls relative to the crack tip is the critical parameter. This ratio must be substantially less than 1 for a crack to propagate; otherwise, the crack will blunt, or the crack-tip solution will saturate.

For corrosion-fatigue crack propagation, film rupture models are based on two equivalent relationships for per-cycle crack advance [44, 49, 50]:

$$\frac{da}{dN_{cf}} = \frac{da}{dr} \cdot \frac{dr}{dN}$$

$$= \frac{1}{f}\frac{da}{dt} \qquad 1.28$$

Where da/dr is the crack advance per film rupture plus dissolution event; dr/dN is the number of rupture events per load cycle, N; and both da/dr and da/dt are related by Faraday's law to the amount of charge Q_f.

Substituting yields the following,

$$\frac{da}{dN_{cf}} = \frac{M}{\rho ZF}\left(\frac{\Delta\varepsilon_{cT}}{\varepsilon_f}\right)\cdot Q_f$$

$$= \frac{1}{f}\left(\frac{M}{\rho ZF}\right)\cdot Q_f\left(\frac{\dot{\epsilon_c}}{\varepsilon_f}\right) \qquad 1.28$$

where $\boldsymbol{Q_f}$ is the amount of charge which passes during dissolution between rupture events; $\boldsymbol{\varepsilon_f}$ is the film rupture strain; $\boldsymbol{\dot{\varepsilon}_c}$ is the crack tip strain rate; $\boldsymbol{\Delta\varepsilon_{cT}}$ is the crack tip strain range; $\boldsymbol{M}$ and $\boldsymbol{\rho}$ are the atomic weight and density of the dissolving metal, respectively; $\boldsymbol{Z}$ is the number of electrons involved in oxidation; and $\boldsymbol{F}$ is Faraday's constant.

Charge passed per rupture event is given by:

$$\boldsymbol{Q_f = \int_0^{t_f=\varepsilon_f/\dot{\varepsilon}_c} i(t)dt} \qquad 1.29$$

where $i(t)$ is the transient current associated with dissolution during reformation of the ruptured film, and t_f is the time between rupture events.

Hudak [50] determined $i(t)$ for a straining electrode in simulated crack-tip solution; substituting yields the following:

$$\frac{da}{dN_{cf}} = \left(\frac{2Mi_o}{\rho ZF}\right)\frac{1}{f}\left(\frac{t_o}{\varepsilon_f}\right)^{1/2}\dot{\epsilon}^{1/2} \qquad 1.30$$

where $i_\circ$ is the bare surface current density at the instant of film rupture, and $t_\circ$ is the time for the initial decrease transient current.

The total environment crack growth rate is obtained by summing with an empirical result for inert environment mechanical fatigue:

$$\frac{da}{dN_e} = C(\Delta K - \Delta K_{th})^n + \left(\frac{2Mi_o}{\rho ZF}\right)\left(\frac{t_o \epsilon_o}{\varepsilon_f}\right)^{1/2} \Delta K \frac{1}{\sqrt{f}} \qquad 1.31$$

where C and n are material constants from the inert environment fatigue law, and $\varepsilon_\circ$ is a constant from the measured $(d\varepsilon/dt) - \Delta K$ relationship.

Ford and Andersen derived an analogous expression for $da/(dNe)$ [44, 51]:

$$\frac{da}{dN_e} = \frac{da}{dN_m} + \frac{1}{2f}(g(\beta)\Delta K^{\gamma\beta} f^{(\beta-1)}$$

$$= \frac{da}{dN_m} + \eta(\beta)\Delta K^{\gamma\beta} f^{(\beta-1)} \qquad 1.32$$

where $g(\beta)$ is stated generally to describe environment chemistry and metallurgical effects on corrosion-fatigue crack growth kinetics, and η is a constant.

The review by Ford and coworkers [44, 49, 51, 52] showed that film rupture quantitative expressions for crack growth rate reasonably predict the effects of ΔK, frequency,

metallurgical variables, and environment chemistry. On balance, however, controversy surrounds determinations of crack chemistry, crack-tip strain rate, the fracture behavior of a film of uncertain structure and adherence, and transient electrochemical reactions.

As stated by Gangloff [32], "Advances in our understanding of crack tip stress/strain fields, crack chemistry and crack tip transient reaction kinetics are outstanding. The challenge remains, however, to integrate these results into predictive models of corrosion-fatigue crack propagation rate by either hydrogen embrittlement or film rupture." Hence the work in this field with the advances to date and the likelihood for future refinements suggest that an in-depth mechanistic understanding of corrosion-fatigue crack propagation is at hand.

1.2.4 **Probabilistic Fatigue Crack Growth Modeling**

Many investigations in the past decade have explored the probabilistic approach in estimating the service lives of engineered components and structures operating in deleterious (or corrosive) environments. This approach was initiated to replace the more traditional approach of statistical modeling. The motives behind avoiding the statistical models, as stated by Wei et al. [53-54] are:

- They are parametric representations of experimental data.
- They do not adequately represent all of the factors that contribute to variability.
- They may have little resemblance to the failure processes under long-term operating conditions.

As such, statistical models may be suitable for making inferences over the range of available observations, but they should not be used for extrapolations beyond this range. Some examples of the many proposed statistical models can be found in [55] by Lin and Yang, [56] by Bogdanoff & Kozin, and [57] by Sheikh, Boah, & Hansen.

To overcome the shortcoming of a statistical model, a mechanistically-based probabilistic model is needed. Current fatigue-life predictions are based upon the presumption that short-time data can be extrapolated and used in predicting long-term structural performance. These extrapolations involve both size (from laboratory test specimens to structures) and time (using data collected over months to predict service lives of tens or hundreds of years). The following factors contribute to uncertainties associated with time extrapolations [54-57]: (1) uncertainties in the crack growth model; (2) statistical variations in material properties, loading and environmental conditions; (3) variability introduced through experimental conditions, and through differences in damage mechanisms at the higher stresses used in testing versus those encountered during service at the lower operating levels; and (4) long-term changes in material properties and variations in environmental conditions. Due to these factors, the current design approaches based on the use of "safety factors" and "design verification" tests cannot provide quantitative predictions of service life, along with defensible assessments of safety and reliability.

To improve the current fatigue design approaches, quantitative methods for life prediction must be developed that link a well-grounded fundamental understanding of the

underlying physical phenomena with appropriate statistical and probabilistic analysis. This understanding must be generalized and translated into a usable form through modeling of the failure mechanism in terms of the key loading, environmental and microstructural variables. It is necessary to conduct statistical analysis to identify the source of uncertainty and to quantify the contributions of key variables. Probabilistic modeling then is needed to integrate the mechanism understanding and statistical information into a methodology for life prediction and risk assessment.

Caleyo, González, and Hallen [58] proposed a probabilistic methodology for the estimation of the remaining life of pressurized pipelines containing active corrosion defects. Their reliability assessment is carried out using several already-published failure pressure failure models. A steady-state corrosion rate is assumed to estimate the growth in the dimensions of corrosion defects. The first-order, second-moment iterative reliability method; the Monte Carlo integration technique; and the first-order Taylor series expansion of the limit state function (LSF) are used to estimate the probability of failure associated with each corrosion defect over time. Further details can be found in [58].

Hall and Strutt [59] described a methodology for implementing physics-of-failure models of component lifetimes in the presence of parameter and model uncertainties. The uncertainties were treated as random variables described by some statistical distributions and were sampled using Monte Carlo methods. One of the models they used is the power-law corrosion growth (PCG) model, which represents the progressive deterioration

of oil and gas pipelines. It was shown in [60] that the growth of defects in oil pipelines arising from the corrosion process could be described by a generic power-law model of the form

$$\frac{dx}{dt} = \kappa X^q \tag{1.33}$$

where X is a dimensionless depth variable given by $= \frac{x}{x_o}$, where x is the depth of the defect at time t, and x_o is a small initiation depth triggered by an event at some time t_o. It was shown that the time-to-failure for a given set of parameters (q, κ, t_o, x_o, and x_{tol}) can be given as

$$t = t_o + \frac{x_o}{(q-1)k}\left[1 - \left(\frac{x_o}{x_{tol}}\right)^{q-1}\right] \tag{1.34}$$

where q is the growth rate exponent, k is the corrosion rate, and x_{tol} is the maximum tolerable defect depth.

A probabilistic model based was proposed by Harlow and Wei [43]. The Paris-Erdogan equation was treated as a mechanistic model, and the key variables that contributed to the failure process were identified. The model was illustrated using data on X70 steel. The influence of random variables on fatigue life was studied.

1.3 *Proposed Work*

Based on this literature review, it is apparent that there is much more need to be done to acquire further understanding of modeling corrosion-fatigue probabilistically. Hence, this research involves the following steps:

1. Adopting a degradation model for corrosion-fatigue of piping in the refining industry. This step involves investigating all the possibilities to accommodate the most relevant physics-based models that specify a great extent of the degradation process.
2. Specifying the random variables, RVs, in the adopted models. This task will be done based on data availability and justifiable assumptions (i.e., no model uncertainty).
3. Assigning appropriate prior distributions for the specified RVs; once again, this would be based on justifiable assumptions and data availability.
4. Examining the RVs for correlations with any existing physical factors that would produce a more viable distribution.
5. Based on the mechanistic (physics-based) model, proposing a simple empirical relationship between degradation and environmental conditions (degradation model).
6. Developing a routine using MATLAB to run the simulations, e.g. Monte Carlo simulations, to acquire the desired results such as the reliability of the piping.
7. Introducing a Markov Chain Monte Carlo approach for Bayesian analysis to update the parameters of the proposed degradation model based on data and evidence gathered from the field.

8. Apply the updated degradation model on some specific examples such as refinery pipelines (assuming a water-based solution medium flow as an approximation) to determine its uses in practices such as inspection and maintenance intervals.

1.4 *Contribution*

The main contributions of this research to the field are is to propose a simple empirical model that accounts for pitting corrosion as crack initiation and crack growth enhanced by corrosion in one model to be described by minimal constant variables so that it can be built with high confidence by experiment and characterized probabilistically. To achieve this core contribution, the following have been carried out:

- Integrate of the pitting contribution and the corrosion-fatigue crack growth contribution into a single empirical model that produces the total life-time of the pipeline under study.

- Propose an empirical model that is consistent with two mechanistic models of pitting and corrosion-enhanced fatigue. In essence, the proposed mechanistic models, for both pitting and crack growth were assisted by running a simulation of a benchmark model to obtain the desired outcome, such as in Figure 1.6. Subsequently, an appropriate empirical model is proposed that is consistent with the plotted data. This empirical model, having a much simpler form improved the computation accuracy (two parameters for empirical vs. several for mechanistic)

required by the adopted mechanistic models due to the large number of parameters involved.

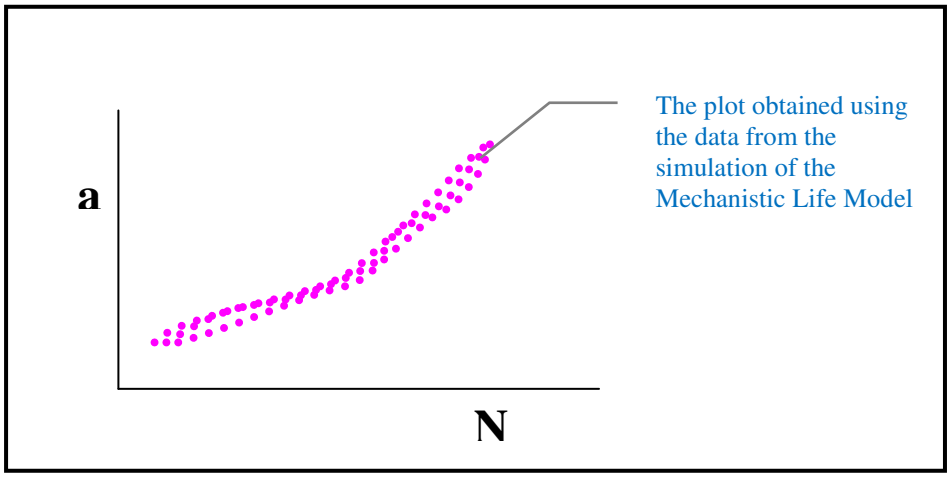

Figure 1.6. Example Plot for Crack Size vs. Number of Cycles Obtained from Simulation.

- Due to uncertainty of the crack size at transition, a_{tr}, from pitting corrosion to corrosion-fatigue crack growth, see Figure 1.7, an approach was proposed, investigated, and represented appropriately in the empirical model.

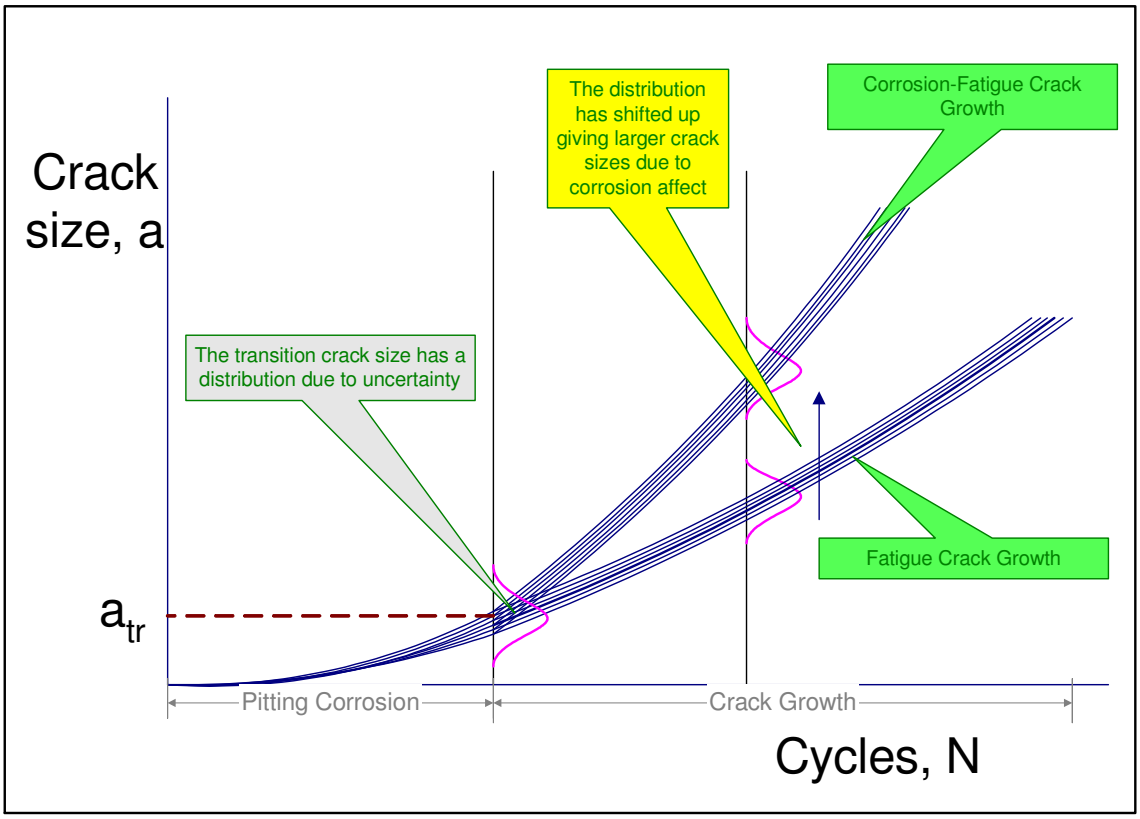

Figure 1.7. Crack Size vs. Cycles Graph Showing the Crack Size at Transition Having a Distribution.

– An experimental facility to carry out pitting corrosion and corrosion-fatigue crack growth was an essential part of this research to accurately estimate the two parameters of the proposed empirical model. State-of-the-art corrosion-fatigue testing equipment was acquired to run the experiments, which is extremely valuable, since there is a great scarcity of data in this field. The technique learned and data produced not only

helped verify and update the proposed empirical model, but it also helped initiate further research efforts in many related fields to corrosion-fatigue. For example, distribution and density of pits per unit area of materials used was estimated.

- A Bayesian probabilistic approach was adapted to estimate the distributions representing the two major uncertain parameters of the proposed empirical model. This task was achieved using both the available generic data (as prior) and the produced experimental data (as evidence).

1.5 *Objectives of Research*

The probability field has grown in recent years to become a prominent assessment tool in many industries. Because inspection and maintenance practices for pipelines in the refining industry have become obsolete and costly, they will benefit greatly from an alternative assessment tool such as the probabilistic approach.

The success of the current research depends greatly on selecting the most appropriate and practical degrading model for the pipelines in the refining industry. The literature has documented several sensible degrading models for corrosion-fatigue in pipelines. However, none has proven to be absolute, though few were found promising. The goal

here is to select a model that comprises the success factors of simplicity, validity, and solvability. The exercise of the probability tools on the selected model should not lead to computation proliferation that will hinder the research progress.

Translating the degrading model into a probabilistic one will initiate the next important step, selection of the random variables, RV. This step is a subjective decision process, and careful examination of the existing pipeline set-ups is mandatory. Field data (mechanical and operation) will also participate in selecting the most feasible RVs. Studying the correlation and dependency of these RVs might be commenced.

Validation and testing of the probabilistic model calls a valuable probabilistic tool, the Bayesian analysis. This tool aids in generating an update model that is more competent and allows for further updating as more data and evidence emerge in the future.

This research realizes the following outcomes:

- Development of a physics-based probabilistic model for the corrosion-fatigue degradation in pipelines.
- Estimation of the reliability of the pipelines under consideration.
- Verification of the competency of the adopted corrosion-fatigue degradation model.
- Utilization of the outcomes of the probabilistic model to optimize the inspection and maintenance practices.

CHAPTER 2

PHYSICS OF FAILURE

2.1 *Introduction*

Full understanding of the underlying physics-of-failure (POF) of the degradation mechanism is a fundamental step in this research endeavor. The POF approach stems out from the new practice in the research field that calls for physical models to replace the traditional statistical approaches which lacks the ability to predict beyond the ranges of the collected data. The POF models once determined could be linked with the statistical and probabilistic analysis to estimate the life and risk of pipelines subject to corrosion-fatigue degradation mechanism. Hence the corrosion-fatigue degradation mechanism need to be modeled physically along with any initiation mechanisms prior to any statistical or probabilistic analysis.

In the previous chapter, literature review has highlighted some of the significant contributors in to corrosion-fatigue degradation mechanism. This literature review has served as a selection process for pinpointing the candidate model that was proposed by examining the behavior predicted by a benchmark model. Wei's superposition model [33, 41, 42] which is based on hydrogen embrittlement concept that coincides with the main source of pipelines failures that involves hydrogen was selected to serve as the benchmark model.

In this chapter, the selected physics-of-failure benchmark model is explained. The mathematical modeling for the two major mechanisms of modeling, namely: pitting corrosion and corrosion-fatigue, is presented. The electrochemical part of the modeling is derived utilizing well-know approaches in science. The last part of this chapter focuses on proposing the corrosion current model accompanied with the details for the proofing experiment.

2.2 *Theory*

The degradation (damage) process for the crack development and propagation has been studied and modeled in many different ways [32, 53, 61]. Figure 2.1 illustrates the presumed steps for the damage process that describe how a crack develops from a pit.

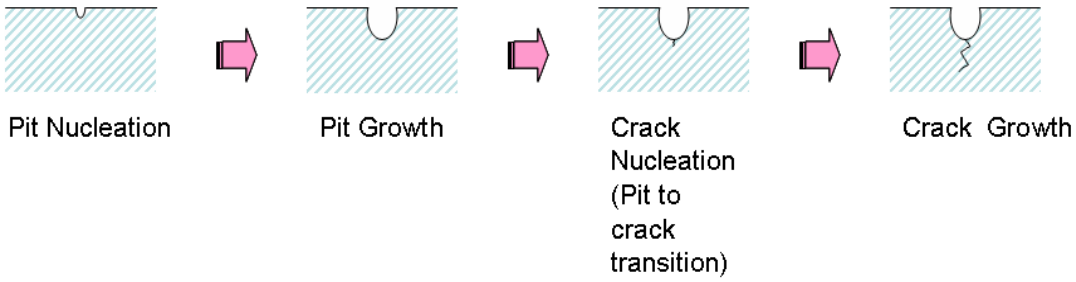

Figure 2.1. Schematic Representation of the Damage Process from Pitting to Crack Growth.

The goal of crack-development and propagation research is to develop an integrated, mechanistic description of whole-life. A sensible means to this end is to isolate and quantitatively characterize each of the four regimes of fatigue damage. This approach has been advocated because the experimental and analytical methods necessary to study each regime are different, variables may affect each regime uniquely, and many applications are dominated by one of the fatigue regimes [32].

In this research the focus will be on regimes 2 and 4, the pitting corrosion and corrosion-fatigue crack growth.

A transition from pitting to fatigue crack-growth is expected to occur when the effective $(\Delta K)_{pit}$ for the pit exceeds ΔK_{th}, and when the time-based rate of the fatigue crack-growth exceeds the rate of pit growth,

$$(\Delta K)_{pit} \geq \Delta K_{th} \quad and \quad \left(\frac{da}{dt}\right)_{crack} \geq \left(\frac{da}{dt}\right)_{pit} \tag{2.1}$$

Experimental data suggest that, in practice, transition from pitting to fatigue crack-growth is determined by the second criterion in the above equation, i.e.

$$\left(\frac{da}{dt}\right)_{crack} \geq \left(\frac{da}{dt}\right)_{pit} \tag{2.2}$$

2.2.1 **Pitting Corrosion Model**

The impact of the localized (pitting) corrosion on fatigue cracking has been recognized since the late 1920s [53]. These pits serve as the nuclei for subsequent fatigue cracking and significantly reduce the serviceable life of a component or structure [62, 63]. As such, the fatigue life of a specimen, or component, is determined by the time (or number of cycles) required to grow a pit to a sufficiently large size to effect crack nucleation (or the transition size), and by the subsequent cycles of crack growth to produce fracture.

To assess the influence of concurrent pitting corrosion, a simplified model for pit growth proposed by Harlow and Wei is used [62]. The model is patterned after that proposed by Kondo [12], and assumes a pit of hemispherical shape growing at a constant volumetric rate in accordance with Faraday's law from an initial radius a_o. The rate of pit growth (with volume $V = (2/3)\pi r^3$) is given as follows,

$$\frac{dr}{dt} = \frac{dr}{dV}\frac{dV}{dt} = \frac{1}{2\pi r^2}\frac{dV}{dt} \tag{2.3}$$

But assuming ρ is constant,

$$m = \rho V \Longrightarrow \frac{dm}{dt} = \rho\frac{dV}{dt} \Longrightarrow \frac{dV}{dt} = \frac{1}{\rho}\frac{dm}{dt} \tag{2.4}$$

From Faraday's Law,

$$m = \frac{MI_p t}{\eta F} \Longrightarrow \frac{dm}{dt} = \frac{MI_p}{\eta F} \tag{2.5}$$

Hence by substitution,

$$\frac{dr}{dt} = \frac{MI_p}{2\pi\eta\rho F}\frac{1}{r^2} \tag{2.6}$$

where,

$$I_p = I_{p_o} \cdot exp\left(-\frac{E_a}{RT}\right) \tag{2.7}$$

And r is the pit radius at time t; M is the molecular weight of metal; I_p is the pitting current; I_{po} is the pitting current coefficient; η is the metal's valence; ρ is the density of the metal; $F = 96{,}514\, C/mole$ is Faraday's constant; E_a is the activation energy; $R = 8.314\, J/mole - K$ is the universal gas constant; T is the absolute temperature.

2.2.2 **Corrosion-Fatigue Crack Growth Model**

A superposition model proposed by Wei [42] was adopted. In the most general form the fatigue crack growth rate is given by [53]:

$$\left(\frac{da}{dN}\right)_e = \left(\frac{da}{dN}\right)_{cycle} + \left(\frac{da}{dN}\right)_{time} \tag{2.8}$$

with a cycle–dependent rate and a time–dependent rate. Within each of these rates, the mechanical (deformation) and environmental contributions are treated as being from independent parallel processes.

$$\left(\frac{da}{dN}\right)_{cycle} = \left(\frac{da}{dN}\right)_r (1 - \emptyset_c) + \left(\frac{da}{dN}\right)_c \emptyset_c \tag{2.9}$$

$$\left(\frac{da}{dN}\right)_{time} = \left[\int_0^\tau \left(\frac{da}{dt}\right)_{creep} dt\right](1 - \psi_{EAC}) + \left[\int_0^\tau \left(\frac{da}{dt}\right)_{EAC} dt\right]\psi_{EAC} \tag{2.10}$$

The cycle-dependent and time-dependent rates are considered to be the weighted average of the pure-mechanical and the pure-environmental fatigue and sustained-load contributions, over one loading cycle, respectively.

The overall crack growth rate is given by:

$$\left(\frac{da}{dN}\right)_e =$$

$$\left(\frac{da}{dN}\right)_r (1 - \emptyset_c) + \left(\frac{da}{dN}\right)_c \emptyset_c + \left[\int_0^\tau \left(\frac{da}{dt}\right)_{creep} dt\right](1 - \psi_{EAC}) + \left[\int_0^\tau \left(\frac{da}{dt}\right)_{EAC} dt\right]\psi_{EAC} \quad 2.11$$

Where $(da/dN)_r$ is the pure-mechanical and $(da/dN)_c$ is the pure-corrosion-fatigue part over one loading cycle, and φ_c is the areal fraction of only pure-corrosion-fatigue. ψ_{EAC} is the areal fraction of the environmentally assisted component of crack growth rates, and the integration is taken over only one fatigue cycle and reflects the changes with K during that cycle.

In its simplest form, only the cycle-dependent part is considered, i.e. Equation 2.9. The micro-structural parameter φ_c is identified with the surface coverage θ (i.e. the fraction of a "control" area of the crack-tip surface that underwent reaction during one fatigue loading cycle; $0 < \theta < 1$). That is,

$$\left(\frac{da}{dN}\right)_e = \left(\frac{da}{dN}\right)_r + \left[\left(\frac{da}{dN}\right)_c - \left(\frac{da}{dN}\right)_r\right]\phi_c$$

$$= \left(\frac{da}{dN}\right)_r + \left[\left(\frac{da}{dN}\right)_c - \left(\frac{da}{dN}\right)_r\right]\theta \qquad 2.12$$

Based on simplified chemical modeling, the dependence of fatigue crack growth on gas pressure p_o, temperature T and fatigue loading frequency f is quantified in terms of gas phase transport, surface reaction, and hydrogen diffusion into the material ahead of the crack tip. Each of these processes operates in sequence, and the crack growth rate is controlled by the slowest process in the sequence. As such (p_o, T, f) dependence reflects on the rate-controlling chemical process and is not amenable to micro-mechanical modeling. Modeling is extended to cover electrochemical reaction-controlled crack growth in aqueous environments. The various models and experimental evidence are reviewed in [41]; in addition, in [53] they are briefly summarized as three distinct systems as follows.

2.2.2.1 **Highly Reactive Gas-Metal Systems (Transport Controlled)**

For highly reactive gas-metal systems, crack growth is controlled by the rate of transport of the gas to the crack tip, which, for molecular or Knudsen flow, the surface coverage θ is proportional to $(p_o/(f\,T^{\frac{1}{2}}))$ or proportional to $(p_o/f\,)$:

$$\theta = \theta\left(p_o, T^{1/2}, 1/f\right) \qquad 2.13$$

In practice, θ may be given as the ratio of

$$\frac{P_o}{fT^{1/2}} \Big/ \left(\frac{P_o}{fT^{1/2}}\right)_s \qquad 2.14$$

And the fatigue crack growth response is given by

$$\left(\frac{da}{dN}\right)_e = \left(\frac{da}{dN}\right)_r + \left[\left(\frac{da}{dN}\right)_c - \left(\frac{da}{dN}\right)_r\right]\left[\frac{\left(P_o/\left(fT^{1/2}\right)\right)}{\left(P_o/\left(fT^{1/2}\right)\right)_s}\right] \text{ for } \frac{P_o}{fT^{1/2}} \Big/ \left(\frac{P_o}{fT^{1/2}}\right)_s \qquad 2.15$$

$$\left(\frac{da}{dN}\right)_e = \left(\frac{da}{dN}\right)_c \text{ for } \frac{P_o}{fT^{1/2}} \geq \left(\frac{P_o}{fT^{1/2}}\right)_s \qquad 2.16$$

Where, f is the fatigue loading frequency and p_o is the gas pressure.

The parameter $[\,(p_o/(f\,T^{\frac{1}{2}}))]_s$ corresponds to the condition for maximum environmental effect, i.e. the condition under which there is sufficient time to fully react the new crack surfaces, generated by fatigue loading each cycle before the next increment of crack growth.

2.2.2.2 **Less Reactive Systems (Surface Reaction-Controlled)**

2.2.2.2.1 ***Gas-Metal Reaction System***

For less reactive systems, crack growth is controlled by the rate of surface reactions at the crack tip. For the simple first-order reactions, the surface coverage θ is given by

$$\theta = 1 - exp(-k_c p_o/f) \qquad 2.17$$

where k_c is the reaction rate constant and is temperature and activation energy dependent and given by

$$k_c = k_{co} \cdot exp(-E_a/RT) \quad 2.18$$

The crack growth response is given by the following equation:

$$\left(\frac{da}{dN}\right)_c = \left(\frac{da}{dN}\right)_r + \left[\left(\frac{da}{dN}\right)_c - \left(\frac{da}{dN}\right)_r\right]\left[1 - exp\left(\frac{k_c p_o}{f}\right)\right] \quad 2.19$$

θ is a function of

$$\theta = \theta(p_o, f, k_c(T)) \quad 2.20$$

2.2.2.2.2 ***Aqueous-Metal Reaction Systems***

For aqueous systems the crack growth response is controlled by electrochemical reaction, so that the amount of hydrogen made available per cycle is related to the amount of charge transferred by the coupled "dissolution-hydrogen reduction" couple. Similar to the gaseous case, the surface coverage θ is given by

$$\theta = \frac{q}{q_s} \quad 2.21$$

where q is the charge density associated with repassivation of the bare metal surface, and q_s is the charge density that is required to completely cover the surface.

The crack growth response is given by the following equation:

$$\left(\frac{da}{dN}\right)_e = \left(\frac{da}{dN}\right)_r + \left[\left(\frac{da}{dN}\right)_c - \left(\frac{da}{dN}\right)_r\right]\left[\frac{q}{q_s}\right] \quad 2.22$$

where, similar to the gas-metal equation,

$$\theta = 1 - exp\left(-\frac{\kappa}{\upsilon}\right) = 1 - exp\left(-\frac{\kappa_o}{\upsilon} exp\left[-\frac{E_a}{RT}\right]\right) \quad 2.23$$

$\nu = f$ = frequency

And,

$$\theta = \theta(p_o, f, k_c(T))$$

2.2.2.3 **Sufficiently rapid transport and surface reaction processes (Hydrogen diffusion controlled)**

In this case, fatigue crack growth rate is determined by the rate of hydrogen diffusion to the fracture process zone ahead of the crack tip. It is given by the following relation:

$$\left(\frac{da}{dN}\right)_e = \left(\frac{da}{dN}\right)_r + \left[\left(\frac{da}{dN}\right)_c - \left(\frac{da}{dN}\right)_r\right] = C_D\left[\frac{p_o D}{f}\right]^{1/2} \Delta K^2 \quad 2.24$$

where

$$D = D_o exp\left(-\frac{E_D}{RT}\right)$$

In Equation 2.24, C_D is an empirical constant, E_D is the activation energy for diffusion, and the model included an explicit dependence on ΔK^2.

In the refining industry, the operation mode of the pipelines is relatively slow and stable from a long-term point of view, and the flow medium is an aqueous oil product. Thus, for this research the second type of the above-mentioned systems, which is the less reactive (surface reaction controlled) aqueous-metal system, was selected; see Equation 2.22.

2.2.3 **Electrochemical Model**

For electrochemical reaction contribution, the surface coverage θ is identified with the ratio of the amount of charge transferred during each loading cycle q to that required to completely repassivate the bared surface q_s , or more conveniently,

$$\theta = \frac{q}{q_s}$$

For this purpose, a simplified model for the reaction is used. For example, it is assumed that the underlying electrochemical reaction consists of a single step and is represented by thermally activated, first-order kinetics [43, 64]. The bare surface reaction current and charge densities are represented in simple exponential forms:

$$\begin{aligned} i &= i_o exp(-kt) \\ q &= \frac{i_o}{k}\{1 - exp(-kt)\} \\ q_s &= \frac{i_o}{k} \\ k &= k_o exp\left(-\frac{E_a}{RT}\right) \end{aligned} \qquad 2.25$$

where i_o is the peak current density (initial rate of reaction on the clean [bare] surface), k is the reaction rate constant in Arrhenius form, and E_a is the activation energy. Thus,

$$\theta = 1 - exp\left(-\frac{k}{\nu}\right) = 1 - exp\left(-\frac{k_o}{\nu} exp\left[-\frac{E_a}{RT}\right]\right) \quad 2.26$$

where

$$\nu = frequency = \frac{1}{t}$$

2.2.4 **Mechanistic Model**

For mechanistic understanding of the problem, the following mechanistic model for fatigue crack growth is chosen. It is assumed that both parts of the above superposition equation can be modeled by the power law (Paris-Erdogan relationship) of the form,

$$\frac{da}{dN} = C(\Delta K)^n \quad 2.27$$

i.e.,

$$\left(\frac{da}{dN}\right)_r = C_r(\Delta K)^{n_r} \quad 2.28$$

$$\left(\frac{da}{dN}\right)_c = C_c(\Delta K)^{n_c} \quad 2.29$$

where

$$\Delta K = \beta \Delta\sigma\sqrt{(\pi a)} \quad 2.30$$

$\Delta\sigma$ is the far field stress range, and β is a geometric parameter.

The coefficients C_r and C_c reflect material properties, and the exponents n_r and n_c reflect the functional dependence of crack growth rate on the driving force ΔK.

Incorporating the electrochemical and mechanical relations yields a simple differential equation in that the variables a and N can be separated. Estimation of parameters n_r and n_c may require numerical integration [43].

The corrosion-fatigue model becomes

$$\left(\frac{da}{dN}\right) = C_r\left(F\Delta\sigma\sqrt{\pi a}\right)^{n_r}(1-\theta) + C_c\left(F\Delta\sigma\sqrt{\pi a}\right)^{n_c}\theta \qquad 2.31$$

From the solution of this equation, we can estimate the N as follows:

$$N_{cg} = \int_{a_{tr}}^{a_f} \frac{da}{C_r\left(F\Delta\sigma\sqrt{\pi a}\right)^{nr}(1-\theta)+C_c\left(F\Delta\sigma\sqrt{\pi a}\right)^{n_c}\theta} \qquad 2.32$$

where a_f and a_{tr} are the final and transitional crack sizes, respectively.

a_{tr} could be calculated iteratively using the criterion set earlier,

$$(\Delta K)_{pit} \geq \Delta K_{th} \qquad \text{and} \qquad \left(\frac{da}{dt}\right)_{crack} \geq \left(\frac{da}{dt}\right)_{pit}$$

which reflects equality between the pitting and cracking rates at the onset of crack growth,

$$\left(\frac{da}{dt}\right)_{pit} = \left(\frac{da}{dt}\right)_{crack}$$

$$\frac{MI_p}{2\pi\eta\rho F C_F f} = C(\Delta K)^n \quad 2.33$$

$$a_{tr}^2(\Delta K)^n = \frac{MI_p}{2\pi\eta\rho F C_F f}$$

$$a_{tr}^2\left(\beta\Delta\sigma\sqrt{\pi a_{tr}}\right)^n = \frac{MI_p}{2\pi\eta\rho F C_F f}$$

The fatigue life N_F is the sum of the number of loading cycles over which pitting and fatigue cracking dominates at a given stress level [53] and is given by

$$N_F = N_{pit} + N_{cg} \quad 2.34$$

2.2.5 **Corrosion Current (I_p) Model**

The corrosion process of the carbon steel in acid and/or sour environments, representative of atmospheric distillation plants in the petrochemical industry, is a very important scientific and technological topic in the oil industry. In fact, the refinery process is becoming more difficult and complicated due to the different qualities of the crude received on daily basis. In addition, the solids dissolved in the crude can provoke the formation of a corrosive aqueous solution whose chemical composition involves the presence of both hydrochloric acid (HCl) and hydrogen sulfide (H_2S). This solution is very aggressive, causing diverse damages to the structural properties of the carbon steel surface during the operating conditions of the distillation plants. For this reason it is necessary to establish an electrochemical methodology that makes it possible to evaluate

the electrochemical behavior of the carbon steel immersed in an acid and/or sour solution similar to those found in atmospheric distillation towers [65].

The overhead of a crude unit can be subjected to a multitude of corrosive species [66].

1. **Hydrochloric acid**, formed from the hydrolysis of calcium and magnesium chlorides, is the principal strong acid responsible for corrosion in the crude unit overhead.
2. **Carbon dioxide** is released from crudes typically produced in CO_2-flooded fields and from crudes that contain a high content of naphthenic acid.
3. **Low molecular fatty acids** such as formic, acetic, propionic and butanoic acids are released from crudes with a high content of naphthenic acid.
4. **Hydrogen sulfide**, released from sour crudes, significantly increases the corrosion of the crude unit overhead. Sulfuric and sulfurous acids, formed by either oxidation of H_2S or direct condensation of SO_2 and SO_3, also increase corrosion.

The sections of the process susceptible to corrosion include the preheat exchanger (HCl and H_2S), the preheat furnace and bottoms exchanger (H_2S and sulfur compounds), the atmospheric tower and vacuum furnace (H_2S, sulfur compounds, and organic acids), the vacuum tower (H_2S and organic acids), and the overhead (H_2S, HCl, and water). Where sour crudes are processed, severe corrosion can occur in furnace tubing and in both atmospheric and vacuum towers where metal temperatures exceed 450° F. Wet H_2S also will cause cracks in steel. When processing high-nitrogen crudes, nitrogen oxides can

form in the flue gases of furnaces. Nitrogen oxides are corrosive to steel when cooled to low temperatures in the presence of water [67].

Chemicals are used to control corrosion caused by hydrochloric acid produced in distillation units. Ammonia may be injected into the overhead stream prior to initial condensation, and/or an alkaline solution may be carefully injected into the hot crude-oil feed. If sufficient wash-water is not injected, deposits of ammonium chloride can form and cause serious corrosion. Detailed information about crude unit corrosion and naphthenic acid corrosion is available on websites and in books, corrosion journals and other sources.

Corrosive species in the pipeline flow streams play an important role in the overall degradation mechanism. Table 2.1 summarizes the different types of corrosion phenomena in oil and gas pipelines and their related aspects.

Table 2.1. Corrosion Types in Oil/Gas Pipelines [68, 69].

Contami-nant	Form of Attack	Corrosion Rate		Sources	Place of Attack
		Low Temp < 260 ºC	High Temp ≥ 260 ºC		
Air	- Fouling - Corrosion	Accelerate corrosion		- Plant equipment exposed during turnarounds & shutdowns. - Loose seals & connectors.	- Vacuum transfer lines. - Vacuum Towers. - Overhead of Crude Distillation Towers.
[Cl^-]	- Underdep osit corrosion.	- Increase corrosion rate due to		- Chloride salts in crude oils - Organic salts	- Overhead of Crude Distillation

	- Crevice corrosion - Pitting	increase of electrolyte conductivity - Low pH increases corrosion rate.		in solvents.	Towers. - Pipelines
Caustic	- Caustic corrosion - Gouging - SCC	- Caustic corrosion increases with temp.		- Neutralizers (NaOH)	- Crude transfer lines. - Boiler tubes.
[H_2]	- HIC - Hydrogen blisters		- Increases high temp sulfidic corrosion.	- Hydorgen Injections lines in the hydrotreating & hydrocracking operations.	- Vessels & Pipelines of hydrotreating & hydrocracking units.
[H_2S]	- Pitting - Crevice corrosion - Sulphide SCC - HIC - Hydrogen blisters - Uniform corrosion	Aqueous corrosion increases with increases hardness	- Corrosivity increases with temp. - Higher hydrogen concentration causes higher sulfidic corrosion.	Sour crude oils	- Vessels & pipelines of most refinery units.
Naphthen-ic Acid	- Pitting - Localized (lake-type) attack		- Higher temperature increases corrosion. - Increases high temp. sulfidic corrosion.	From organic acids in Crude Oils	- Trap and Bubble caps of distillation tower. - Vessels. - Furnace heads, elbows, and tees.
water	- Pitting	Accelerate corrosion in		- Found in all crude oils and	- Fractionation tower

	- Uniform corrosion	presence of air, Cl^-, & H_2S		hard to remove completely. - Stripping Steam.	overhead system. - Storage tanks.

Among all of the possibilities given in the table, we concentrated on two important species of corrosion that might play a significant role in the whole process:

1. Corrosion because of chloride concentration, and
2. Corrosion due to H_2S concentration.

H_2S and chloride were selected as the most corrosive species in the oil/gas pipelines due to the following facts [70-83]:

a. They are present in almost all types of crude.
b. A majority of the failures are due to these two factors.
c. Corrosion control measures are not completely able to stop these factors as compared to others (in the long run).
d. Carbon steel and stainless steel pipelines are mostly susceptible to pitting corrosion due to these factors.

Hence, a water-based solution flow medium having only Cl^- and H_2S as the corrosive agents will approximate for an oil flow medium in the refinery pipeline. There, the following efforts will be focused on identifying the most appropriate representation for the corrosion current, I_p, which includes the chloride and Sulphide effects which in turn would account for temperature effect as well.

2.2.5.1 **Chloride Corrosion**

First, we must differentiate between corrosion that occurs at low temperatures and is influenced by chloride concentration on the carbon steel material commonly used in the refineries, and the corrosion that occurs at high temperatures, influenced or attacked by hydrogen sulfide on carbon and other stainless steels.

Most chloride salts in the crude oil coming into a refinery are inorganic (sodium, magnesium, or calcium chloride) and are effectively removed by the de-salter. The non-extractable chlorides are not removed in the desalter, but can break down from downstream heating and processing to form hydrochloric acid (HCl) and can sometimes cause corrosion and fouling problems. The forms of these chlorides are still being determined, but they probably include organic chlorides (either natural or added via treatment chemicals or by the disposal of slops into the crudes); inorganic chlorides encapsulated in high-melting-point waxes or asphaltenes; or chlorinated solvents used in upstream operations. Even as little as 1% of the non-extractable chlorides can cause a major increase in the atmospheric tower overhead HCl and chloride levels and cause severe corrosion and fouling problems [68].

Attempts to model the effects of chloride concentration have been well documented in literature. Table 2.2 lists down some of the most promising models.

Table 2.2. Chloride Concentration Effect Models.

Proposed Model	Respective References
$I_p = A\ exp\ (-B\ E_{pit})$ $I_{corr} = E\ exp\ (-F \cdot [pH]\ )$ $CR = G\ exp\ (H \cdot [pH]\ )$	[84],[85],[88] [87],[91] [33]
$E_{pit} = -C\ log\ [Cl^-\ ] + D$ $E_{corr} = -R\ [\ pH]\ (+,-)\ S$	[85],[86],[87],[88],[89],[90] [87],[90],[91]
$pH = -P\ \ ln\ [\ Cl^-]$ $+\ \ Q$	pH decreases with increasing chloride concentration. [84],[86]
$I_p = M\ \ exp\ (\ N\ \ log\ [Cl^-]\ )$	The current density increases with the increasing of chloride concentration [84],[85],[88],[91]

The coefficients A,B,C,D,E,F,G,H,M,N,P,Q,R,S are constant values. It should be mentioned that the corrosion rate that depends on the corroded material, corrosion species, and environmental condition is proportional to the corrosion current density.

According to Brossia and Cragnolino on the effect of environmental variables on localized corrosion of carbon steel [92], the presence and concentration of chloride and the solution temperature also play key roles in determining whether localized corrosion of carbon steel occurs.

In general, once sufficient concentration of chloride is present such that localized corrosion is possible (for carbon steels, this concentration has been reported to be between 0.3mM and 3mM [92, 93], the effect of $[Cl^-]$ on E_{pit} follows the following relation:

$$E_{pit}(T) = E^{\circ}_{pit}(T) + B(T)\ log\ [Cl^-] \qquad 2.35$$

where E_{pit}° is the pitting potential at 1M chloride concentration, and $B(T)$ is the slope of E_{pit} dependence on $[Cl^-]$, with T, the absolute temperature.

Similar to chloride $[Cl^-]$, increasing the temperature generally results in decreasing E_{pit} values. In the paper [92], which examined the pitting behavior of carbon steel in bicarbonate solutions containing chloride, the authors found the following relations for E_{pit}° (mV) and $B(T)$ as a function of temperature:

$$E_{pit}^{\circ}(T) = -584.8 + 3.92\,T \;, \quad B(T) = -24.5 - 1.1\,T \tag{2.36}$$

By inserting the these relations in the above equation, we have

$$\begin{aligned} E_{pit}(T) &= E_{pit}^{\circ}(T) + B(T)\ \log[Cl^-] \\ &= (-584.8 + 3.92\,T) + \left(-24.5 - 1.1\,T\right)\log[Cl^-] \end{aligned} \tag{2.37}$$

Combining this relation with the given relations in the above table for the I_{corr}, we can see not only the chloride and temperature dependencies of I_{corr} but also the temperature dependencies of the appropriate coefficients in the following form. The general dependency,

$$I_p = A\exp\left(-B\,E_{pit}\right) \; and \;\; E_{pit} = -C\,\log[Cl^-] + D \tag{2.38}$$

together with the extended relation for E_{pit}, we get the following numeric equation,

$$I_p = A\,\exp\{-B\,\{(-584.8 + 3.92\,T) + (-24.5 - 1.1\,T)\log[Cl^-]\}$$

$$I_p = A\,\exp\{-B\,\{(-584.8 + 3.92\,T) + (-24.5 - 1.1\,T)\log[Cl^-]\}$$

$$= \ A \cdot \exp\{+B\ (24.5\ +\ 1.1\,T\ ) \cdot log[Cl^-]\}\,.\exp[(-3.92\,B)T] \qquad 2.39$$

We can see easily that the I_p values increase with increased chloride concentrations and the pre factor can be seen as possibly having a temperature dependency.

To emphasize that the above relations have a general character, we want to refer here to a paper of Matheison et. al on pitting resistance of 316L stainless steel [94], where it was suggested that E_{pit} may depend linearly on $log[Cl^-]$. Although they do not claim that such a simple, linear and additive model represents any fundamental law of nature, for engineering applications, a mathematical formulation may be useful. They give the following relations.

For pickled material:

$$E_{pit} = 456(\pm 21) - 4.6(\pm 0.4) \cdot T[°C] - 159(\pm 13) \cdot \log[Cl^-]\,;\ R^2 = 0.91 \qquad 2.40$$

For ground material:

$$E_{pit} = 543(\pm 29) - 5.0(\pm 0.4) \cdot T[°C] - 180(\pm 14) \cdot \log[Cl^-]\,;\ R^2 = 0.96 \qquad 2.41$$

with E_{pit} in mV (SCE), temp. in $°C$, and $[Cl^-]$ in g/L

The above relations are proved in the paper [94] for the chloride concentration ranges from 0.05% to 5%.

We can combine this relation with I_p values related to E_{pit} and get:

$$I_p = A\ exp\ (-B\ E_{pit}\ ) \quad 2.42$$

2.2.5.2 H_2S Corrosion

Sulphur is one of the foremost corrodents that cause problems in the refinery industry. It occurs in crude petroleum at various concentrations and forms a variety of chemical compounds, including hydrogen sulphide, mercaptans, sulphides, polysulphides, thiophenes and elemental sulphur. The crudes that are processed nowadays contain 1 to 3 wt. % of sulphur on average. The main forms of damage caused by sulphur to the steel structures include weight-loss corrosion, sulphide stress-cracking in low temperature aqueous environments, and high-temperature sulphide corrosion in non-aqueous environments at 200 – 500 ºC. Corrosion rates are dependent upon temperature, sulphur concentration, and the form in which the sulphur exists. Hydrogen sulphide is the most active compound from a corrosion standpoint [85, 86]. Most other sulphur forms can be considered almost inert until petroleum reaches the refinery. During refinery operations, due to the catalytic influence of the steel surface, less active sulphur compounds are converted into hydrogen sulphide. The amount of hydrogen sulphide evolved increases with temperature. Because of the great influence of hydrogen sulphide on the corrosion behaviors of the steels, two forms of sulphide corrosion are distinguished [68, 95]: (1) without hydrogen present and (2) with hydrogen present.

2.2.5.2.1 *Sulphide corrosion without hydrogen present*

Sulphur contained in hydrocarbon fractions in atmospheric and vacuum distillation units, catalytic cracking units, and hydro-treating and hydro-cracking units upstream of the hydrogen injection line destroys steel structures. Heat exchanger tubes, furnace tubes and piping are generally made of carbon steel. Elements of distillation columns, where temperature is above 250ºC and turbulent flow conditions are encountered, are usually lined with steel containing 12% of chromium. To predict the relative corrosive character of crude petroleum and its various fractions without hydrogen present, sulphide corrosion rates vs. temperature data have been gathered on the basis of industrial experience. The data given by respondents were incomplete and scattered considerably, but they were combined with earlier reported corrosion rates and presented as the so-called original McConomy curves [68, 95].

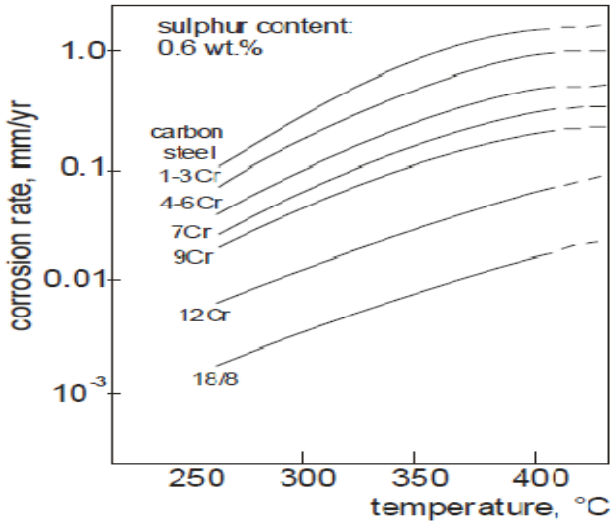

Figure 2.2. Modified McConomy Curves Showing the Influence of Temperature on Sulphide Corrosion Rates of Steels (without Hydrogen Present) [68, 95].

In Table 2.3 we tried to estimate our corrosion rate for carbon steel in case of corrosion without hydrogen present from these curves and obtained a relation for corrosion rate dependent on temperature:

$$CR = 1 \times 10^{-7} \cdot \exp\left(2.6 \times 10^{-2} T[K]\right) \qquad 2.43$$

Table 2.3. Corrosion Rate Corresponding to Different Temperatures using McConomy Curves

T [°C]	T [K]	Corrosion Rate [mm/yr]
250	523	0.07
275	548	0.15
300	573	0.29
325	598	0.60
350	623	0.90

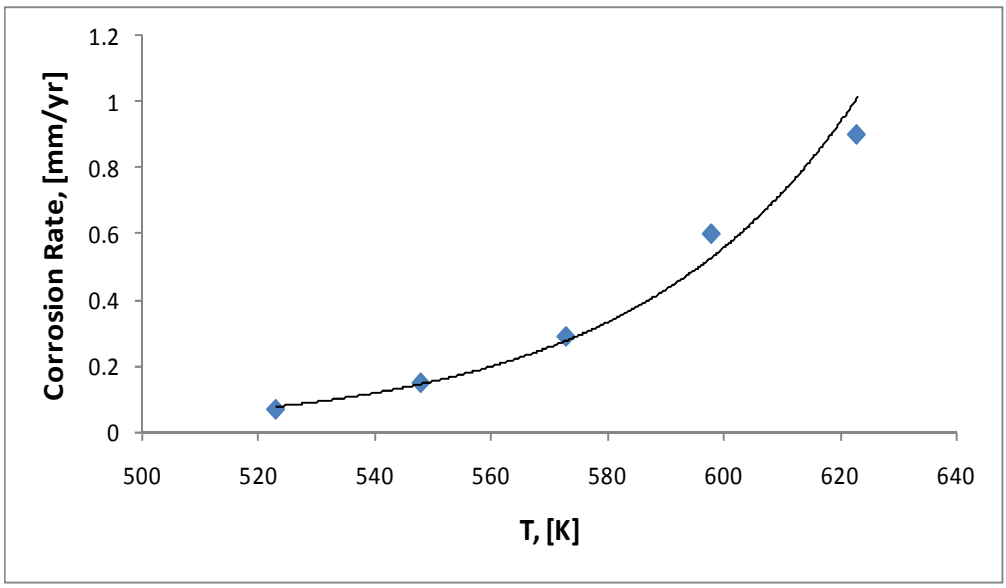

Figure 2.3. Corrosion rate –Temperature Dependency in McConomy Diagram Fitted for Carbon Steel.

The presence of sulphur on the steel surface causes the activity of carbon in the steel to increase, the thermal stability of the carbides to decrease, and the carbon that is released from the carbides to diffuse inside the steel. From a number of reports in the literature, we were able to predict and estimate the relation for the corrosion (pitting) currents will be discussed in the coming sections.

2.2.5.2.2 *Sulphide corrosion with hydrogen present*

The presence of hydrogen in some refinery operations, for example hydro-treating, hydro-cracking, and catalytic reforming increases the severity of sulphide corrosion. In this case the corrosion is detrimental not only because of metal loss but also because the volume of sulphide scale that is formed can lead to reactor plugging**.** Reactors, piping, elements of furnaces, and heat exchangers downstream the hydrogen injection-line is

particularly exposed to the corrosion. Reactor effluent piping operating above 250ºC, depending on the environmental parameters and expected corrosion rates, is made of carbon steel, Cr-Mo steels, or stabilized 18Cr-8/10Ni steels. Basic information for material selection for refinery hydrogen units is provided by the so-called Couper-Gorman curves [68, 95].

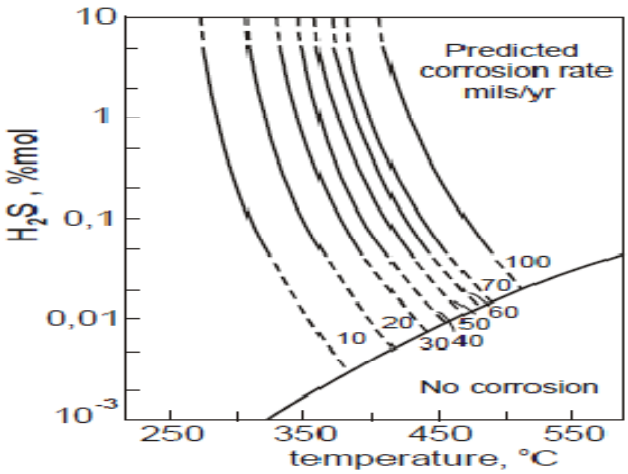

Figure 2.4. Effect of Temperature and Hydrogen Sulphide Content on High-Temperature H2S Corrosion of Carbon Steel [68, 95].

Table 2.4. Corrosion of Carbon Steel in Naphtha

H2S [mol%]	Corrosion rate(CR) in [mm/yr]	I_{corr} [uA]
0.1	6E-5 exp (0.0134 T[K])	(2.5979E-2)exp(0.0134 T[K])
0.2	2E-5 exp (0.0155 T[K])	(0.8660E-2)exp(0.0155 T[K])
1.0	1E-5 exp (0.0170 T[K])	(0.4330E-2)exp(0.0170 T[K])
10.0	8 E-6 exp (0.0179 T[K])	(0.3464E-2)exp(0.0179 T[K])

The general relation for the corrosion of carbon steel looks like:

$$CR(T) \approx I_p = M \times \exp\,(N \times T[K]) \qquad 2.44$$

for different H_2S concentrations.

Corrosion current related to the corrosion rate for carbon steels according to the given refinery data was chosen: $CR(mm/y) \sim (2.3095)\ x\ Icorr(T)]$.

Table 2.5. Corrosion Rate and Current (Density) of Carbon Steel in Gas-Oil

H_2S [mol%]	Corrosion rate(CR) in [mm/yr]	I_{corr} [uA]
0.1	6E-5 exp (0.0146 T[K])	(2.5980E-2)exp (0.0146 T[K])
0.2	5E-5 exp (0.0149 T[K])	(2.1649E-2)exp (0.0149 T[K])
0.5	4E-5 exp (0.0156 T[K])	(1.7319E-2)exp (0.0156 T[K])
1.0	3E-5 exp (0.0165 T[K])	(1.299E-2) exp (0.0165 T[K])
5.0	2 E-5 exp (0.0173 T[K])	(0.866 E-2)exp (0.0173 T[K])

The general relation for the corrosion of carbon steel looks like:

$$CR\ (T) \approx I_p = P \times \exp\,(Q \times T[K]) \qquad 2.45$$

for different H_2S concentrations.

Corrosion current related to the corrosion rate for carbon steels according to the given refinery data was chosen as: $CR\left(\frac{mm}{y}\right) \sim (2.30955\ )x\ Icorr(T)$.

The curves were elaborated on the basis of a survey conducted by the National Association of Corrosion Engineers (NACE) Committee T-8 on Refining Industry [93].

They present the influence of temperature and hydrogen sulphide concentration on corrosion rates of carbon steel, 5Cr-0.5Mo steel, 9Cr-1Mo and 18Cr-8Ni steel. For ferritic steels two sets of curves apply, depending on whether the environment is gas oil or naphtha. It was indicated that no corrosion occurs at low hydrogen sulphide concentrations and temperatures exceeding 320ºC.

Because of the antagonism between sulphur and carbon, the sulphur on the steel surface causes the carbon activity in the steel to increase, and the stability of the carbides to decrease. Moreover, hydrogen accelerates the process of carbide decomposition. Elevated temperature and increased hydrogen partial pressure allow for hydrogen particles to dissociate and hydrogen atoms to adsorb on the steel surface and diffuse inside the steel. Under the parallel influence of the sulphur and hydrogen, the carbides are more prone to decompose than under the influence of the sulphur action alone. Hydrogen supports the process of carbide de-stabilization. This is why an increased sulphide corrosion rate of the steel at the presence of hydrogen can be expected [68, 95].

It should be mentioned here that there are some reports that relate the corrosion rate and corrosion current to the pH values [96, 97], but we think that the temperature dependency of corrosion in the case of H_2S-corrosion plays a more significant role than the pH of the solution. The pH dependency is important, then, when we have a combination of corrosion species and they appear in competition with each other in the corrosion process.

2.2.5.2.3 *Modeling Chloride and H_2S Corrosion Combination Effect on I_p*

In the polarization resistance method, the corrosion current is related to the slope of the potential-current plot through the following relation [92]:

$$\frac{\Delta E}{\Delta I} = R_p = \frac{\beta_a \beta_c}{2.3(i_{corr})(\beta_a + \beta_c)} \quad 2.46$$

where β_a = polarization resistance (Ohm), β_c = anodic and cathodic Tafel constants (assumed to be 0.1V), and i_{corr} corrosion current (A). According to this general corrosion relation and setting values for β_a& β_c, we can reduce the above equation to

$$R_p = 2.174 \times 10^{-2} \cdot I_{corr}^{-1} \sim \frac{a}{I_{corr}} \quad 2.47$$

The parameter R_p , the polarization resistance, behaves like a resistor. If the Tafel constants are known, one can calculate the I_{corr} from R_p. I_{corr} can be used to calculate the corrosion rate.

Now there are two possibilities for the R_p values [98]:

1. R_P's are in series:

$$R_p = R_{p1} + R_{p2}, \quad 2.48$$

$$\Rightarrow \frac{a}{I_{corr}} = \frac{a_1}{I_{corr(1)}} + \frac{a_2}{I_{corr(2)}}$$

$$\Rightarrow I_{corr} = \frac{I_{corr(1)} * I_{corr(2)}}{\alpha * I_{corr(1)} + \beta * I_{corr(2)}}$$

Or,

2. R_P's are parallel:

$$\frac{1}{R_p} = \frac{1}{R_{p1}} + \frac{1}{R_{p2}}$$

$$\Rightarrow a * I_{corr} = a_1 * I_{corr1} + a_2 * I_{corr2}$$

$$\Rightarrow I_{corr} = \alpha * I_{corr1} + \beta * I_{corr2} \qquad 2.49$$

This form is a linear combination of different current (densities).

The following possibilities can be chosen for the estimation of corrosion current (densities):

1. Separation of the chloride and hydrogen sulphide corrosion

A) With

$$I_p = A \exp\left(-B\, E_{pit}\right), \qquad 2.50$$

$$E_{pit} = -C \log[Cl^-] + D \qquad 2.51$$

$$pH = -P \ln[Cl^-] + Q \qquad 2.52$$

or

$$I_p = A * exp\{+B\,(24.5 + 1.1\,T)log[Cl^-]\}.exp\,[(-3.92\,B)\,T] \qquad 2.53$$

B) With

$$CR = 1 \times 10^{-7} \cdot \exp\,(2.6 \times 10^{-2} T[K]) \qquad 2.54$$

for 0.6 mol% at different temperatures.

or

$$CR(T) \approx I_p = M \cdot \exp\,(N \cdot T[K]) \qquad 2.55$$

for different H_2S concentrations (in gas–oil, or naphtha) according to the above given Tables 2.4 & 2.5.

2- Application of weighted form for the combination:

This relation can be given in the following weighted form that depends on the surface coverage θ (theta),

$$I_p = I_p([Cl^-]) \cdot \theta + I_p([H_2S]) \cdot (1 - \theta) \qquad 2.56$$

where θ is surface coverage.

This relation is similar to the linear combination function. It should be mentioned here that pH is a function of chloride concentration $[Cl^-]$, i.e. pH decrease with an increase in the chloride concentration, and $I_p^{[H_2S]}$is a function of temperature.

3- Combination of Chloride and Hydrogen Sulphide Corrosion

In sour (H_2S) and chlorinated environments the synergetic effect of chloride concentration and hydrogen sulfide concentration can be detrimental and can increase the corrosion rate. Chloride in the presence of hydrogen sulfide has the tendency to make a localized attack and cause localized corrosion; they synergistically affect the corrosion

rate in a sour environment in an additive [99-101] form. The following reasons cited in the literature support the additive form:

- The additive form is based upon the mechanism of anodic dissolution of iron in acidic solutions containing H_2S as proposed in [99].
- Chlorine ion (Cl^-) is the prerequisite for pitting corrosion in H_2S environments. [102]
- H_2S makes it easier for chloride ions to initiate pits. [103]
- In sour service environments, a synergetic action between H_2S and chloride ions is observed, the role of H_2S being attributed to its ability to depassivate the steel. [100, 104, 105]

So we can say that the total corrosion rate is the sum of the contribution of the chloride and the hydrogen sulfide together:

$$CR = CR(Chloride) + CR(Hydrogen\ Sulfide) \quad 2.57$$

This means, in other words, that

$$I_{p,Total} = I_p^{[Cl^-]} + I_p^{[H_2S]} \quad 2.58$$

The general form of the additive total corrosion rate can have a different form depending on the condition of the fixed temperature or on the given temperature and concentration of the corrosion species:

$$I_p(t) = I_p([Cl^-]) + I_p([H_2S])$$

$$I_p(t) = \{A \cdot exp(B \cdot log([Cl^-]))\} + \{C \cdot exp(D \cdot log([H_2S]))\} \quad 2.59$$

or,

$$I_p(t) = \{A \cdot exp(B \cdot (24.5 + 1.1T) \cdot log([Cl^-]))\} \cdot exp[(-3.92E)T] + C \cdot exp(D \cdot (-5.738 + 0.007T[K] + 0.017[H_2S])) \quad 2.60$$

A, B, C, & D constants that are determined experimentally.

2.2.5.2.4 *Experimental Proof for the Proposed Additive form of Ip_{Total}*

The proposed additive form for the total corrosion current Ip_{total} in Equation 2.58 will be now proofed experimentally.

2.2.5.2.4.1 Cyclic Voltammetric (CV) Experiment

Cyclic voltammetric experiments [106, 107] were performed by Mr. Mohammad Nuhi with a BAS CV-5W voltammetric analyzer in the chemistry department at the University of Maryland under the supervision of Dr. Min Jia, a post-doctorate researcher of Professor Neil Blough. All the measurements were carried out in a three-electrode measuring cell. A hanging platinum plate was used as a counter electrode, an Ag |AgCl| KCl(sat) was used as a reference electrode, and our specimen (X70 carbon steel mounted in an epoxy resin with a standard area of 1 cm^2 and sealed back contacted) was used as

working electrode for the measurements. The counter electrode was a platinum band (sealed and back contacted with Cu-wire). The BAS system was connected to a computer for data acquisition, with appropriate software for evaluating the data. Cathodic and anodic branches of the polarization curve were monitored during the sweeping of potential. The data was transported in text form from the DOS program to MS Excel in data form.

2.2.5.2.4.2 Specimen Preparation

Three 1-cm^2 specimens were connected from behind and embedded from the free unconnected part in a resin mass (cold mounted) [108] provided by CALCE, in the mechanical engineering department, and polished on different 400, 600, 800 and 1500 mesh – sand papers (each time for at least 2 hrs). The specimen was checked under the microscope in the Kim building under the supervision of Professor R.J. Bonnenberger for smoothness of the surface. Thus, the specimens were ready for the electrochemical experiment as working electrodes in the BAS–CV equipment.

2.2.5.2.4.3 The Standardized Experimental conditions given to the BAS-CV system

E_{Init}(mV) = -1200 , E_{High}(mV) = 200 , E_{Low}(mV) = -1200 , $(P/N)_{Init}$ = P

V (mV/sec) = 100 , Number of Segments = 2 , Sample Interval (mV) = 1

Quiet Time (sec) = 2 , Sensitivity (A/V) = 1E-3

2.2.5.2.4.4 Experimental Procedure

Three different specimens were prepared as working electrodes for experiments in:

1- Chloride (concentration ~ 7.1 g/liter) + water solution

2- H_2S($S_2O_3Na_2 + 6H_2O$,Sodium thio-sulfate, 500ppm) + water solution

3- Chloride (concentration ~ 7.1 g/liter) + H_2S (500ppm) + water solution

The data were evaluated and the first current-potential curves were prepared. Then the same data were used to build a semi-logarithmic drawing like diagrams mentioned above. Then, we used the second method (drawing the slopes on the cathodic and anodic parts of the curves) to get the corrosion current values.

The corrosion currents for the working electrode (steel specimen) in seawater show that corrosion currents vary between 10^{-5}A to 10^{-4}A, and the corrosion currents for the specimen in chloride + H_2S show a corrosion current between 10^{-4}A to 10^{-3}A. This shows an increase in corrosion current in a more corrosive medium, and in addition, it shows that the addition of corrosion current as proposed in our first model might be a good approximation. Figure 2.5 below shows different steps from the electrochemically potentiodynamic potential–current diagram to the semi-log potential–current diagram and their relation to potentiodynamic or voltammetric diagrams [109].

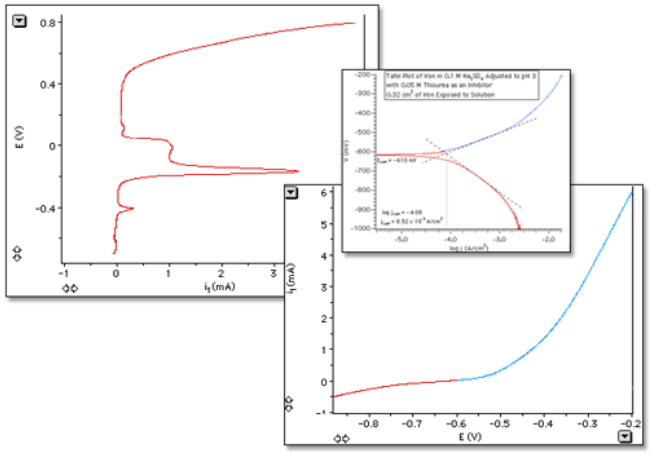

Figure 2.5. Electrochemical Measurement of Corrosion [104].

2.2.5.2.4.5 Evaluation of data

The transported data were evaluated in the Excel program and are given in the following tables:

Table 2.6. Electrochemical Measurements of Corrosion for Water + Chloride + H_2S Solution

Specimen Name	Mean Values
CLSSCH	1.2150×10^{-4} A
CLSHSH	1.1725×10^{-4} A
CLSHCLSH	1.7625×10^{-4} A
CLSHCLS	1.5700×10^{-4} A
CLLSHCL	1.5800×10^{-4} A
CLLSHH	1.2995×10^{-4} A
CLCHH	1.3250×10^{-4} A
Mean =	1.43345×10^{-4} A

Table 2.7. Electrochemical Measurements of Corrosion for Water + H_2S Solution

Specimen Name	Mean Values
WSHGG	0.837×10^{-4} A
WSHG	0.94×10^{-4} A
WSH	0.74×10^{-4} A
WSHH	0.725×10^{-4} A
WSHHG	0.742×10^{-4} A
WSHHH	0.665×10^{-4} A
Mean =	0.775×10^{-4} A

Table 2.8. Electrochemical Measurements of Corrosion for Water + Chloride Solution

Specimen Name	Mean Values
WCLLLLL	0.801×10^{-4} A
WCLLLL	0.737×10^{-4} A
WCLLL	0.651×10^{-4} A
WCLL	0.6415×10^{-4} A
WCLGH	0.569×10^{-4} A
WCLGGL	0.683×10^{-4} A
Mean =	0.6804×10^{-4} A

Now, the means from Tables 2.7 and 2.8 are summed to produce the following:

0.775×10^{-4} A + 0.6804×10^{-4} A = 1.4554×10^{-4}A

($W+H_2S$) + ($W+ [Cl^-]$) = ($W+[Cl^-] + H_2S$)

as is visible in the diagrams.

In solutions under H_2S influence the cathodic effect is more significant than in the third case, where chloride alone is the corrosive species. In the third case, the anodic part is affected more strongly.

The sum of the W+[Cl-] and W+[H_2S] is nearly an order of magnitude equal to the W+ [Cl-] + [H_2S]. This estatement was proposed in our work about the influence of chloride and hydrogen sulfate together as a corrosive specie in the corrosive environment.

2.2.5.3 **Factors that influence the rate and severity of cracking**

The following are key factors influencing the cracking rate and severity:

1. Chloride content
2. Oxygen content
3. Temperature
4. Stress level
5. pH value of an aqueous solution

It has been established that oxygen is required for chloride cracking to occur. The severity of cracking increases with temperature. Cracking has been found to occur, however, at tropical locations where exposure to direct sunlight can increase metal temperatures significantly above ambient. As a general rule, chloride SCC of process equipment occurs only at temperatures above about 65°C (145°F). The stresses required

to produce cracking can be assumed to be always present in the form of residual stress or thermal stress.

Carbon steels are among the most widely utilized materials for structural and refinery applications because carbon steel generally undergoes relatively predictable uniform dissolution in many environments. However, there are a number of environmental factors that can cause carbon steel to undergo rapid, localized corrosion instead of relatively slow, uniform corrosion [92]. The new, stronger generation of pipeline steel includes X70 and X80, which exhibit a fine-grained, bainitic ferrite micro-structure.

The main chemical composition and mechanical properties of the X70 steel are listed in the tables below:

Table 2.9. Composition of X70 Carbon Steel (wt%) [110,111].

Element	C	Mn	Si	P	S	Other
X70	0.04	1.5	0.24	0.008	0.0025	< 0.1

Table 2.10. Mechanical Properties of X70 Carbon Steel [110].

Material	σ_y (MPa)	σ_{UT} (MPa)
X70	537	634

E=2.07×10^5 MPa [107].

According to the B. T. Lu et. al, X70 carbon steel, before the stress cycles N reach 5×10^5, shows no cracks, but general corrosion and pits are observed. After N > 5×10^5, cracks

begin to initiate and then propagate along the direction perpendicular to the maximum tensile stress. It should be mentioned here that the crack initiation and sizes [110] were monitored under optical microscope with the acetate replica technique. In our case the corrosion-fatigue crack initiated with pits and may have been accompanied by non-metallic inclusions in the micro-structure. Our transition micro-crack corresponded to an average number of cycles, $1.69\times10^5 < N < 3.6\times10^5$. The stress concentration and local electrochemical condition produced by pits will promote crack initiation [110-112].

Factors affecting the corrosion-fatigue behavior of X70 carbon steel as mentioned above and given briefly in accentuated form are environmental factors such as chloride [Cl^-] and H_2S corrosion species. Their influence on crack initiation and propagation itself depends on pH, applied stress, frequency of the applied fatigue load, temperature and pressure. Corrosion rate versus pH and temperature, for example, are given in the figure below:

Table 2.11. Corrosion Data for Different pH Values

pH	mm/yr	mg/hr
3	5.59E-03	5
4	3.35E-03	3
7	1.12E-03	1
9	8.39E-04	0.75
11	5.59E-04	0.5

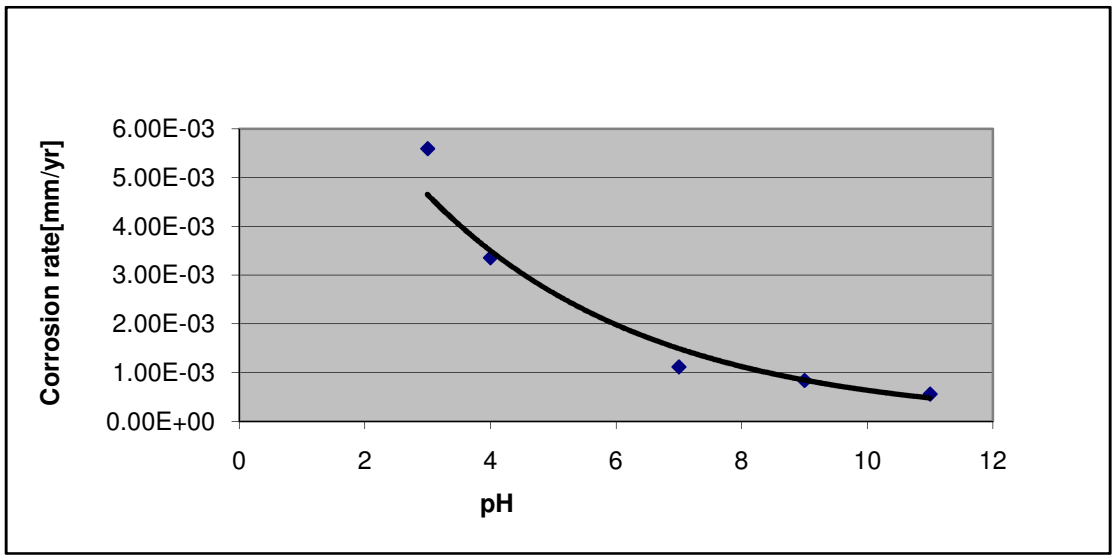

Figure 2.6. Corrosion Rate vs. pH.

As shown in the figure above, the corrosion rate decreases with the increasing pH values, and for X70 carbon steel we know (as mentioned above and according to [112]) that by increasing the chloride and H_2S concentration the pH values have a decreasing tendency (more acidic behavior).

Table 2.12. Corrosion Data at Different Temperature Values

T [C]	T [K]	mm/yr	mg/hr
25	298	1.12E-03	1
40	313	1.25E-03	1.125
52.5	325.5	1.67E-03	1.5

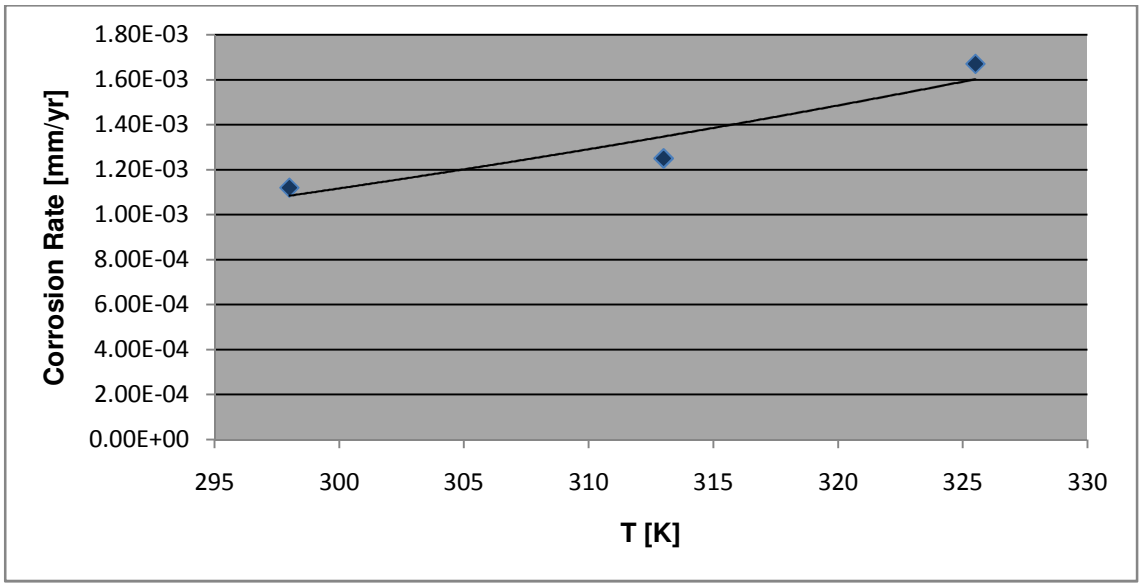

Figure 2.7. Corrosion Rate vs. Temperature.

The calculated temperature dependency of the corrosion rate shows that this tendency is not so significant unless there are very high temperatures and very high concentrations of the corrosion species [112].

The most important aspect of treatment of corrosion-fatigue in structures is the environment. Proper consideration of the environment is required at every step of the process of the generation and use of corrosion-fatigue data [113]. Understanding the mechanical, metallurgical and environmental aspects are not only essential for interpretation of the experimental data but are also necessary to set up the experimental equipment properly. There are a bewildering number of variables that affect the environmental fatigue crack growth that have been categorized by R.P. Wei et. al in their review paper [114]:

Mechanical Variables:

- Maximum stress or stress-intensity factor
- Cyclic stress or stress-intensity factor range
- Stress ratio or load ratio, R
- Cyclic load frequency
- Cyclic load waveform (for constant-amplitude loading)
- Load interactions in variable-amplitude loading
- State of stress
- Residual stress

Metallurgical Variables:

- Alloy composition
- Distribution of alloying elements and impurities
- Microstructure and crystal structure
- Heat treatment
- Mechanical working
- Preferred orientation of grains and grain boundaries (texture)
- Mechanical properties (strength, fracture toughness, etc)

Environmental Variables:

- Temperature
- Pressure
- Type of environment (gaseous, liquid, etc)

- Partial pressure of damaging species
- Electrochemical potential
- pH
- Viscosity of environment
- Velocity of environment
- Coatings, inhibitors, etc. [109, 110]

Most of these variables or combinations of these are important in characterizing the corrosion-fatigue crack initiation and growth. We want to concentrate on some of those that are characteristic in an oil refinery.

2.2.5.3.1 ***Temperature:***

As shown above, temperature is one of the most important variables. Nearly all the researchers report a rapid increase of corrosion with increased temperature, especially in connection with H_2S and sulfur and naphthenic corrosion in temperatures higher than 270C. According to the literature [115], at higher temperatures naphthenic acid corrosion becomes evident, the rate of corrosion gradually increasing with the temperature. Maximum corrosion occurs often at temperatures of 270-280°C, and above 350°C the corrosion again increases rapidly, being due for the most part to the action of sulfur [115]. The majority of the data indicates that a temperature increase of 38°C approximately doubles the corrosion rate of attack. This behavior is given by an exponential tendency, or curves by G. Sorell et al. [116], which is given by the following equation:

$$corrosion\ rate = CR\ [in/yr] = K \cdot exp(A \cdot T[K]) \quad 2.61$$

with K~0.0014 and A~ 0.0062.

Maximum corrosion rates result in the temperature range of 400-500°C. It should be noted that the corrosion rates increase with higher H_2S and chloride concentrations and this tendency is given by nearly all the literature in different forms such as

$$CR\ [in/yr] = 0.2138[exp(0.0348[H_2S(vol\%)])] \quad 2.62$$

The presence and concentration of chloride and solution temperature play key roles in determining whether localized corrosion of carbon steel occurs. This effect on E_{pit} of iron and carbon steel has been examined by several investigators and is summarized by Szklarska-Smialowska [92, 93] in the form of

$$E_{pit}(T) = E^{o}_{pit}(T) + B(T) \cdot log[Cl^{-}] \quad 2.63$$

Similar to $[Cl^-]$, increasing the temperature generally results in decreasing E_{pit}.

2.2.5.3.2 ***Pressure and partial Pressure:***

The total pressure appears to be an important corrosion variable only in as much as it determines the partial pressure of the hydrogen sulfide in a gas mixture. An interesting fact in the literature [116] is that in attempting to relate the rate of attack to some measure

of hydrogen sulfide content, it becomes apparent that the normally often used measure like weight and volume or mol. percent do not correlate as well as does the partial pressure of the hydrogen sulfide in the gas mixture, and the total pressure on each other and their effects on the corrosion rate, where the following relation can be derived can be expressed as

$$CR\left[{}^{in}/_{yr}\right] = exp(-5.73895 + 0.00665T[K] + 0.0174[H_2S]) \quad 2.64$$

and

$$[H_2S] = 0.0909\ P_{[H_2S]} \quad 2.65$$

with $P_{[H2S]}$ = partial pressure of hydrogen sulfide.

Partial pressure = (Mole% x psi)/100

Carbon steels are susceptible to hydrogen-induced cracking (HIC). This can occur when carbon steel is exposed to hydrogen sulfide; the risk of HIC should be considered when the partial pressure of H_2S > 3.5 mbar. Hydrogen-induced cracking (HIC) can theoretically occur at lower levels of H_2S, though as the partial pressure decreases the rate of accumulation of hydrogen damage decreases. The 3.5 mbar level is set as a practical level below which significant HIC damage would not be expected to accumulate during a normal service life. At higher levels of H_2S, the rate of hydrogen entry is expected to increase (although there is not a linear relationship between the amount of H_2S in the environment and the amount of hydrogen which enters the steel). What can be stated is that the likelihood of HIC damage becomes greater at higher levels of H_2S [117].

As-welded or as-bent carbon steel fabrications are susceptible to carbonate cracking because of the level of residual stress remaining after fabrication. If the equipment/piping is properly stress relieved, then it is considered not susceptible to carbonate cracking. A post-weld heat treatment of about 620°C (1150°F) for one hour per 25 mm (1 inch) of thickness (one hour minimum) is considered to be effective for carbon steel [117, 118].

2.2.5.3.3 ***pH***

This has been indicted above and discussed in Figures 2.6 and 2.7 and also Tables 2.11 and 2.12.

2.2.5.3.4 ***Effect of cyclic frequency on corrosion FCG rates***

It is known that the application of traditional methods of electrochemical protection may be unsuccessful if an engineering structure or its components are loaded (e.g., cyclically loaded) under in-service conditions. In 1975, Vosikovsky [119] showed that cathodic protection resulted in the acceleration of corrosion FCG rate, da/dN, in X-65 pipeline steel exposed to 0.6 M NaCl solution shown in the figure below.

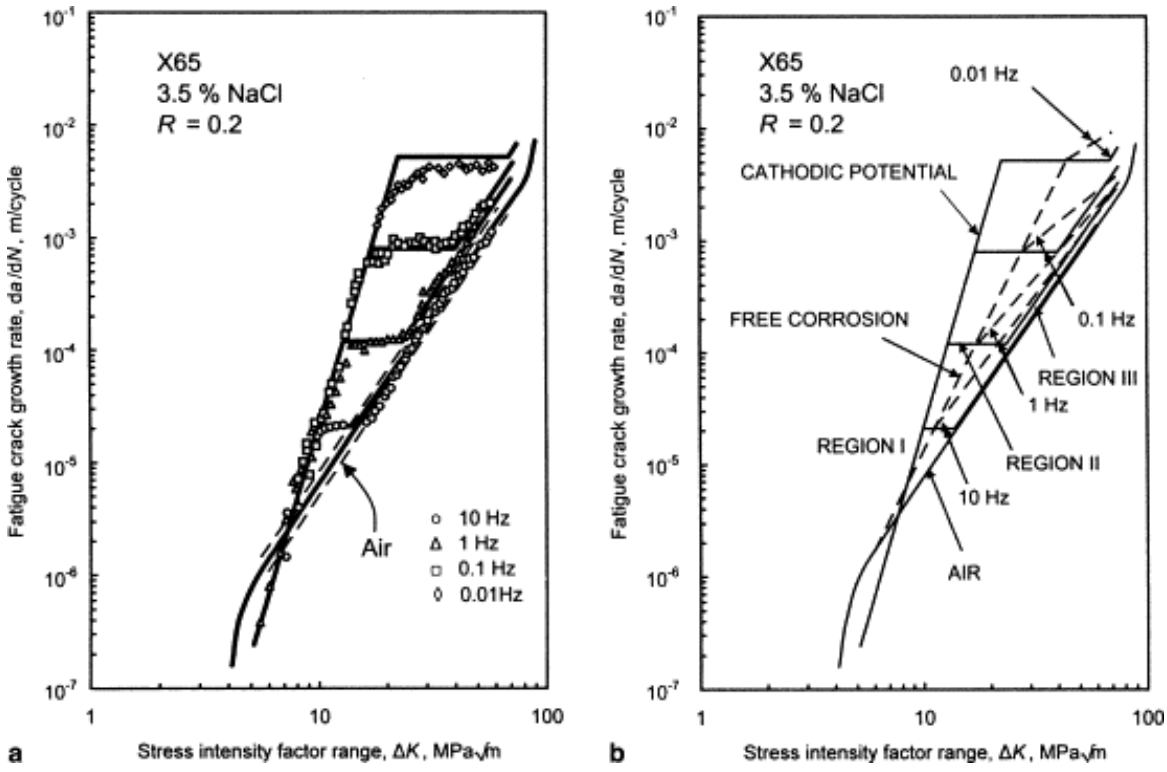

Figure 2.8. (a) FCG Rates at the Cathodic Potential of −1040 mVSCE and Four Frequencies; (b) Comparison of FCG Rates at the Cathodic Potential of −1040 mVSCE and OCP and Four Frequencies for X-65 Steel [119].

The solid lines at the cathodic potential and the dashed lines at OCP through the growth rate data were defined by corresponding equations [119]. Vosikovsky used pre-cracked fracture mechanics specimens and carried out his tests over a frequency range between 0.01 and 10 Hz. He found that the lower the cyclic frequency, the higher the acceleration in corrosion FCG rates observed under CP in comparison with crack growth rates in air. The maximum increase in da/dN at lowest frequency (0.01 Hz) was 50 times at the cathodic potential of -1040 mVSCE and 10 times under the open-circuit potential of -680

mVSCE, relative to da/dN found in air. The severity of hydrogen embrittlement is highly dependent on the rate of hydrogen diffusion into the region of high tensile triaxiality in the metal matrix ahead of the crack.

The maximum effect of the environment on crack growth will not be seen unless sufficient hydrogen has had time to accumulate in this region so that a critical combination of stress state and hydrogen concentration is attained [119]. It was also shown [119-121] that slower loading frequencies, more negative potential and higher temperatures resulted in a substantially higher ‘‘plateau crack growth rate’’ on the da/dN vs ΔK diagrams. As the cyclic frequency increased, the rate of supply of absorbed hydrogen becomes limited because crack growth is faster on a time basis [122].

2.2.5.3.5 *Importance of the crystallographic orientation of materials in the corrosion behavior*

V. Venegas et. al in their article “Role of Crystallographic Texture in Hydrogen-Induced Cracking of Low Carbon Steels for Sour Service Piping” [123] write that electron backscatter diffraction (EBSD) and X-ray texture measurements performed on HIC samples of API 5L X46 and ASTM A106 steels show that the resistance to hydrogen-induced cracking (HIC) of low carbon steels for sour service piping could be improved through crystallographic texture control and grain boundary engineering. W. F. Brickell et al. [124] mentioned that the rate of hydrogen penetration through single crystals of iron in contact with an H_2S-CO_2-H_2O environment was related to the specific crystallographic orientation of the crystals used, and the rate of hydrogen penetration was a function of the

lattice packing density of the exposed crystal plane. The rate decreased with the orientation of the single crystal planes.

It should be mentioned here that the crystal orientation and the type of packing plane might have an enormous effect on the corrosion-fatigue of the iron-based materials, and this dependency might influence the current density and the pitting probability of the material.

2.3 *Summary*

Pitting corrosion was selected to represent the initiation agent of failure for the subsequent corrosion-fatigue degradation failure mechanism. The pitting growth rate was constructed with the assumption of having a constant pit shape. Hydrogen embrittlement as the base concept which accounts for many pipelines hydrogen induced failures, has guided to select Wei's superposition model as a benchmark model for corrosion-fatigue. Paris law for fatigue crack growth has been identified to model the mechanistic part of Wei's superposition model. The weight factor that amounts to the corrosion-fatigue contribution in Wei's model has been sensibly constructed utilizing existing physical chemistry aspects. Lastly, the summation form model for the corrosion current has been proposed and experimentally approved.

So, the selected physics-of-failure benchmark model is now fully constructed for the subsequent analysis. All components of the benchmark model: Pitting corrosion,

corrosion-fatigue, electrochemical model, and corrosion current model, are well represented to generate the intended outcomes: crack size vs. number of cycles.

CHAPTER 3

EMPIRICAL MODEL DEVELOPMENT

3.1 *Introduction*

Proposing a simple empirical model for the corrosion-fatigue degradation mechanism is a key contributor of this research. Furthermore, in order to implement a probabilistic analysis it is essential to have the least number of uncertain variables in the proposed empirical model. Integrating two degradation mechanisms namely pitting corrosion as an initiating agent of failure and corrosion-fatigue as a subsequent agent of failure compromise an intrinsic challenge for modeling process. Pitting corrosion degradation mechanism is controlled by a different set of driving forces as compared to corrosion-fatigue degradation mechanism. Besides, the transitional point between the two degradation mechanisms is not quite well defined in the literature and need to be investigated so as to properly address the proposed empirical model. The uncertainty of parameters of the proposed empirical model needs to be estimated.

The benchmark model discussed in Chapter 2 will be deployed in simulation routine and will be run to aid in proposing the simple empirical model so as to capture the two major degradation mechanisms of pitting corrosion and corrosion-fatigue. Prior to any computation effort, the major assumption pertaining to this research is set henceforth to facilitate the computation load and well justify the subjective part of it. All the variables

involved in this simulation are well designated to have either represented by deterministic or probabilistic values with the review of the literature. The routine code for simulating the benchmark model is written in MATLAB which produce the distribution for the crack size vs. number of load cycles. Based on the outcomes of the simulation, a simple empirical model will be proposed with least number of uncertain parameters. A correlation with the pipeline physical parameters, e.g. temperature, loading stress, etc. will follow the simple empirical model proposal. Lastly, a premature estimation of the uncertain parameters of the model will be explored.

3.2 *General Assumptions*

The major assumptions employed in structuring the empirical model of pipelines degradation are discussed in this section. Some of the assumptions are inherent in probabilistic fracture mechanics analysis of the pipelines, while others are more germane to the specific type of analysis. Throughout the analysis other assumptions more specific to the different sections will be presented. Uncertainties due to these assumptions are not quantified and should be analyzed in future research. The assumptions made are not expected to significantly alter the results of the probabilistic modeling of the corrosion-fatigue crack growth phenomenon.

The following are the general assumptions:

- Pipeline failure due to corrosion-fatigue occurs due to the growth of cracks emitting from corrosion pits on the internal surface. Other failures due to design,

manufacturing, assembly or errors in use are omitted. All other failures which are stochastic in nature, such as accidental impact, are also omitted. These should be considered in future studies.

- Pit nucleation is not considered in the modeling effort in this research. This is under scientific investigation, and further development will be required before it can be adopted. Hence, the pit initial size will be assumed to be zero or near zero in the analysis resembling a flush finish pipeline internal surface.

- Pit-to-crack transition modeling is also not considered in this research. This phenomenon is still being debated in the literature, and a solid, widely acceptable physical model is awaited. In this research, only the criterion set in literature,

$$\left(\frac{da}{dt}\right)_{crack} = \left(\frac{da}{dt}\right)_{pit}$$

will be applied for pit transition to a crack. The transition occurs when the pit-depth growth rate equals the crack-depth growth rate.

- All pits and cracks are assumed to be located on the inside of the pipeline wall. Embedded cracks were not considered since it has been documented that only surface cracks grow in fatigue.

- Pits in the pipelines are independently and identically distributed in size. In other words, the initial pit-size distribution is taken to be the same in each section of the cylinder.

- The aspect ratio of the crack remains constant during the crack growth. Nevertheless, a varying aspect ratio could be explored in future research.

- The sub-critical growth of cracks due to corrosion-fatigue are similar to fatigue crack growth and can be predicted from linear elastic fracture mechanics or elastic plastic fracture mechanics analysis.

- The stress history defined by cycling from pressurizing and depressurizing the pipelines due to the fluctuating operation of the inline pumps, controls corrosion-fatigue crack growth.

- If more than one crack exists in each section of the pipeline then the cracks will not interact with each other or nucleate to form larger cracks. The critical condition for unstable crack propagation is dependent only on the size of the largest crack present on the internal surface of the pipeline.

- The corrosion current, Ip, is assumed to be deterministic in the modeling analysis. This assumption is based on the stable condition of the pipeline's internal

environment. Excluding the rare fluctuating events, the average corrosion current of the pipelines remains constant.

- The applied stress used in the failure criterion will not be significantly relaxed by crack extension but instead remains constant even during incremental crack growth. Initial pressure is only relaxed when the crack breaches the wall.

- Pits are hemispherical in shape and grow at constant volumetric rate in accordance with Faraday's law from an initial radius $a_{o.}$

- Cracks retain the same profile during crack growth until they grow through the walls of the pipeline. Once a crack grows through the pipeline wall, the outside and inside surface lengths are equal.

- The adopted corrosion-fatigue degradation model—Wei's super-position model—is the most suitable and practical model to be used as a benchmark model. A comprehensive literature review has confirmed this evidence and is summarized in Chapter 1.

- Pits and cracks are found during the testing phase after manufacturing or periodic testing using NDE techniques. The probability that a crack will be detected depends only on the size and not on the skill of the equipment operator.

3.3 *Computational Methodology Procedure*

The objective of this research was to build an empirical model with a minimum number of parameters capable of tracing the corrosion-fatigue degradation predicted by a physical model. Most of the reviewed physical models in the literature have demonstrated their capability of estimating the corrosion-fatigue degradation level, but most of them had to employ a cumulative number of parameters with few limitations. Probabilistic modeling of physical models is quite challenging, and reducing the number of parameters to the minimum turned out to be a prerequisite. In addition, selecting the simplest physical corrosion-fatigue model form was another factor to be taken in account to facilitate the probabilistic analysis. A cautious selection of the corrosion-fatigue physical model along with the accompanying probabilistic modeling procedure was a crucial element in this research. Figure 3.1 illustrates the flow of steps undertaken in this research and is followed by a brief description of each step.

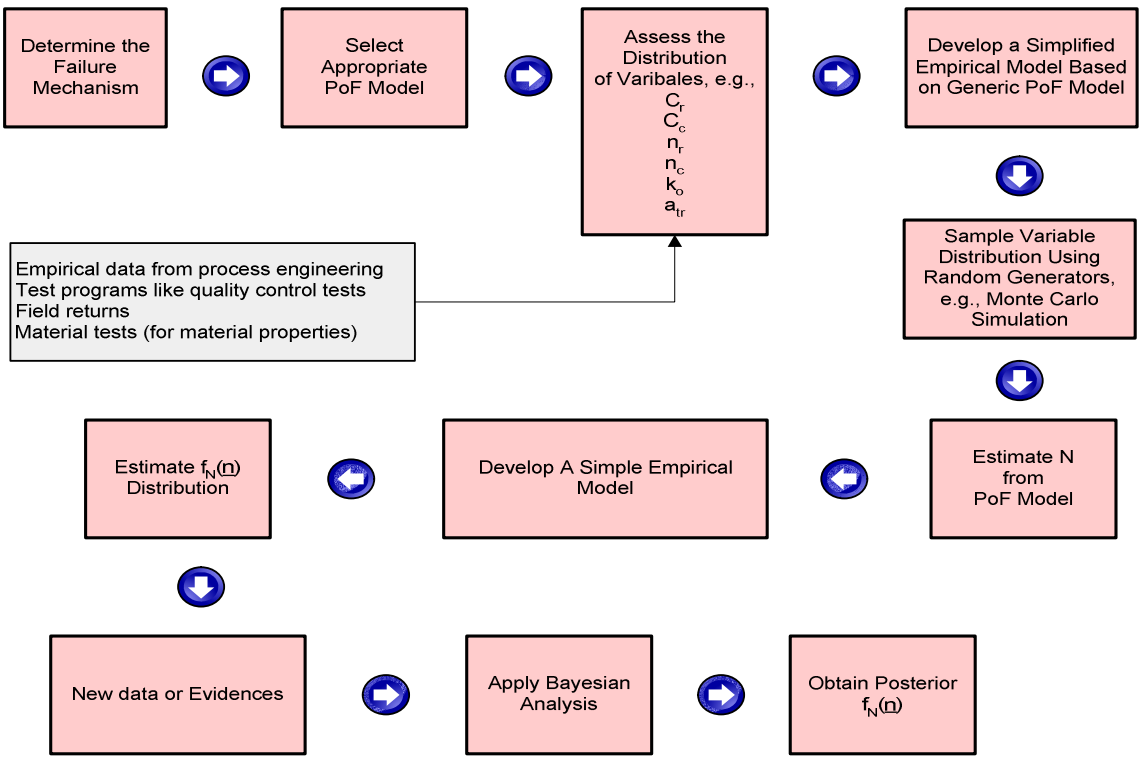

Figure 3.1. Flow Diagram for the Computational Methodology.

1. Failure Mechanism Determination

Pipelines in the refinery undergo several degrading mechanisms. Corrosion accounts for the major source of this degradation, while fatigue cracking has also accounted for many failures in the past few years. Extensive studies focusing on these degradation mechanisms separately have been conducted, producing quite number of life estimating models. However, the predictions of these models had many limitations, causing over- or under-estimation of the life predicted for the pipelines. In the past, the interaction of the different degradation mechanisms in the pipelines and the need to build physical models capable of representing such interactions has been overlooked. The effort of this research, then, was to focus on one type of interacting degradations that has major

negative consequences to the refinery (see Figure 3.2). The corrosion-fatigue-interaction degradation mechanism was selected after a careful review of the literature and discussion with refinery personnel. The pipelines failures due to corrosion-fatigue tend to go unpredicted for many reasons:

- The initiation site of the crack is difficult to locate, and hence the degradation grows unpredictably.
- The limitation of the inspection techniques hinders the discovery of the exact initiation of the crack and the tracing of it.
- The lifespan of the degradation can either be long or short, depending on the exact nature of the degradation site and environment.

Therefore, this research focused on studying and probabilistically modeling the corrosion-fatigue degradation mechanism.

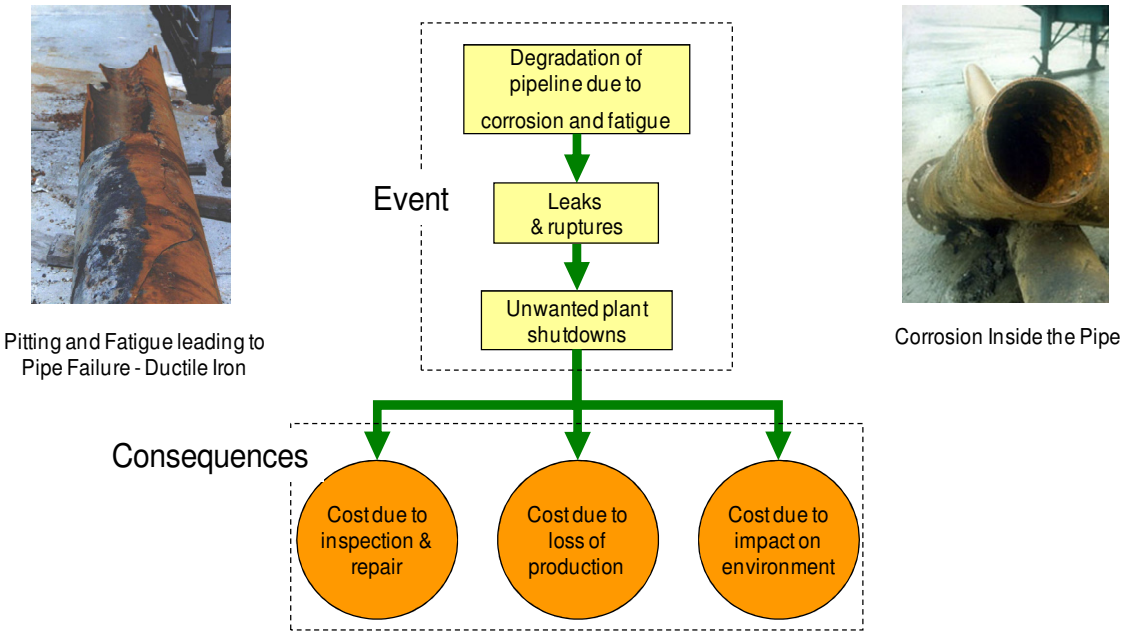

Figure 3.2. Sequence of Events and Consequences for Pipeline Corrosion-Fatigue Degradation Failure.

2. Physics-of-Failure Model Selection

This step called for a thorough literature review for all efforts exerted in the corrosion-fatigue field. Chapter 1 summarizes the most popular physical models. All of the models existing in the literature are under debate due to many factors; however a few have succeeded in acquiring partial support for demonstrating successful predictions within acceptable limitations. The superposition model developed by R.P. Wei [41] has gained substantial support for its ability to satisfactorily predict life estimates for many mechanical structures, including pipelines. Wei's research was backed by many experiments over many years that were competent in validating the proposed superposition model. Hence, this research adopted the superposition model to construct a simple empirical model that could be probabilistically analyzed and validated.

3. Variable Selection

The variables are important in deciding how the computation will be executed. Hence, the most significant variables to the corrosion-fatigue phenomenon were carefully selected. These variables went through a minimization process to reduce the full range of variables utilized in the superposition model computation to the needed size. The next section elaborates on the selection, categorization, and assessment of the variables.

4. Empirical Model Development

This was the core step in the research. Building an empirical model based on an existing physical model was a challenging task. The following criteria, as discussed in the objectives of this dissertation, were reflected in the proposed empirical model:

- The model should be able to reproduce the adopted physics-of-failure model results with the least margin of errors.
- The simplest form should be adopted, yet it must be physically sound.
- The random variables should be minimized for probabilistic analysis to be achievable. Also, the deterministic variables should closely represent the environmental and physical parameters of the pipelines.
- Probabilistically the model can be analyzed and validated.

Details of the empirical model development procedure are given in a subsequent section.

5. Monte Carlo Simulation

Random variables are important to the computation part of this research. To generate random variables, a Monte Carlo simulation was performed using MATLAB. Figure 3.3 depicts the simulation outcome for the crack size versus number of cycles to pipeline complete failure (crack through pipeline wall thickness). The expected distributions for many parameters are indicated on the figure to assist in the probabilistic analysis and evaluation.

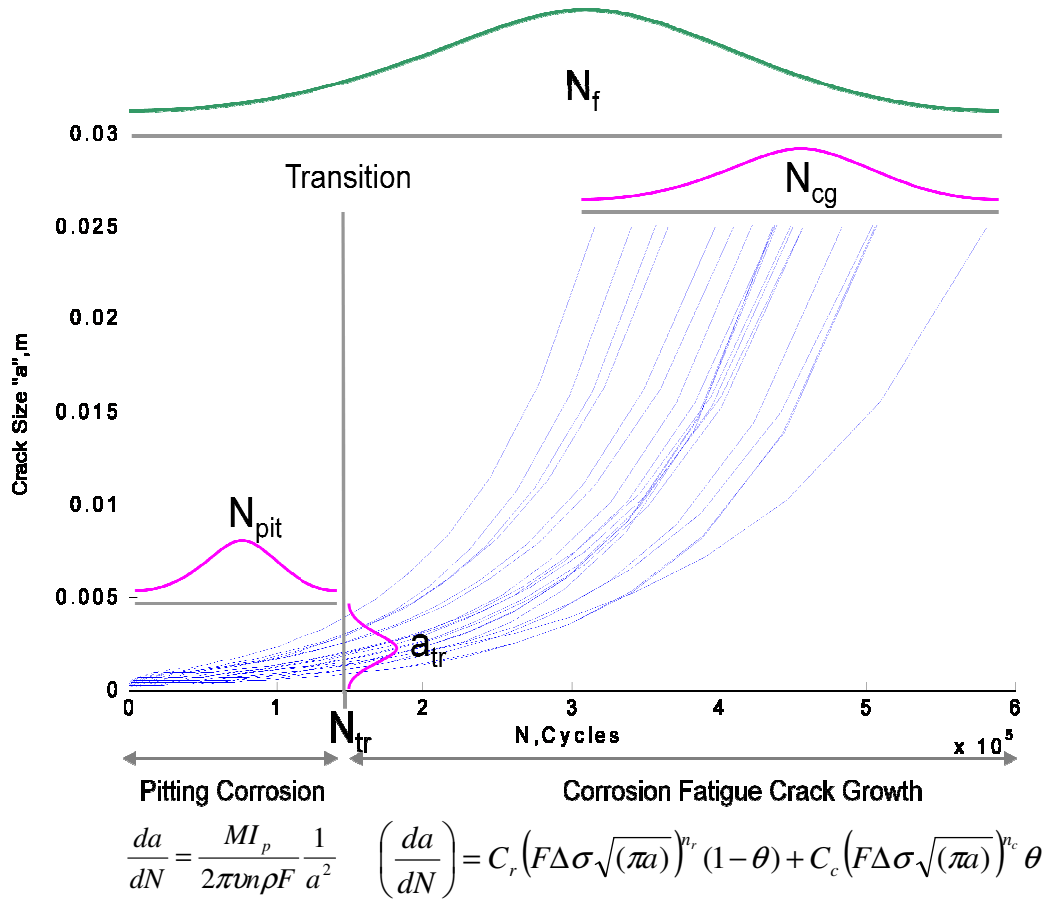

Figure 3.3. Monte Carlo Simulation Outcome from MATLAB with the Expected Distributions.

6. Estimating “N” from PoF Model

This step utilized the produced random data from the Monte Carlo simulation to calculate the life estimate “N, number of cycles” versus damage “a, crack size.” Basically, this step was a reproduction of Wei’s superposition model outputs that aided in proposing the structure of the empirical model.

7. Develop a Simple Empirical Model

The graphical representation of the Monte Carlo simulation guided in determining the most suitable structure for the empirical model with the criteria set in the objective of this research. Subsequent sections will detail this step extensively.

8. Probabilistic Analysis

The last four steps comprised the probabilistic evaluation of the proposed empirical model. Firstly, the empirical model was cross-checked probabilistically against the benchmark model, the superposition model. Secondly, the distributions of the damage, a, and the empirical model parameters were estimated using the generic data produced from Monte Carlo simulation. Lastly, these distributions were updated, utilizing either the collected field data or experimental data. The Bayesian analysis assisted in performing the aforementioned validation and estimation. Yet again, the computation burden exerted by the Bayesian analysis to perform the numerical integration mandated the use of computer programming. Thus, WinBUGS software program assisted in carrying out the necessary Bayesian analysis computation.

3.4 *Selection of Variables*

Tables 3.1 and 3.2 contain the variables that were selected in this research to be either deterministic parameters or uncertain parameters represented by a probability density function. The selection was mainly subjective but was influenced by the parameters that most influence the final result; the ultimate selection would be decided upon data availability.

Table 3.1. Deterministic Parameters of the Mechanistic Model for X70 Steel Piping.

Variable	Value
Universal gas constant	R = 8.314 J/mol-K
Activation energy	E_a = 35 KJ/mol
Fatigue exponent	n_r = 2
Corrosion-fatigue exponent	n_c = 2
Frequency	ν = 0.1 - 10 Hz
Applied stress range	$\Delta\sigma$ = 100 - 500 Mpa
Temperature	T = 293 - 723 K
Corrosion Current	$I_p = 1\times10^{-6}$ - 1×10^{-4} A
Final crack size	a_f = 25 mm
Shape Factor	β = 1.24
Faraday's constant	F = 96,514 C/mole
Molecular weight	M = 55 g/mole
Valence	η = 3
Density	ρ = 7.87 g/cm^3

Table 3.2. Uncertain Parameters of the Mechanistic Model (Represented by the Weibull Distribution) for X70 Steel [43].

Random Variable	β (shape factor)	α (scale factor)	γ
C_r	12	4.0×10^{-11}(m/cyc)(MPa$\sqrt{m}$)$^{-2}$	0
C_c	8	2.0×10^{-10}(m/cyc)(MPa$\sqrt{m}$)$^{-2}$	0
κ_o	10	3.0×10^{5} (s^{-1})	0

Deterministic variables are generic in nature and can be found in the open literature. Activation Energy, E_a, is treated to be deterministic in this research by reasonably assuming Arrhenius equation is valid within the selected condition regime [64] and leaving reaction rate constant, k_o, to represent the variability. In line with the on-going practice, n_r and n_c, the fatigue and corrosion-fatigue exponents, were chosen to be deterministic. For carbon steel alloys n_r and n_c were estimated to be 2 [25]. On the other hand, the selected random variables were c_r, c_c, and k_o: the fatigue coefficient, corrosion-fatigue coefficient, and the reaction rate constant, respectively. These variables are mechanistically and statistically independent of time [62]. The variability in material properties is represented in c_r and c_c. Finally, k_o variability represents the crack-tip chemistry (nature and concentration of ionic species) and electrochemical conditions (pH and electrode potential) [43].

3.5 *Monte Carlo Simulation*

The initial stage of this research was to simulate the results from the selected benchmark superposition model. In this simulation many equations needed to be solved using

different criteria and the selected variables in the proceeding section. The following equations and criteria were solved to obtain the life estimate versus extent of damage for the pipeline:

- The transition point from pitting corrosion to fatigue crack growth needed to be determined initially to aid in subsequent calculations. As mentioned before, the transitional criteria were

$$\left(\frac{da}{dt}\right)_{pit} = \left(\frac{da}{dt}\right)_{crack}$$

  So, transition occurs when the rate of pit growth rate equals the crack growth rate at the onset of crack growth. a_{tr}, is calculated from this criteria by solving Equation 2.33.

- Following the estimation of a_{tr}, the integration of $\left(\frac{da}{dt}\right)_{pit}$ in Equation 2.3 was calculated from initial value of a_o equal to zero to a_{tr}. The value of N_{tr} was estimated from this step.
- Now the superposition weight factor θ, Equation 2.26, was estimated, which was critical for the following computational step.
- With θ value in hand, the fatigue crack growth size, N_{cg}, was determined by solving Equation 2.32.
- The desired outcome was furnished at this step with the final number of cycles, N_F, corresponding to the crack through of the pipeline. N_F is the summation of N_{tr} and N_{cg}, Equation 2.34.

- Graphical representation of the outcomes mainly N vs. a was produced. This was the most important starting point in the research and served in proposing the desired simple empirical model.

3.5.1 **MATLAB Routine Program**

A computer routine was written in MATLAB to carry out the computations involved in sampling the random variables. The input for the number of curves was opted as arbitrary for a higher figure to increase the amount of data available to produce refined distributions of the desired parameters. Furthermore, the environmental factors were chosen at arbitrary from a broad spectrum of operating conditions to impersonate the use and accelerated levels for a pipeline in a refinery. Figure 3.4 portrays the general flow of the MATLAB program with all key calculations aimed to produce the desired data and plots.

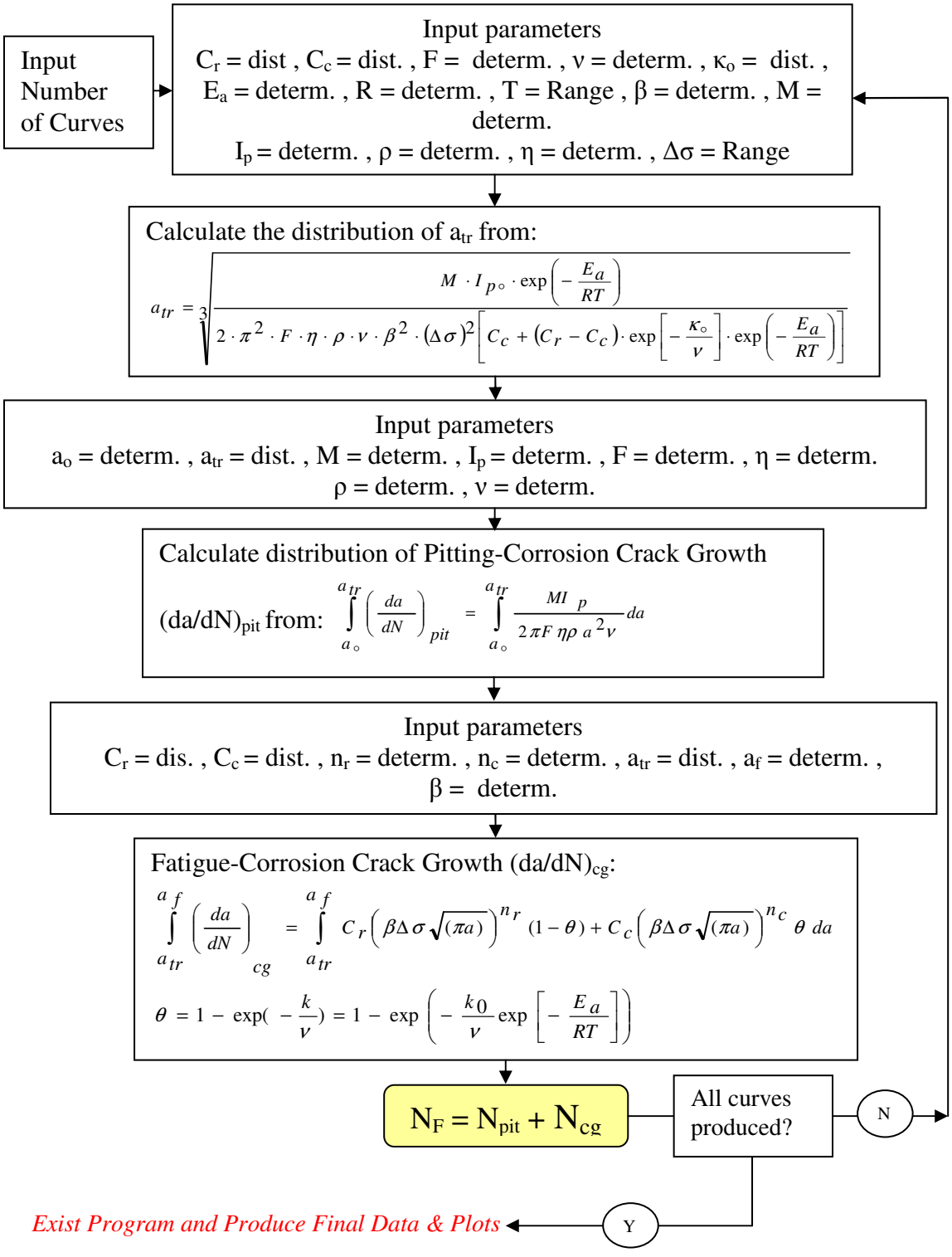

Figure 3.4. MATLAB Program Algorithm of the Simulation-Based Solution.

3.5.2 **Simulation Outcome**

The following two Figures, 3.5 and 3.6, illustrate the final outcomes for one of the simulations conducted in the MATLAB program.

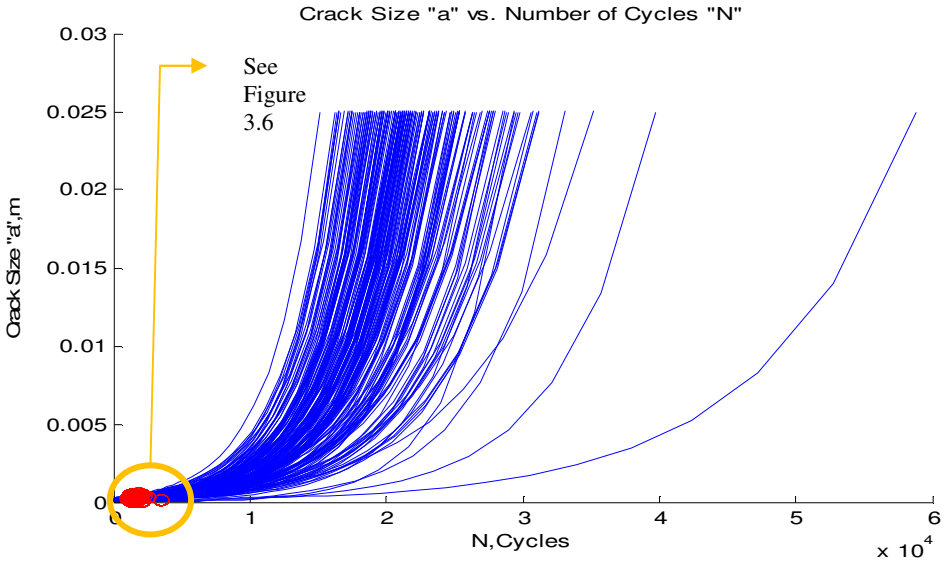

Figure 3.5. Results of the Simulation Using Wei's Model.

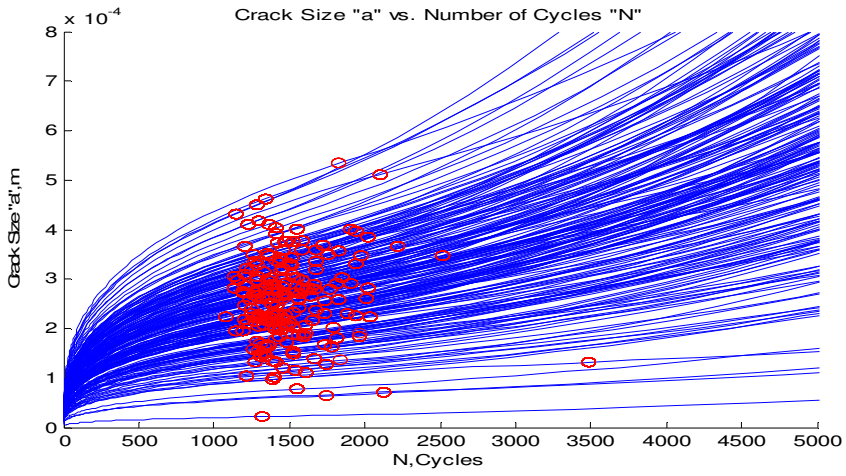

Figure 3.6. Zoomed Area for the Coordinates (Ntr, atr) to Show the Transition Points.

Figure 3.6 presents a close-up for the transitional area for all curves as indicated by the red dotted circles.

The simulation generated 200 lines for crack size versus number of cycles. The program was set for a pre-determined final crack size as shown in Figure 3.5, in which all the lines cut off at one particular value of crack size. However, the variability in the outcomes was achieved, as is obvious from the non-uniform distribution of the curves. Figure 3.6 clearly shows how the transitional point for crack sizes varies for each curve. So, at a particular number of cycles, one would find the distribution of crack size, which reflects the variability in the inputs of the simulation program. Hence, the program successfully reproduced the anticipated outcomes for the superposition Wei's model. What remained was to use this outcome to determine the simplest empirical model that could represent the same effect of that for the superposition model.

3.5.3 **Modeling Corrosion-Fatigue Structure**

This section presents the core of this research, since it details the steps undertaken to propose the structure of the simplest empirical model possible that would condense the long range of steps in the superposition model programming. The goal was to propose one simple empirical model that could achieve the same results as the superposition model, yet use as few input parameters as possible so that probabilistically the model could be evaluated and verified. The following subsections highlight the steps taken to propose the desired empirical model structure.

3.5.3.1 **Assumptions**

It was vital to set some assumptions straight prior to commencing the efforts to propose the desired simple empirical model. Besides the general aforementioned assumptions, the following assumptions helped ease the proposal task:

- Curve-fitting the superposition model simulation outcome presents the most adoptive method to narrow down the size of proposed model.
- The model is mainly for high strength carbon steel pipeline, here X70. Other pipeline material would call for model updating and a new simulation of the superposition model.
- The selection of the deterministic parameters in the proposed empirical model is subjective and mainly related to the pipeline operation and inspection/maintenance history.
- The selected deterministic variables in the proposed empirical model are assumed to be independent, and no correlation exists between them.
- The random variables of the proposed empirical model represent the variability of all effects other than the selected deterministic variables.
- The remaining deterministic variables in Table 3.1 are assumed to be condensed within the proposed empirical model random parameters.

3.5.3.2 **Model Structure Proposal**

The outcome curves of the superposition model simulation from MATLAB were utilized in defining the structure of the intended empirical model structure. Figure 3.7 shows the simulation outcome of one curve only, which assisted in the curve-fitting process.

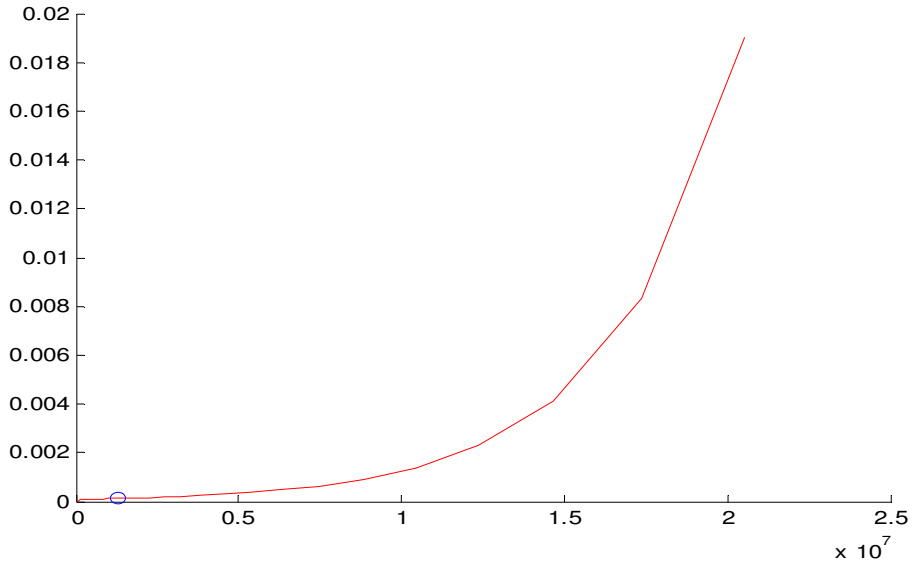

Figure 3.7. The Simulation Outcome for a Single Curve for T=673K, σ=20MPa, ν=7 Hz, and Ip=1×10^{-6}.

From MATLAB, the transitional number of cycles, N_{tr}, is 1.2744×10^{6} number of cycles, and the transitional crack size, a_{tr}, is 1.2802×10^{-4} meters. In Figure 3.7 this transitional point is indicated by a blue circle. Many attempts were applied via trial and error to fit the above curve by a single empirical equation, but these attempts deemed unsuccessful. This failure of this attempt was mainly because we had two degradation processes contributing to this curve. Pitting corrosion as the crack initiating phenomenon formed the first left portion of the curve before the transition point, while the subsequent process of corrosion-fatigue crack growth formed the second right part of the curve. Hence, the

attempt was geared instead toward splitting the curve fitting to accommodate the two major degradation processes in-hand. First, the corrosion pitting part was curve-fitted up to the transition point. Figure 3.8 shows the exploded view for the left portion of the curve for the corrosion-pitting degradation process. The line beyond the transitional point has been extended as a black dotted line to reflect the continuation process for the corrosion pitting if it had been the only degradation mechanism.

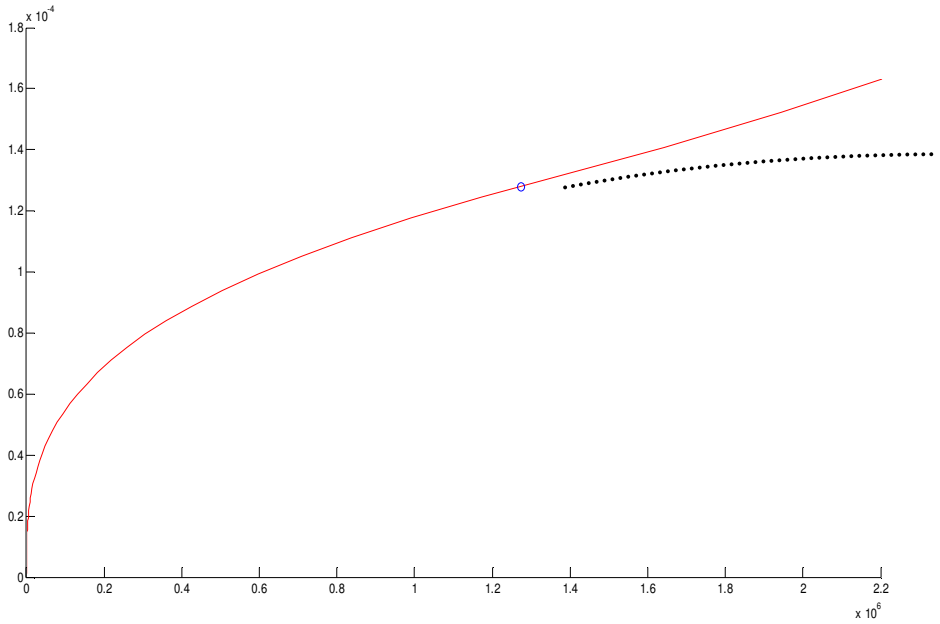

Figure 3.8. Left Portion of the Curve Representing the Pitting Corrosion Process.

The attempt by trial and error to curve-fit this portion of the curve revealed the following relation:

$$a = \alpha \cdot N^{1/3} \qquad 3.1$$

This relation was examined for many curves of the simulation, and all were consistent in giving the same relation. A review of the literature for this finding confirms Hoeppner [125], which states the following relation:

$$t = \left(\frac{d}{c}\right)^3 \tag{3.2}$$

where t is the time, d is the pit depth, and c is a material/environment parameter.

With no further attempts, the first portion was found and was quite consistent with a well-known physical equation.

The same method for curve-fitting was pursued for the next portion to the right of the transitional point representing the corrosion-fatigue crack growth. Figure 3.9 shows the exploded view for the right portion of the curve where the bottom portion beyond the transitional point has been extended as a black dotted line to show how the curve should behave if corrosion-fatigue were the only degrading process.

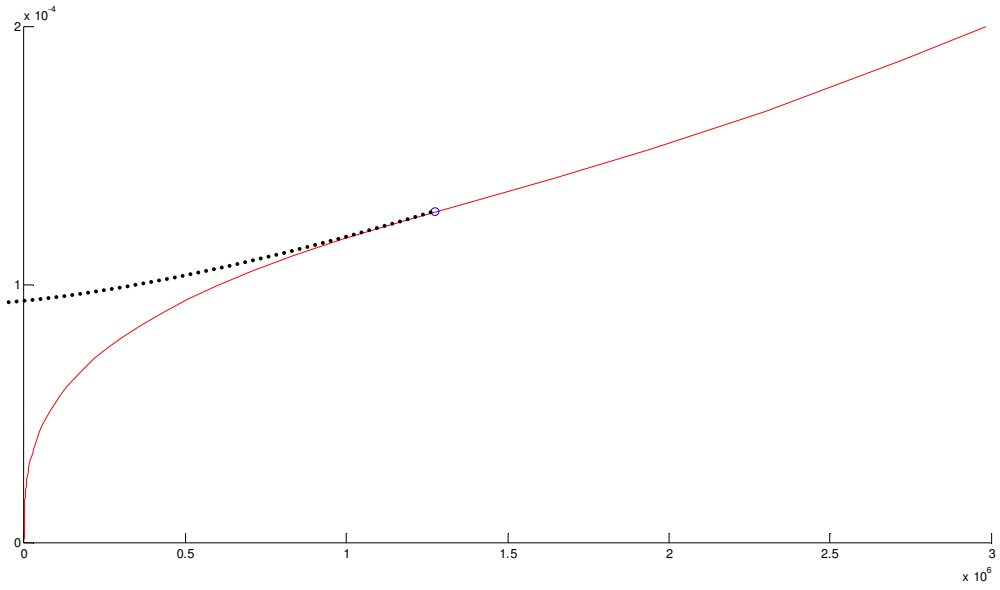

Figure 3.9. Exploded View for the Right Portion of the Curve Representing the Corrosion-Fatigue Crack Growth Degradation Process.

Once more, trial and error revealed the following relation while curve-fitting the right portion of the curve:

$$a = \beta \cdot e^{\gamma N} \qquad 3.3$$

So, the corrosion-fatigue crack growth process increased exponentially beyond the transitional point from the pit, which had grown to the transitional pit size by a power relation of 1/3. It can be seen from the simulation curves that the pitting corrosion consumes the least amount of time, in our case it was 1.2744×10^{6} number of cycles, while the corrosion-fatigue crack growth consumes 1.9247×10^{7} number of cycles, which is an order of magnitude. This is because the pit normally forms faster and grows to the transitional size in a shorter period of time due to the harsh environment and the nature of the pitting corrosion. From Figure 3.8 it is clear how the curve before the transitional

point jumps initially to a particular size and then reaches an optimum size beyond which the growth is minimal. On the other hand, corrosion-fatigue, occupying the second part of the sigmoidal curve, grows gradually at slower pace than the pit growth rate. However, toward the end it shoots up, resembling the brittle fracture as per the third part of the sigmoidal curve.

Now, a combined relation of the above Equations 3.1 and 3.3 was needed to obtain a single relation that represented empirically the overall phenomenon. Figure 3.10 illustrates the different points used to aid in the combination process.

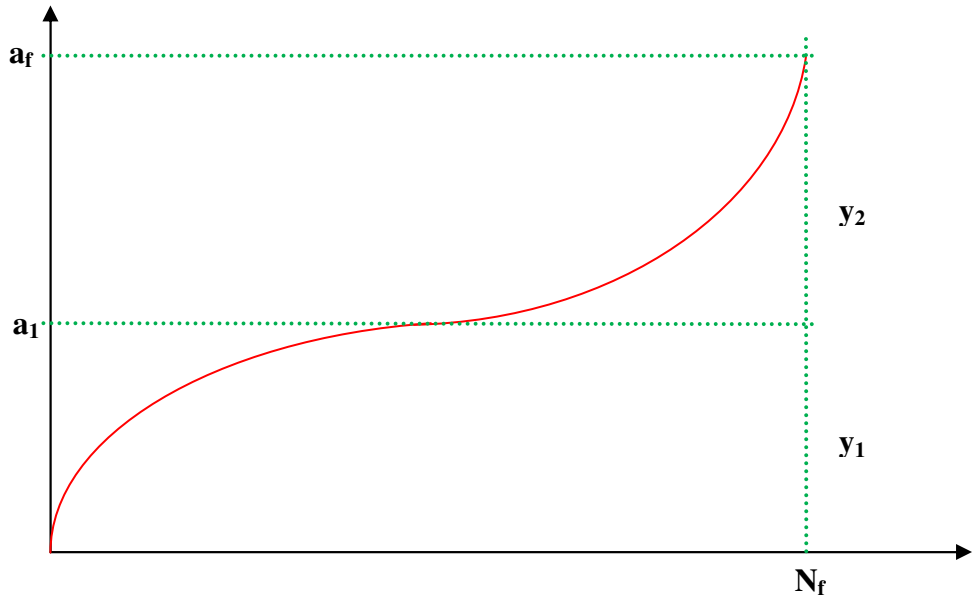

Figure 3.10. Illustration for the Different Coordinate Points Employed in the Combination Process.

From the simulation we get

$$a_f = 0.025\ m$$

while from Equation 3.3 and Figure 3.10 we get

$$a_2 = \beta \cdot e^{\gamma N}$$

By substitution we get

$$0.025 = \beta \cdot e^{\gamma N}$$

$$\frac{0.025}{\beta} = e^{\gamma N}$$

$$ln\frac{0.025}{\beta} = \gamma N$$

$$N_f = \frac{1}{\gamma} ln\frac{0.025}{\beta}$$

From Figure 3.10 we get

$$a_1 = \alpha \cdot N^{1/3}$$

By substitution we get

$$a_1 = \left(\frac{1}{\gamma} ln\frac{0.025}{\beta}\right)^{1/3} \equiv y_1$$

So,

$y_1 + y_2 = 0.025 \Rightarrow y_2 = 0.025 - y_1$

By substitution,

$y_2 = 10^{-14} \cdot C_2 \cdot N^2 \cdot e^{0.45451\times10^{-5}\cdot N}$

So, the combined empirical equation is

$$a = A \cdot N^{1/3} + B \cdot N^2 \cdot e^{C\cdot N} \qquad 3.4$$

where C ≡ 0.4545×10^{-5}

Hence Equation 3.4 represents the most general form for the simple empirical model structure. C_1 and C_2 are the only random parameters of the empirical model. These values were determined experimentally and in our case using the generic data from Wei's superposition model to get an initial indication of their value. To cross-check their value with the simulation outcome, Equation 3.4 was applied to the same conditions, and the following Figure 3.11 was obtained.

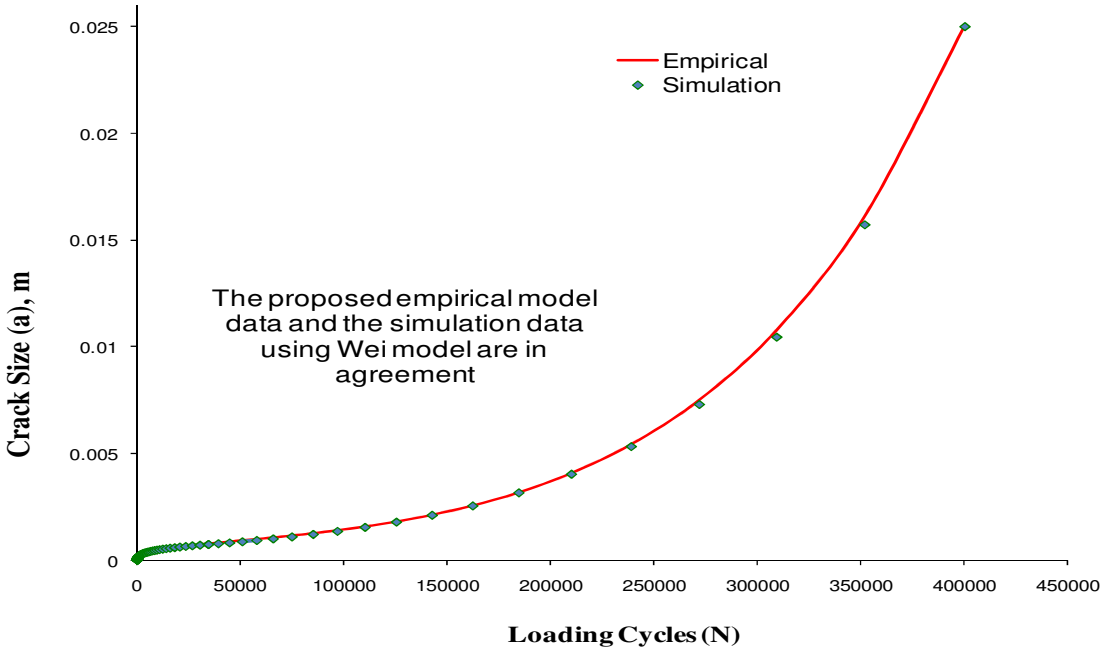

Figure 3.11. Demonstration of the General Simple Empirical Model Against Wei's Superposition Model.

Clearly, the proposed empirical model agreed with Wei's model, indicating a successful proposal.

3.5.3.3 Application of Environmental Factors

The general simple empirical form for the corrosion-fatigue was successfully obtained in Equation 3.4. This form had to be extended to include the critical physical parameters of the pipeline under operation, such as

- Loading stress "σ"

- Loading frequency “ν”
- Temperature “T”
- Flow characteristics “C” (e.g., chloride concentration, sulfur concentration, viscosity, corrosion current)

To include such pipeline operating conditions into the proposed empirical model, we adopted a simple straightforward approach. Correlations for the proposed empirical model’s three parameters A, B, and C were carried out against the physical conditions. Only the last physical condition, “flow characteristics,” was presented through the corrosion current, Ip, which yielded the chloride and sulfur concentrations. The other flow characteristics of the pipeline were assumed to have a negligible effect as compared to the chloride and sulfur concentration (this is discussed in detail in Chapter 2). Each correlation updated the proposed empirical model once, and this updating was carried out to the next physical parameter correlation process. In addition, the range for each physical parameter stretched to include the pipeline operating condition range as well as the experimental condition range (accelerated). Hence, the correlation mission assumed a cumulative approach in order to reach to the most feasible comprehensive empirical model. The correlation was conducted for only the 50^{th} percentile of all distributed parameters in the superposition simulation outcome. In all cases, a baseline operating condition for all cases was selected from which each physical parameter correlation started. Here, at each correlation, only the correlated physical parameter was varied while the others remained constant. In our case the following conditions were selected:

T = 373 K ;

$\nu = 3$ Hz ;

$\sigma = 100$ MPa ;

$Ip = 1 \times 10^{-6}$ A

3.5.3.3.1 *Temperature "T" Effect Correlation*

The physical parameter of the operating pipeline "temperature" was correlated with the proposed empirical model's three parameters A, B, and C. Table 3.3 displays the temperature range used here and the corresponding values for the three parameters of the proposed empirical model. For each set of conditions, the outcome of the superposition simulation at the 50^{th} percentile was obtained. This outcome was then used to calculate the parameters of the empirical model through an optimization process, which minimized the error value between the superposition model outcome and the proposed empirical outcome. Later, the data points corresponding to each parameter against the temperature range were curve-fitted to determine whether a correlation existed and if it did, how it could be best represented.

Table 3.3. Temperature Range versus the Proposed Empirical Model Parameters.

T (K)	A	B	C
273.0	9.3575E-14	8.5362E-16	5.7552E-06
345.7	1.3892E-11	8.5406E-16	5.7545E-06
418.4	2.2165E-06	6.9981E-16	6.0374E-06
491.1	5.4454E-06	5.2727E-16	6.4389E-06
563.8	9.3576E-14	8.5367E-16	5.7552E-06
636.5	1.3870E-11	8.5367E-16	5.7552E-06
709.2	2.7644E-10	8.5419E-16	5.7543E-06
781.9	5.1043E-12	8.5358E-16	5.7554E-06
854.6	1.3877E-11	8.5392E-16	5.7548E-06
927.3	2.7946E-10	8.5363E-16	5.7552E-06
1000.0	1.3862E-11	8.5358E-16	5.7553E-06

This correlation resulted in the following:

- No correlation was found between temperature and all three parameters of the proposed empirical model A, B, and C.
- The reason there was no correlation is that in the superposition modeling simulation the crack size "a" is related to temperature, $a \sim \exp(1/T) \approx 1$. So, no matter what value T takes, it has no impact on A, B, or C.

Hence, the proposed empirical model remained the same as in Equation 3.4 and was used in the following correlation versus loading stress "σ".

3.5.3.3.2 *Loading Stress "σ" Effect Correlation*

The physical parameter of the operating pipeline "loading stress" was correlated with the proposed empirical model's three parameters A, B, and C. Table 3.4 displays the loading stress range used here and the corresponding values for the three parameters of the proposed empirical model. Similarly to the case of temperature correlation, the produced values displayed in the table correspond to the 50th percentile curve.

Table 3.4. Loading Stress Range versus the Proposed Empirical Model Parameters.

σ (MPa)	A	B	C
1	1.5223E-06	3.3416E-22	4.2201E-10
5	1.6140E-06	5.6680E-20	1.2235E-08
10	1.6910E-06	5.0457E-19	5.1901E-08
15	1.7498E-06	1.8072E-18	1.2050E-07
20	1.7987E-06	4.4633E-18	2.1879E-07
25	1.8413E-06	8.9964E-18	3.4722E-07
30	1.8795E-06	1.5948E-17	5.0616E-07
40	1.9472E-06	3.9329E-17	9.1684E-07
50	2.0025E-06	7.9325E-17	1.4519E-06
100	2.2166E-06	6.9975E-16	6.0377E-06
200	2.5027E-06	6.1932E-15	2.4979E-05
300	2.7094E-06	2.2201E-14	5.7213E-05
500	3.0024E-06	1.1122E-13	1.6220E-04
800	3.3432E-06	4.9140E-13	4.2230E-04
1000	3.5252E-06	9.9368E-13	6.6507E-04

This correlation resulted in the following:

- Parameter A versus loading stress had the following correlation:

$$A \sim \sigma^{0.182} \quad 3.5$$

Figure 3.12 displays the resulting curve fit for the loading stress range against parameter A's values.

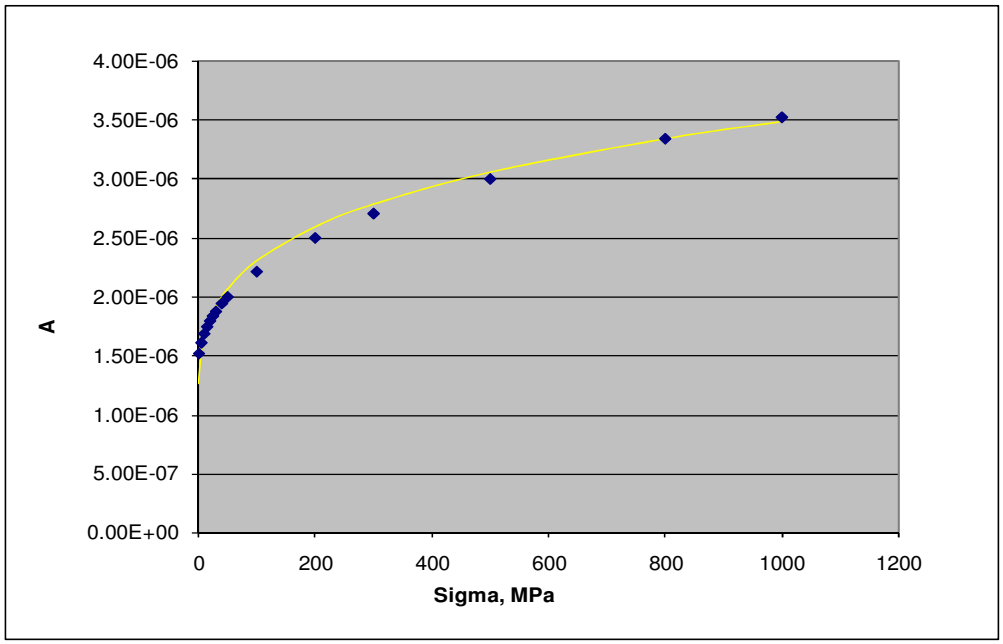

Figure 3.12. Plot of Loading Stress Values versus Empirical Model Parameter A Values.

- Parameter B versus loading stress had the following correlation:

$$B \sim \sigma^{3.24} \quad 3.6$$

Figure 3.13 displays the resulting curve fit for the loading stress range against parameter B's values.

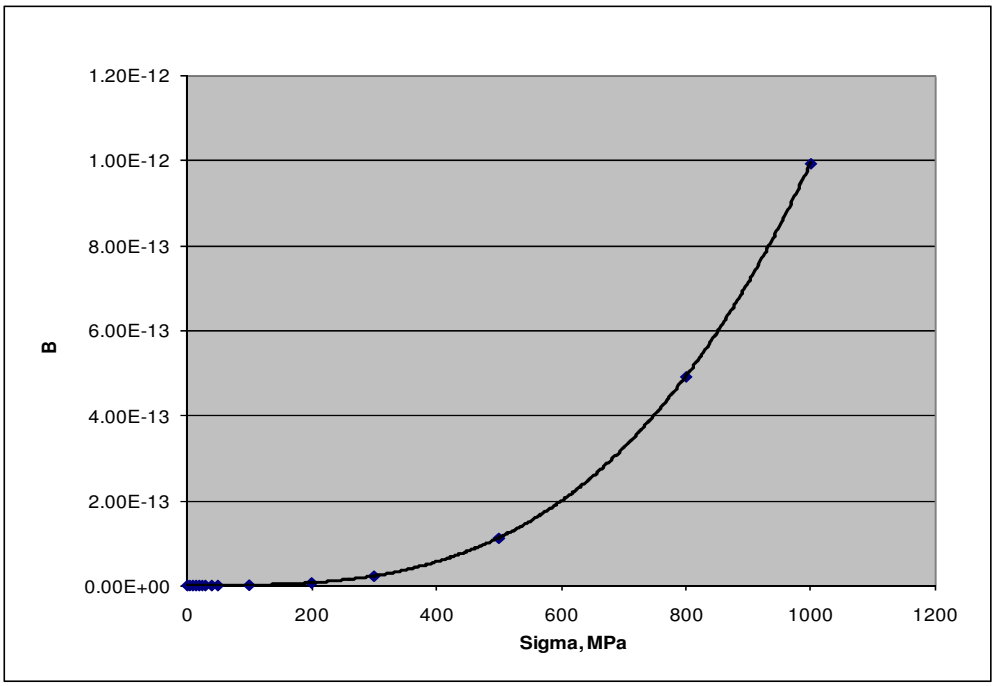

Figure 3.13. Plot of Loading Stress Values versus Empirical Model Parameter B Values.

- Parameter C versus loading stress had the following correlation:

$$C \sim \sigma^{2.062} \qquad 3.7$$

Figure 3.14 displays the resulting curve fit for the loading stress range against parameter C's values.

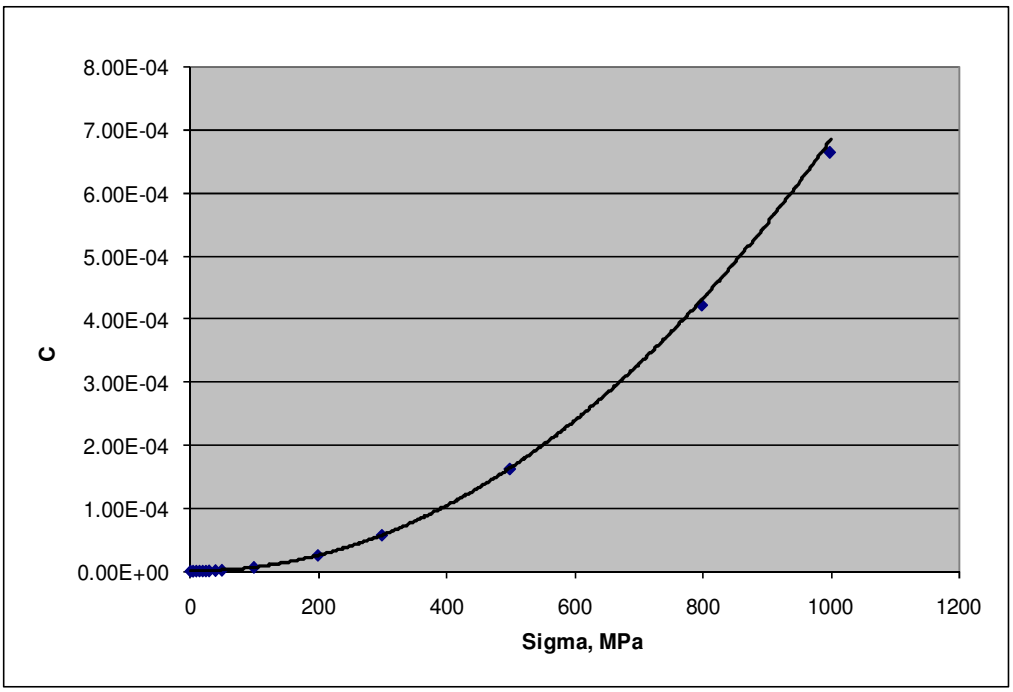

Figure 3.14. Plot of Loading Stress Values versus Empirical Model Parameter C Values.

Hence, with the above correlations for the loading stress with the proposed empirical model three parameters A, B, and C, the proposed empirical model in Equation 3.4 was updated as follows:

$$a = A \cdot \sigma^{0.182} \cdot N^{1/3} + B \cdot \sigma^{3.24} \cdot N^2 \cdot e^{4\times10^{-10}\cdot\sigma^{2.062}\cdot N} \quad 3.8$$

Next, this equation was carried out for the next correlation against the loading frequency parameter.

3.5.3.3.3 *Loading Frequency "v" Effect Correlation*

The physical parameter of the operating pipeline "loading frequency" was correlated with the proposed empirical model three parameters A, B, and C. Table 3.5 displays the loading frequency range used here and the corresponding values for the three parameters of the proposed empirical model. Similarly to the case of temperature and loading stress correlations, the produced values displayed in the table correspond to the 50^{th} percentile curve.

Table 3.5. Loading Frequency Range vs the Proposed Empirical Model Parameters.

v (Hz)	A	B	C
1.00E-07	2.6685E-04	3.9824E-20	2.8601E-10
1.00E-06	1.2079E-04	6.6986E-20	3.7159E-10
1.00E-05	5.5864E-05	3.4487E-20	3.2118E-10
1.00E-04	2.5854E-05	1.6710E-20	3.0407E-10
1.00E-03	1.2255E-05	6.9062E-21	3.3393E-10
1.00E-02	5.9965E-06	2.6659E-21	3.7181E-10
0.1	3.0507E-06	9.9935E-22	4.0803E-10
1	1.6191E-06	3.7170E-22	4.3989E-10
3	1.2158E-06	2.3209E-22	4.5342E-10
10	8.9239E-07	1.3892E-22	4.6696E-10
50	6.0274E-07	7.0418E-23	4.8300E-10
100	5.3099E-07	5.2482E-23	4.8961E-10
200	4.3878E-07	3.9483E-23	4.9518E-10
400	3.7936E-07	2.9405E-23	5.0144E-10
600	3.4981E-07	2.4898E-23	5.0448E-10
800	3.2163E-07	2.2164E-23	5.0646E-10
1000	3.2813E-07	2.0069E-23	5.0872E-10

This correlation resulted in the following:

- Parameter A versus loading frequency had the following correlation

$$A \sim \nu^{-0.288} \qquad 3.9$$

Figure 3.15 displays the resulting curve fit for the loading frequency range against parameter A's values (the logarithmic scale is applied to improve the display of points and the fitting curve).

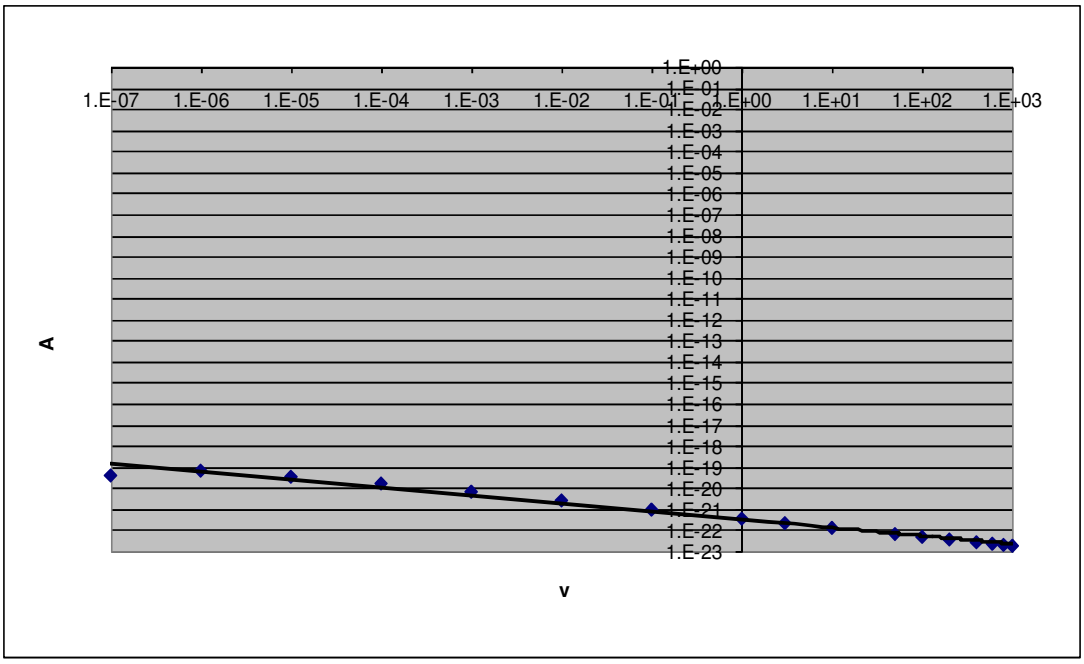

Figure 3.15. Plot of Loading Frequency Values versus Empirical Model Parameter "A" Values on Logarithmic Scale.

- Parameter B versus loading frequency had the following correlation:

$$B \sim \nu^{-0.377} \qquad 3.10$$

Figure 3.16 displays the resulting curve fit for the loading frequency range against parameter B's values.

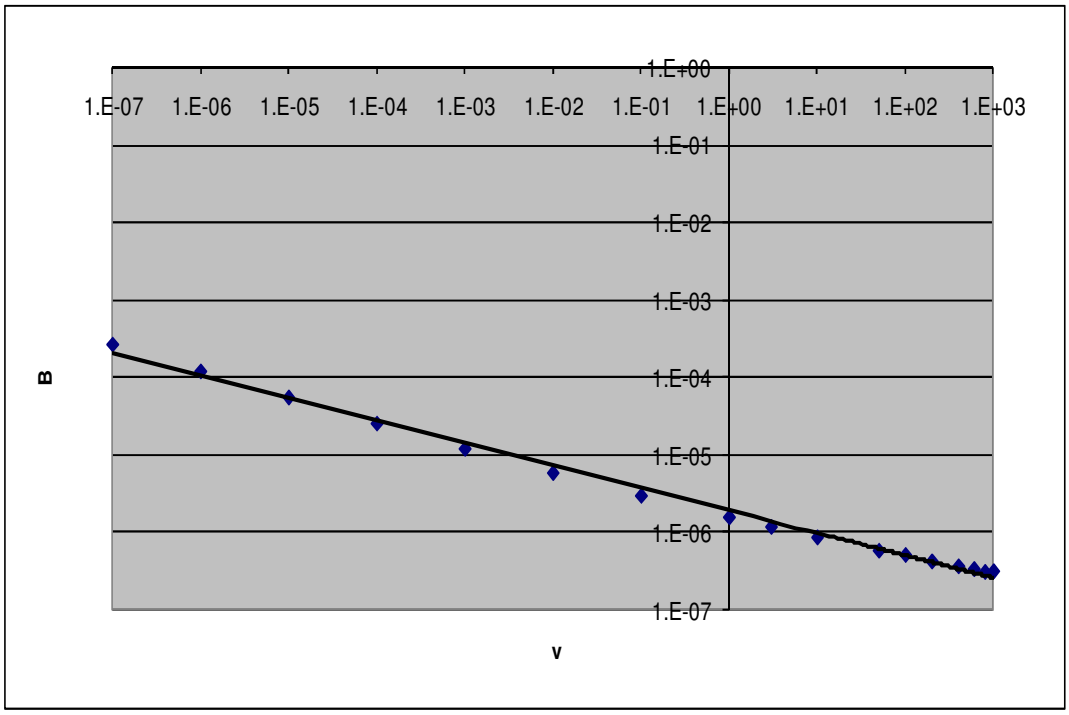

Figure 3.16. Plot of Loading Frequency Values versus Empirical Model Parameter B Values on Logarithmic Scale.

- Parameter C versus loading frequency had the following correlation:

$$C \sim \nu^{0.024} \qquad 3.11$$

Figure 3.17 displays the resulting curve fit for the loading stress range against parameter B's values.

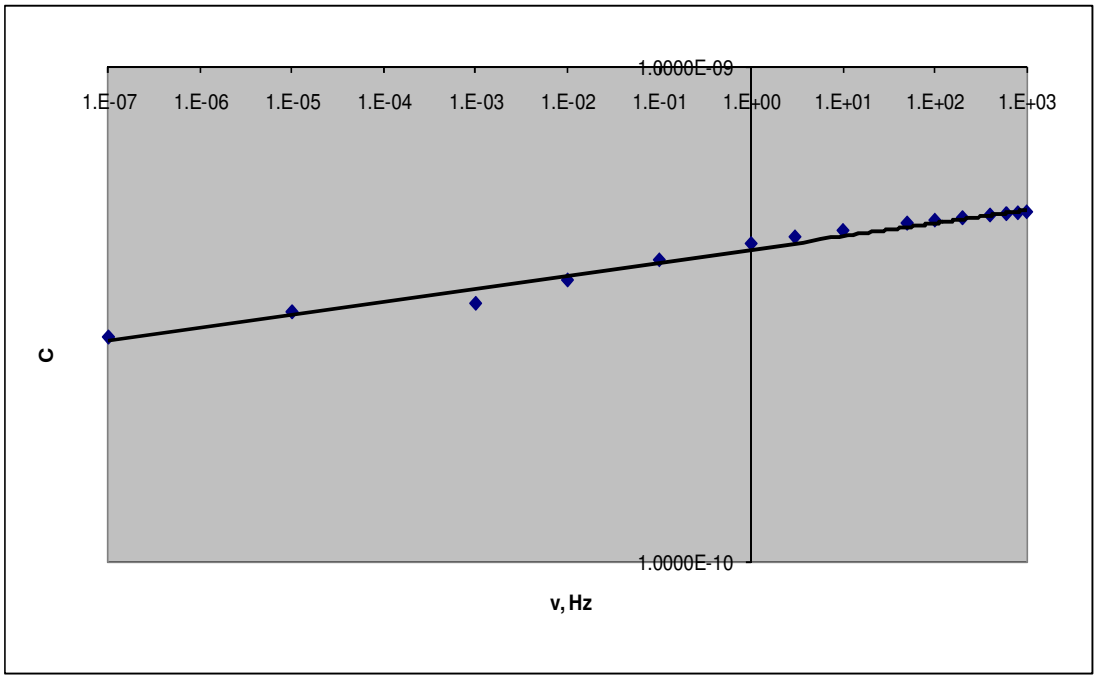

Figure 3.17. Plot of Loading Frequency Values versus Empirical Model Parameter C Values on Logarithmic Scale.

Hence, with the above correlations for the loading frequency with the proposed empirical model's three parameters A, B, and C, the empirical model was further updated as follows:

$$a = A \cdot \sigma^{0.182} \cdot \nu^{-0.288} \cdot N^{1/3} + B \cdot \sigma^{3.24} \cdot \nu^{-0.377} \cdot N^{2} \cdot e^{4\times10^{-10}\cdot\sigma^{2.062}\cdot\nu^{0.024}\cdot N} \qquad 3.12$$

Next, this equation was carried out for the next correlation against the corrosion current parameter.

3.5.3.3.4 *Corrosion Current "I_p" Effect Correlation*

The physical parameter of the operating pipeline "corrosion current" was correlated with the proposed empirical model three parameters A, B, and C. Table 3.6 displays the loading frequency range used here and the corresponding values for the three parameters of the proposed empirical model. Similarly to the case of temperature and loading stress correlations, the produced values displayed in the table correspond to the 50th percentile curve.

Table 3.6. Corrosion Current Range vs the Proposed Empirical Model Parameters.

Ip (A)	A	B	C
1.00E-12	7.2549E-08	1.2398E-24	5.3826E-10
1.00E-11	3.1563E-07	3.0407E-24	5.2888E-10
1.00E-10	2.7025E-07	7.7867E-24	5.1592E-10
1.00E-09	3.9156E-07	1.9768E-23	5.0218E-10
1.00E-08	5.7930E-07	5.1258E-23	4.8533E-10
1.00E-07	9.6674E-07	1.3549E-22	4.6468E-10
1.00E-06	1.6972E-06	3.6112E-22	4.4042E-10
1.00E-05	3.1144E-06	9.7078E-22	4.1160E-10
1.00E-04	6.0006E-06	2.6035E-21	3.7835E-10
1.00E-03	1.2043E-05	6.8624E-21	3.4177E-10
1.00E-02	2.5056E-05	1.7267E-20	3.0706E-10
1.00E-01	5.3590E-05	3.9126E-20	2.9312E-10

1	1.1675E-04	6.7757E-20	3.8917E-10
10	2.5349E-04	9.3222E-20	6.6768E-10
20	3.1835E-04	1.4014E-19	3.7767E-10
30	3.6169E-04	1.4979E-19	3.7899E-10
40	4.0185E-04	1.5514E-19	3.7954E-10
50	4.3512E-04	1.5789E-19	3.7977E-10
60	4.6378E-04	1.5942E-19	3.7987E-10
70	4.8938E-04	1.6030E-19	3.7992E-10
80	5.1326E-04	1.6082E-19	3.7994E-10
90	5.3396E-04	1.6109E-19	3.7995E-10
100	5.5359E-04	1.6124E-19	3.7995E-10
300	7.9849E-04	1.6941E-19	3.7985E-10
500	9.4201E-04	2.1316E-19	2.7902E-10
800	1.1016E-03	2.4731E-19	8.4792E-10
1000	1.1864E-03	2.9929E-19	8.8132E-10

This correlation resulted in the following:

- Parameter A versus corrosion current had the following correlation:

$$A \sim I_p^{0.248} \qquad 3.13$$

Figure 3.18 displays the resulting curve fit for the corrosion current range against parameter A's values.

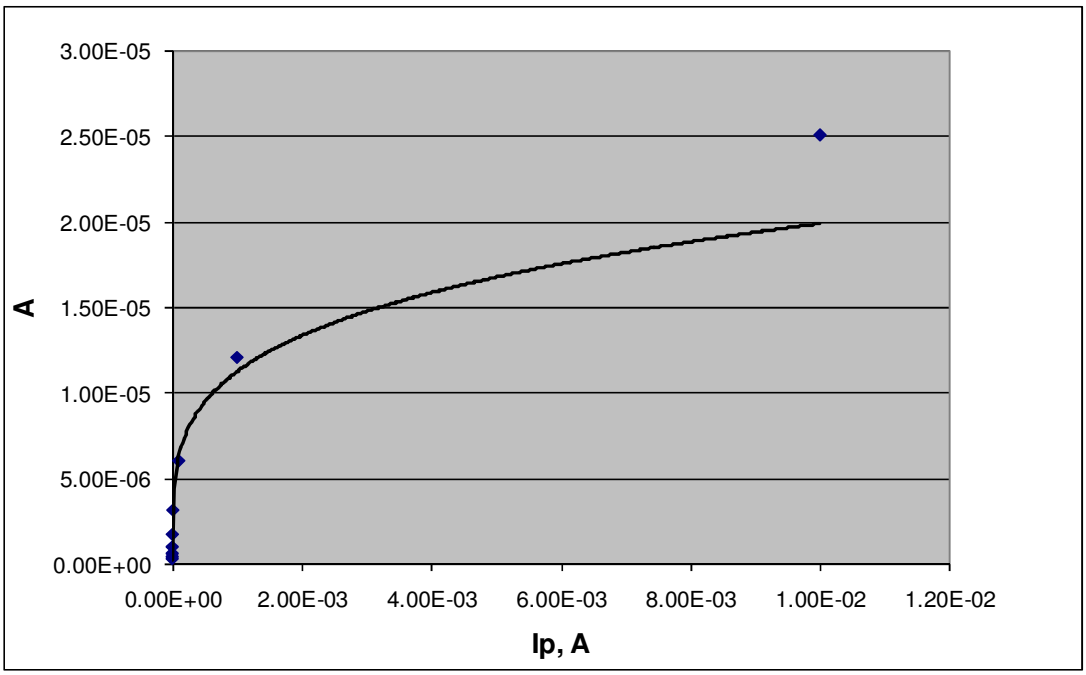

Figure 3.18. Plot of Corrosion Current Values vs Empirical Model Parameter A Values.

- Parameter B versus corrosion current had the following correlation:

$$B \sim I_p^{0.421} \qquad 3.14$$

Figure 3.19 displays the resulting curve fit for the corrosion current range against parameter B values.

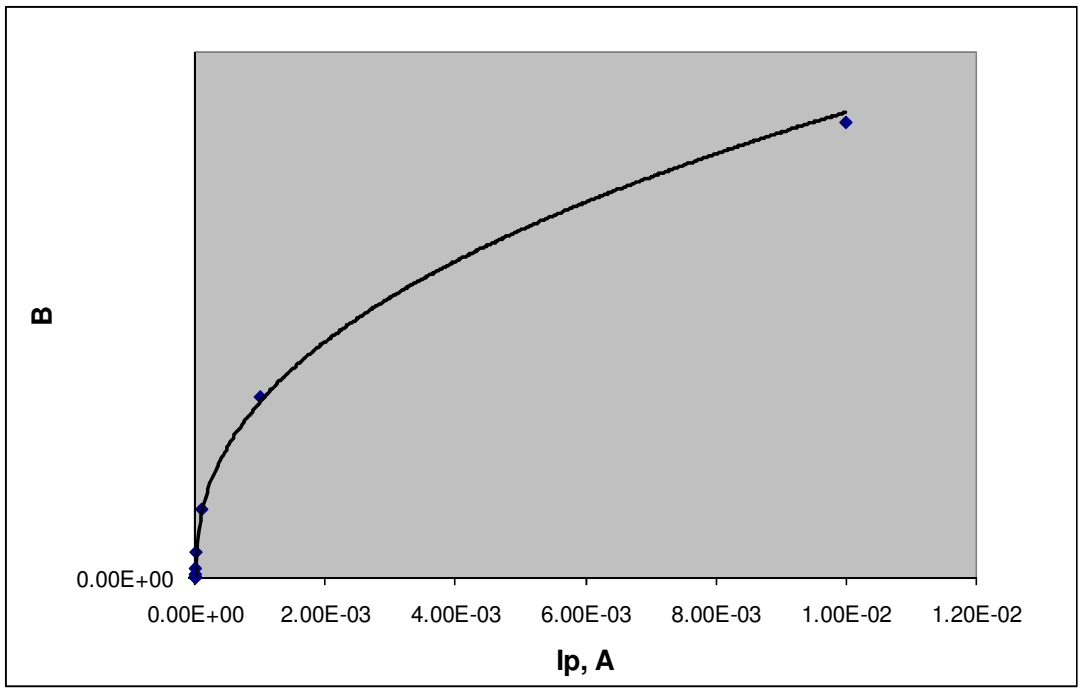

Figure 3.19. Plot of Corrosion Current Values vs. Empirical Model Parameter B Values.

- No correlation was found between corrosion current and the proposed empirical model parameter C.

Hence, with the above correlations for the corrosion current with the proposed empirical model's three parameters A, B, and C, the empirical model would be further updated as follows:

$$a = A \cdot \sigma^{0.182} \cdot \nu^{-0.288} \cdot I_p^{0.248} \cdot N^{1/3} + B \cdot \sigma^{3.24} \cdot \nu^{-0.377} \cdot I_p^{0.421} \cdot N^2 \cdot e^{4\times10^{-10} \cdot \sigma^{2.062} \cdot \nu^{0.024} \cdot N} \quad 3.15$$

3.5.3.4 **Updated Empirical Model Structure**

Equation 3.15 is the updated form for the proposed empirical model in Equation 3.4, in which the physical parameters affecting the operating pipeline have been addressed. To verify the updated form, the updated empirical model was examined against the superposition Wei's model as shown in Figure 3.20.

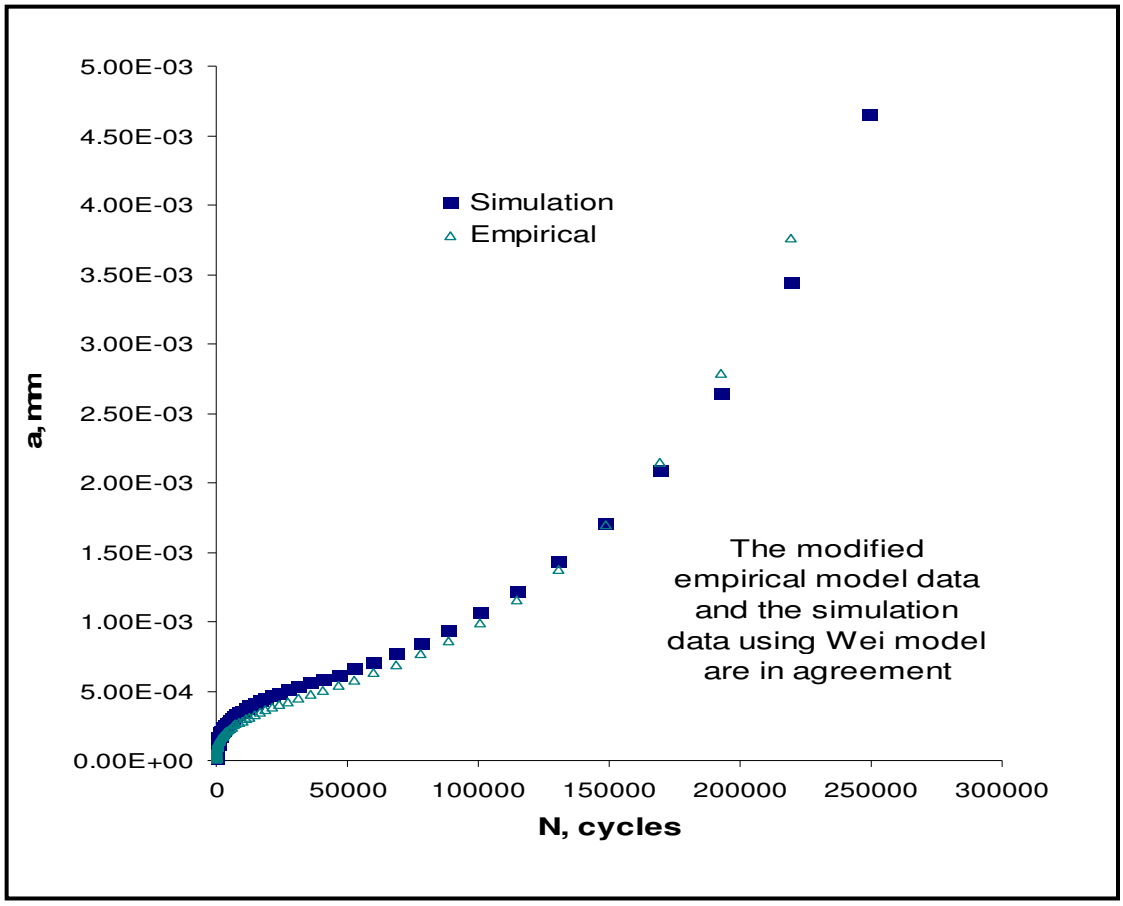

Figure 3.20. Plot of the Updated Empirical Model Outcome Against Wei's Superposition Model Outcome.

The close agreement between the outcomes of both the modified proposed empirical model and Wei's superposition is clearly shown in Figure 3.20. Thus, an important goal has been accomplished by proposing a simple empirical model, Equation 3.15, capable of reproducing Wei's superposition model with the least error factor, and at the same time addressing the physical aspects of the pipeline. All the inputs required in the superposition model have now shrunk to only a few, and most importantly the uncertain parameters have been reduced to two only. Now, working with a simple model having only two parameters, the probabilistic analysis will be more affordable.

3.5.3.5 **Estimation of Model Parameters Including Uncertainty**

The distribution of the proposed empirical model in Equation 3.15 could be estimated using three different sets of data:

1. Generic data produced using the MATLAB program that was applied to run the superposition Wei's model simulation.
2. Field data that would be gathered from selected refineries for pipelines having the material characteristics and operating within the same profile as intended in this research.
3. Experimental data that would require a lab set-up to run pitting corrosion tests and corrosion-fatigue crack growth tests.

Experimental data will be discussed in more detail in Chapter 4. Meanwhile, the generic data that could be produced from MATLAB for Wei's superposition model will be very

helpful in estimating the proposed empirical model parameters A and B. This estimation will also give a glimpse of the approximate characteristics of their respective distribution, which later can be a helpful guide when the field and experimental data are applied.

In order to obtain enough data to build the distribution for the empirical model's A and B parameters, the MATLAB program written to run the superposition model was extended to include a section that would calculate A and B values for each curve produced in the simulation (this can be set to any number of curves). To do so, the following mathematical approach was utilized:

Equation 3.15 was split into two parts,

$$f_i = \sigma^{0.182} \cdot \nu^{-0.288} \cdot I_p^{0.248} \cdot N^{1/3} \tag{3.16}$$

And,

$$g_i = \sigma^{3.24} \cdot \nu^{-0.377} \cdot I_p^{0.421} \cdot N^2 \cdot e^{4\times10^{-10}\cdot\sigma^{2.062}\cdot\nu^{0.024}\cdot N} \tag{3.17}$$

where Equation 3.15 could be represented using Equations 3.16 and 3.17 as follows:

$$a_i = A \cdot f_i + B \cdot g_i \tag{3.18}$$

where the first part of the summation represents the pitting corrosion degradation, and the second part represents the corrosion-fatigue crack growth degradation.

The error function is defined as follows:

$$Error = \sum_i^n [a_i - A \cdot f_i - B \cdot g_i]^2 \quad 3.19$$

Equation 3.19 is used to estimate A and B as follows:

$$\frac{\partial E}{\partial A} = 2[a_i - A \cdot f_i - B \cdot g_i] \cdot [-f_i] = 0 \quad (1)$$

$$\frac{\partial E}{\partial B} = 2[a_i - A \cdot f_i - B \cdot g_i] \cdot [-g_i] = 0 \quad (2)$$

From (1),

$$a_i f_i - A f_i^2 - B g_i f_i = 0 \quad (3)$$

From (2),

$$a_i g_i - B g_i^2 - A g_i f_i = 0 \quad (4)$$

From (3),

$$f_i^2 A + g_i f_i B = a_i f_i \quad 3.20$$

From (4),

$$f_i g_i A + g_i^2 B = a_i g_i \quad 3.21$$

So a matrix can be written based on Equations 3.20 and 3.21:

$$\begin{bmatrix} f_i^2 & g_i f_i \\ f_i g_i & g_i^2 \end{bmatrix} \begin{bmatrix} A \\ B \end{bmatrix} = \begin{bmatrix} a_i f_i \\ a_i g_i \end{bmatrix} \quad 3.22$$

The matrix in Equation 3.22 was applied to the MATLAB program, used to simulate the superposition model outcomes, to produce enough data points for A and B parameters.

The produced data points from MATLAB were later introduced to different program, ReliaSoft-Weibull ++ 5.32, which is capable of estimating A and B distributions. Figures 3.21 and 3.22 display an approximate distribution for A and B, respectively, for one operating condition.

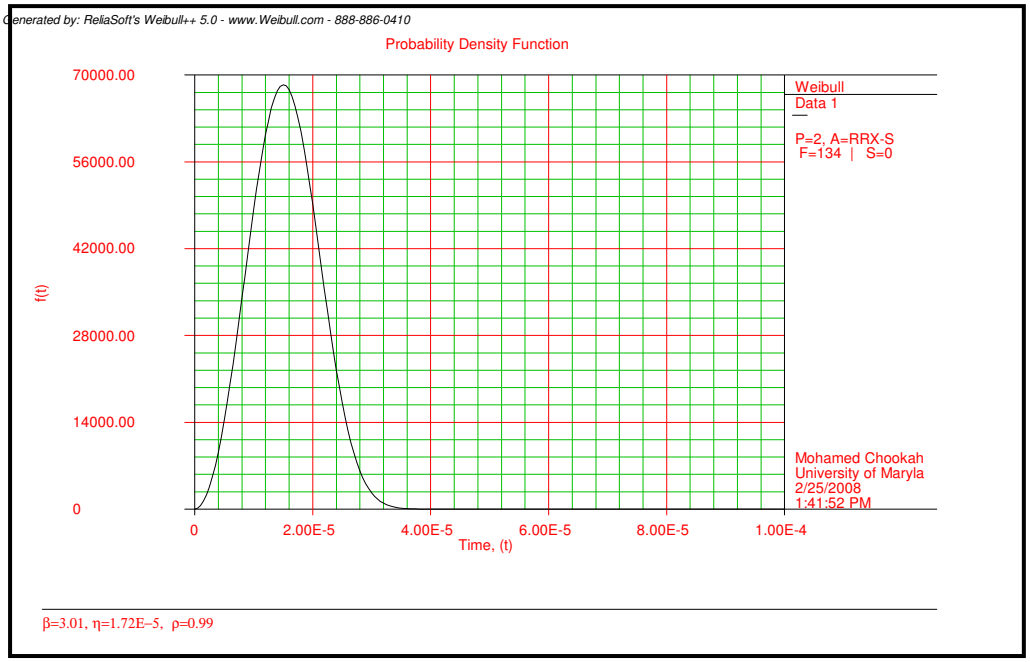

Figure 3.21. The Weibull Distribution of A with a Shape Parameter, β, of 3.01 and Scale Parameter, α, of 1.72×10^{-5}.

.

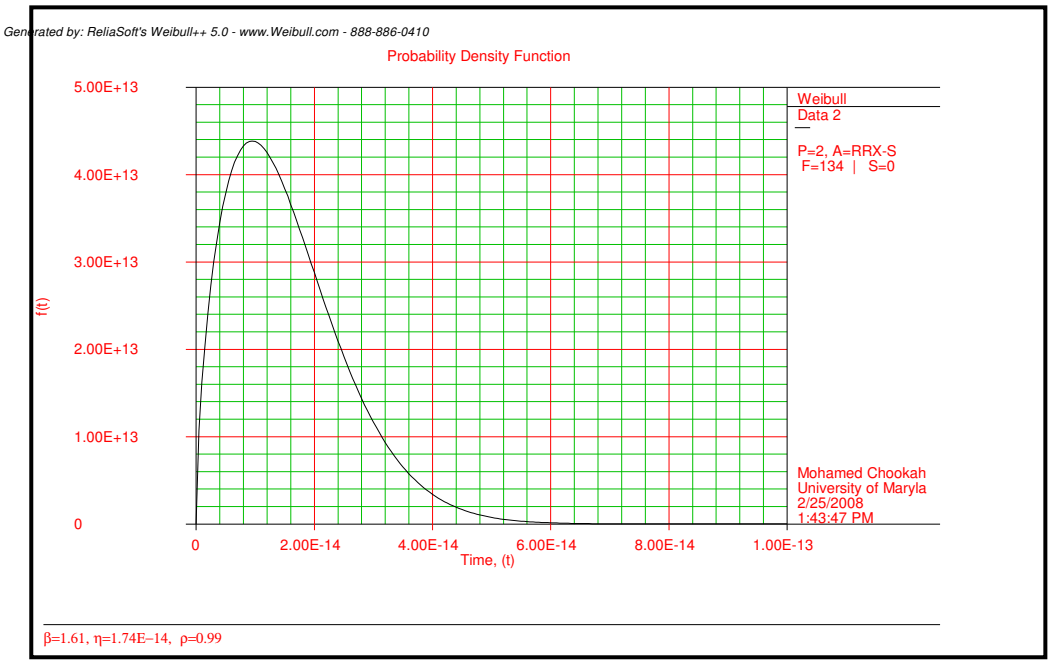

Figure 3.22. The Weibull Distribution of B with a Shape Parameter, β, of 1.61 and Scale Parameter, α, of 1.74×10^{-14}.

Further, the Monte Carlo simulation was run at a randomly selected conditions as displayed in Table 3.7 to examine the effect of the pipeline operating aspects on A and B distributions.

Table 3.7. Randomly Selected Environmental Conditions to Run the Monte Carlo Simulation to Obtain A & B Distributions.

Data set	T, K	σ, MPa	ν, Hz	Ip, A
1	373	10	10	1×10^{-5}
2	673	20	7	1×10^{-6}
3	473	30	5	1×10^{-5}
4	273	40	4	1×10^{-6}
5	573	50	3	1×10^{-5}

Utilizing again the ReliaSoft-Weibull ++ 5.32 program to analyze the distribution of each parameter respectively, it was possible to obtain the following.

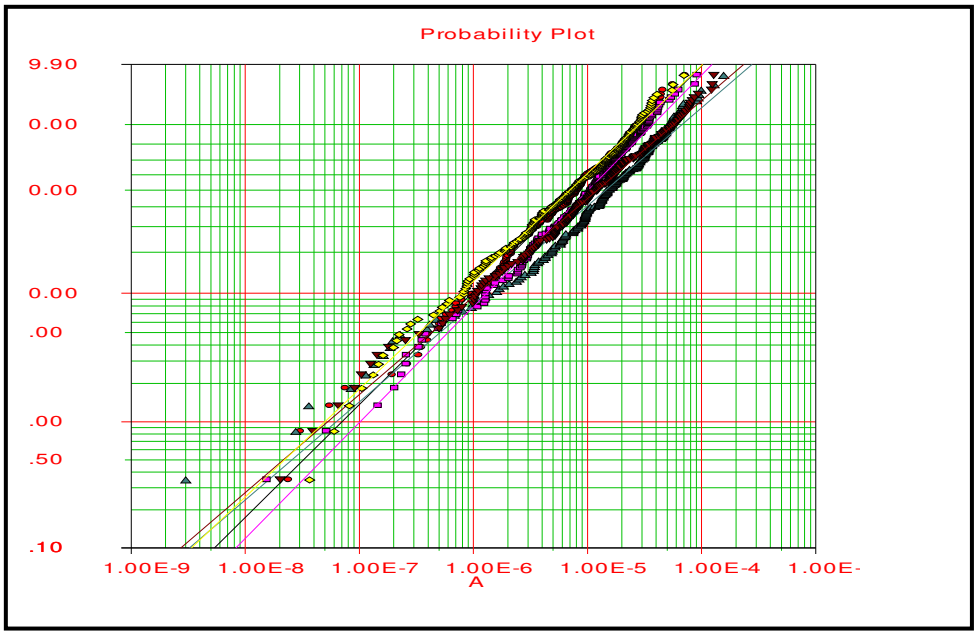

Figure 3.23. The CDF (Weibull) of Parameter A Distribution for Five Different Data Sets as in Table 3.7.

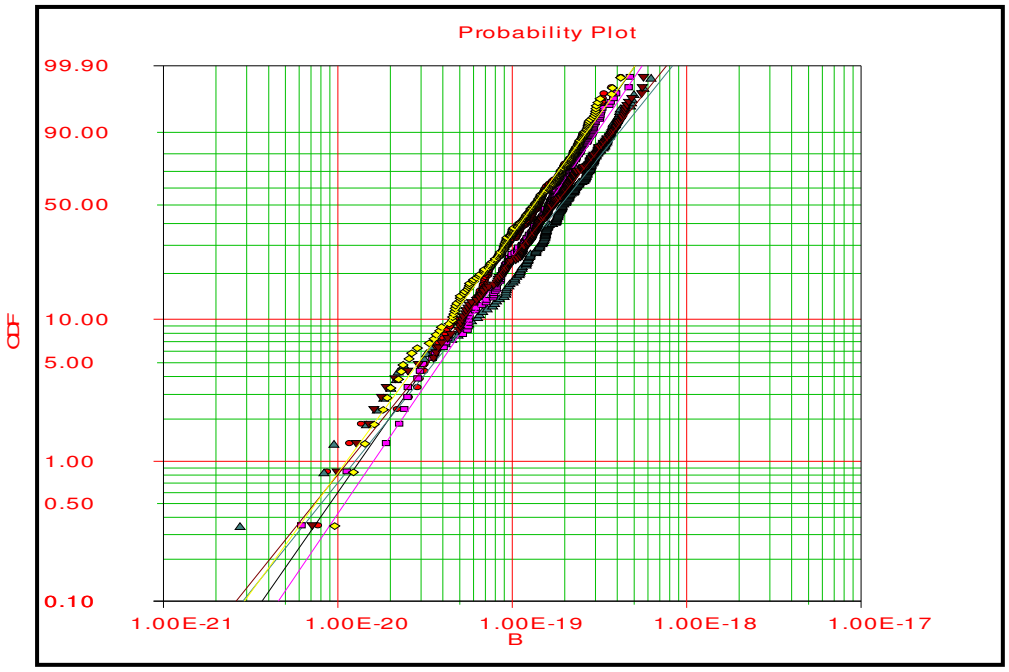

Figure 3.24. The CDF (Weibull) of Parameter B Distribution for Five Different Data Sets as in Table 3.7.

The most notable aspect of Figures 3.23 and 3.24 is the negligible impact of environmental condition variations on the A and B distributions. This evidence implies the independency of the A and B variabilities from the pipeline's surrounding environmental conditions; thus, the source of the variability is mainly from the material property.

3.6 *Summary*

A simple empirical model has been proposed that was capable of capturing the two major degradation mechanisms of pitting corrosion and corrosion-fatigue. The simulation outcomes generated in MATLAB facilitated the identification of the simple form that resembles the benchmark model outcomes with the least number of uncertain parameters which was only two. To proposed empirical model has two uncertain parameters that correlates crack size with independent variables of stress (load) applied, frequency of the load, and the environmental conditions such as the concentrations of the chemical agents. Temperature has been correlated with the corrosion current parameter which was experimentally proved. An initial attempt to estimate the proposed model two uncertain parameters has revealed a satisfactory agreement with the anticipated results.

CHAPTER 4

DATA COLLECTION

4.1 *Introduction*

Generating data for corrosion-fatigue as well as for pitting corrosion degradation mechanisms is an essential element of the modeling process. The proposed empirical model in Chapter 3 had relied on the generic data that was used in the Monte Carlo simulation based on Wei's superposition model. To claim further validity of the proposed empirical model that could be applied practically to the pipelines undergoing pitting corrosion and corrosion-fatigue degradation, actual and controlled data is required. The filed data would be the best source for such data. However, the data collected from a refinery having pipelines undergoing similar degradation mechanisms revealed many weaknesses such as inconsistency, crack growth records unavailability, and unconfirmed failure mechanisms. Hence, it is necessary to rely on experimental data which would yield more consistent and controlled information. Given the proposed Bayesian analysis that will be used to evaluate the data, even small amount of data acquired from the experiments discussed in this chapter would be sufficient to practically estimate the proposed empirical model parameters.

This chapter details the data collection from two sources. An outside testing lab in New York State was hired to carry out some of the indented pitting corrosion and corrosion-

fatigue tests. On the other hand, a few pitting corrosion tests were conducted in-house, in addition to one corrosion-fatigue test utilizing the recently acquired Cortest testing equipment. Hence, this chapter will be divided into two sections, each dedicated to one source of data collection. These two sections discuss the approach and corresponding results from the outside lab in New York and the in-house experiments.

4.1.1 **Innovative Test Solution Lab**

Innovative Test Solutions (ITS) of Scotia, New York conducted crack-growth testing at temperature, as well as corrosion testing at temperature on compact tension (CT) specimens machined from X-70 pipe material. Electric Potential Drop software was utilized to record the crack propagation during the crack-growth tests. Separate specimens were statically stressed and introduced to a corrosive salt solution for a period of time, where surface corrosion was recorded in the form of pitting size and depth. Both tests used a corrosive salt solution for the testing medium.

4.1.1.1 **Crack Growth Procedure**

Compact tension (CT) specimens were machined from X-70 pipe material for the purpose of crack-growth testing. The basic geometry for the CT specimens was dictated by ASTM E-1457, along with the test procedure for crack growth with EPD. Prior to testing, the specimens were pre-cracked using a cyclic tensile load in air at room temperature. The load applied to the specimen during pre-cracking was a magnitude smaller than the loads applied during the test.

After a pre-crack was formed, specimen dimensions were then measured and recorded. Next, three sets of wires were attached to the CT specimen for the purpose of using Electric Potential Drop software to track the crack propagation during the test. One set was used for inducing a current into the specimen, the second set was used to read the active voltage drop across the specimen crack plane, and the third was a reference of the voltage drop outside of the crack plane. An illustration of a standard CT specimen and locations for wire attachment is provided in Figure 4.1.

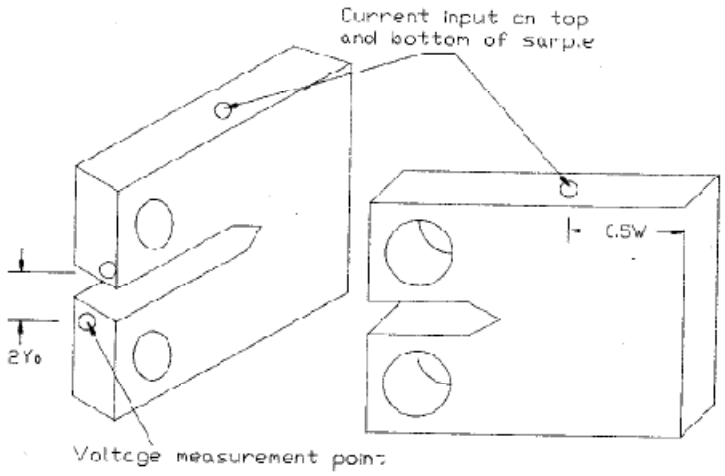

Figure 4.1. Geometry of Typical CT Specimen and Lead Wire Placement.

The prepared specimen was installed in a loose load train that was shielded from ground, and was placed into a watertight container that would hold the corrosive salt solution medium during the test. A cartridge heater was installed into the test medium to regulate the temperature to 90º (194ºF). A diastolic pump was utilized to circulate the medium and any particulates caused by corrosion. The load train was then installed into an MTS-

system 20 Kip servo-hydraulic frame with digital recording capabilities of stroke, force, reference and active voltage input channels. All channels were recorded during the test for crack propagation determination. The voltage signals were amplified between the specimen and recording device to better show minute changes in the voltage drop across the crack plane. The current induced upon the specimen was switched every 5 seconds during the test.

A diagram and picture of the set-up is shown in Figure 4.2 and Figure 4.3.

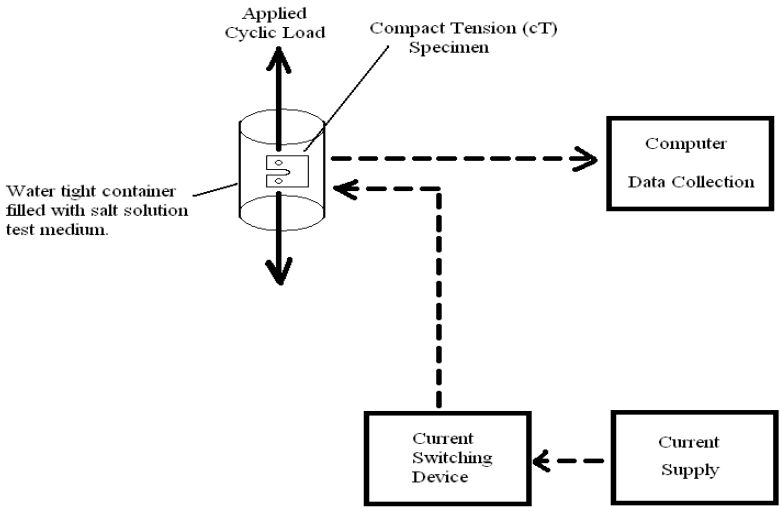

Figure 4.2. Crack Growth Test Set-up.

Upon the test termination, specimens were removed, and measurements of the crack plane were taken using a high-magnification scope. The pre-crack and final crack lengths were used to determine the crack propagation rate during the test.

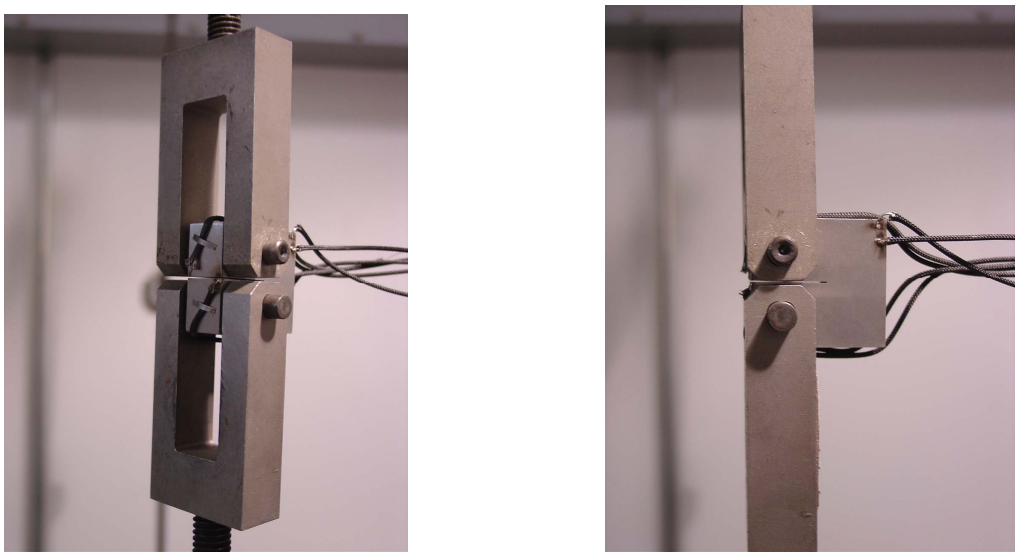

Figure 4.3. Crack Growth CT Specimen with Lead wires attached and installed into a loose load train prior to submersion into test medium.

The testing medium was a corrosive salt solution comprised of substitute seawater and 0.4% by volume sodium thiosulfate. The two medium components are shown in Figure 4.4. The substitute seawater was made to ASTM-D1141 standards. The corrosive salt solution was utilized for both the crack-growth testing and static-stress corrosive testing.

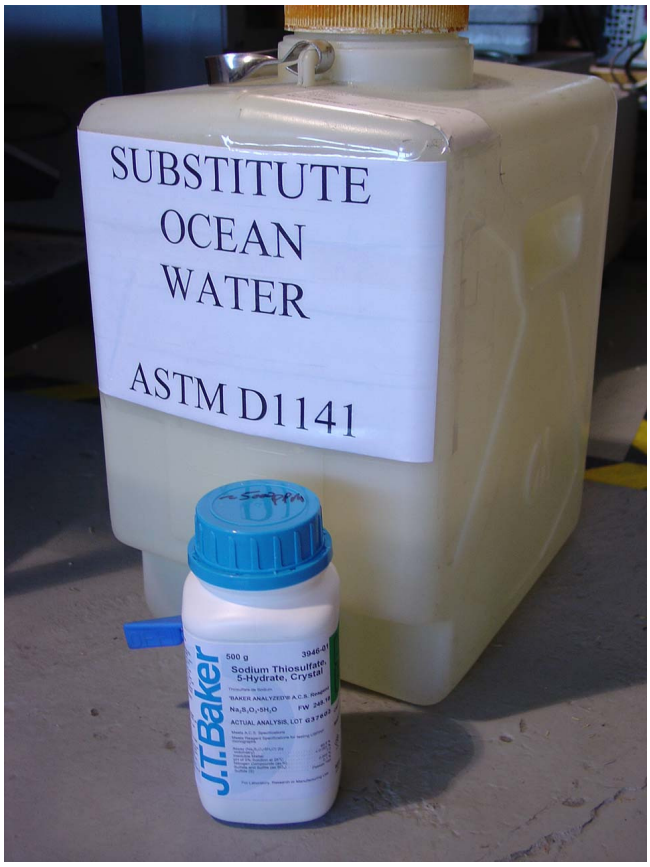

Figure 4.4. Substitute Seawater and Sodium Thiosulfate Comprise the Testing Medium.

The corrosion current value of the X-70 material in the corrosive salt solution medium was recorded using a potentiostat to record the minute current created by the corrosion chemical reaction.

4.1.1.2 Corrosion Test Procedure

Static-stress corrosion specimens were machined from X-70 pipe material. The specimens were approximately 2" long by 1" wide strips, 1/8" thick. A strain gage was applied to the center of the specimen in order to read the stress applied. The specimen

was fitted into a device that secured the ends of the specimen and statically stressed the specimen by applying a force to the side opposite the strain gage by a threaded bolt with a ¼" ball bearing as the point of pressure. Locking nuts ensured that the stress applied remained static. A picture of a static stress specimen with a strain gage applied to the surface is shown in Figure 4.5 below.

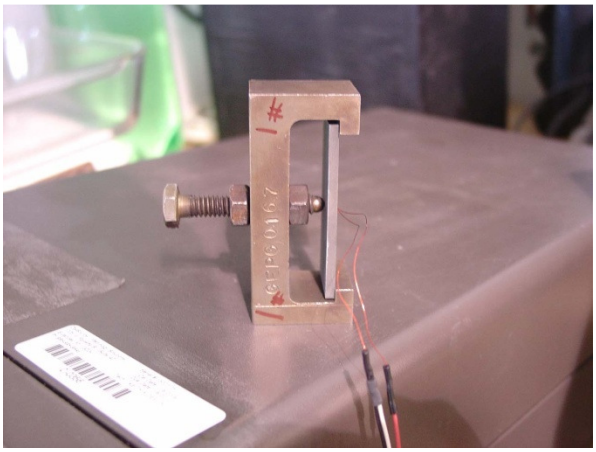

Figure 4.5. Static Stress Corrosion Specimen with a Strain Gage Applied to One Face for Measurement of Stress Applied.

The specimens were submerged in a bath of the corrosive salt solution medium, which was heated to 90ºC (194ºF). Periodically the specimens were removed from the medium, and pit size and depth were measured using a profilometer. Pictures of the surface were also taken to record the corrosion process. A picture of the static-stress corrosion test set-up is shown in Figure 4.6.

Figure 4.6. Static-Stress Corrosion Test Set-up.

Pictures of the surface corrosion and a graph of pit size vs. time are available in Appendix A.

4.1.1.3 **Results Discussion**

The crack growth specimens were tested at various stresses, and test frequencies. All testing was conducted at an "R" Ratio of 0.5. The loose load train prohibits the specimen from being fully unloaded. The R ration of 0.5 ensured that the specimen was in tension at all times during the test. The crack growth measurements were obtained at or near full tension, when the specimen crack faces were farthest apart, to ensure no voltage leakage

across the crack plane. The resultant data was tabulated and plots made to graphically represent the crack propagation during test. These results are displayed in Appendix B. All specimens experienced severe corrosion during submersion in the corrosive salt solution testing medium. Due to the corrosion final measurements of the crack plane faces were under a best effort basis. Multiple measurements of the pre-crack length, and crack length were made to ensure accurate results.

The static stress specimens were removed from the corrosive salt solution medium and surface profile measurements were taken during the 40 day test. Scaling of the material was noted on the surface of the specimen around the 3 week mark. Pit size was determined using the profile data from multiple passes over the specimen surface. The Static Stress specimens also experienced severe corrosion.

4.1.2 **In-House Testing**

The main objective of conducting in-house tests was to establish a state-of-the-art laboratory capable of carrying out mainly corrosion-fatigue tests plus many more related tests in the field of study. Also, it became apparent that outsourcing for corrosion-fatigue tests is quite an expensive option with enormous compromise on the number of tests runs and the quality of data collected. Hence, the decision was made to establish a corrosion-fatigue laboratory to serve this research field for many years to come. The sponsor of this research, ADNOC (Abu Dhabi National Oil Company, UAE), generously provided sufficient funds to establish the intended laboratory. Thus, the state-of-art corrosion-

fatigue equipment was acquired from Cortest company in Ohio, USA, which can achieve the most accurate corrosion-fatigue tests resembling the actual field settings.

In addition to the above corrosion-fatigue tests, in-house pitting corrosion tests were conducted utilizing the available resources within the university.

4.1.2.1 **Corrosion-Fatigue Testing**

As mentioned above, the in-house corrosion-fatigue test was conducted, and the resulting data was collected for further analysis. The subsequent sections detail this conducted corrosion-fatigue test.

4.1.2.1.1 ***Cortest Testing Equipment***

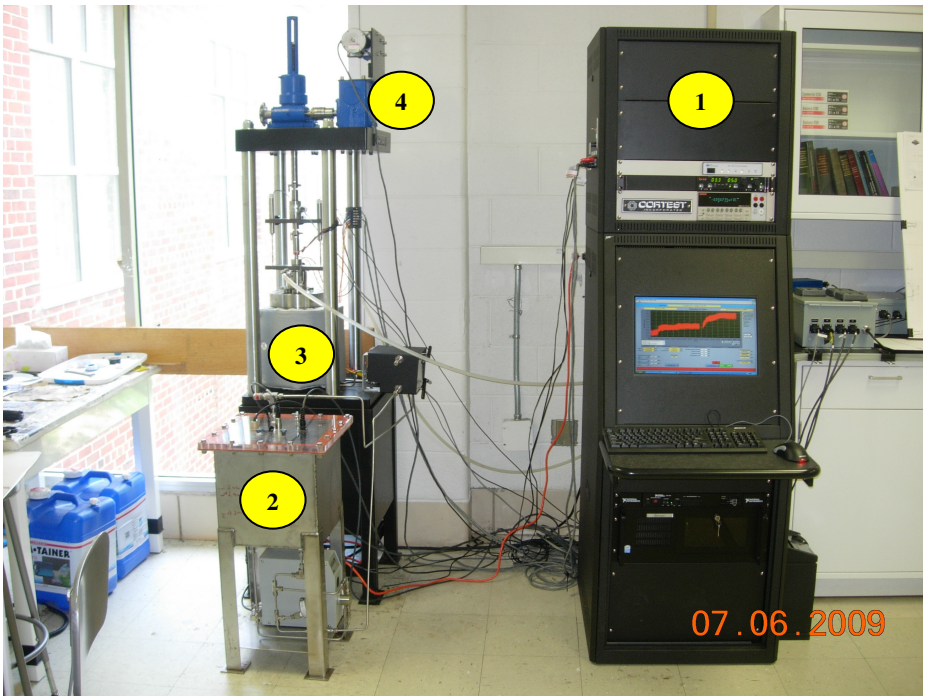

Figure 4.7. The Cortest Corrosion-Fatigue Test Equipment.

From Figure 4.7:

1. Data acquisition tower and the PC monitoring system.
2. Recirculating fluid tank (RTL)
3. Vessel assembly (Autoclave)
4. Motor assembly

It should be mentioned here that this equipment is specified for working under very low extension rates of up to 4.5 x 10^{-5} mm, and so it is possible to perform tests with very high accuracy and nearly exact acceleration to the problems that might happen in the real field.

The test results from the specimen were evaluated according to the Johnson equation with help from the direct current potential drop (DCPD) method.

4.1.2.1.2 ***DCPD Method***

The direct current potential drop (DCPD) [126] method represents a way to measure crack length indirectly during experimental fatigue crack growth investigations or short-term fracture mechanics testing, such as the measurements of fracture toughness and the J-integral. The DCPD method works on the basis of an occurrence of a potential drop caused by a discontinuity in a specimen, such as cracks, when a homogeneous direct current of sufficient value passes through the whole cross-section of a sample.

A big advantage of the DCPD method is the possibility of an analytical expression of the potential drop for various configurations of electrodes and different shapes and dimensions of a specimen. Johnson's formula [127] and its modification [128] are two of the most frequently used analytical descriptions of the dependence and calculation of crack length on the potentials in specimens of a rectangular cross-section with a through-thickness crack of straight-crack front. The DCPD measurement is one of the most reliable and convenient methods of automatically monitoring the crack growth process, suitable for integration into computer controlled monitoring systems, with no need for direct, time-consuming optical measurements. The crack length was evaluated using the well-known Johnson's formula:

$$\frac{a}{W} = \frac{2}{\pi} cos^{-1} \left\{ \frac{cosh\frac{\pi Y_O}{2W}}{cosh\left[\frac{V}{V_O} cosh^{-1}\left[\frac{cosh\frac{\pi Y_O}{2W}}{cosh\frac{\pi a_O}{2W}}\right]\right]} \right\} \qquad 4.1$$

a_0 being the initial crack length, V_o=V(a_o) the corresponding initial potential, W the effective width of the specimen, and y the distance of electrodes from crack mouth. The following figure shows the DCPD schematic connected to a CT specimen.

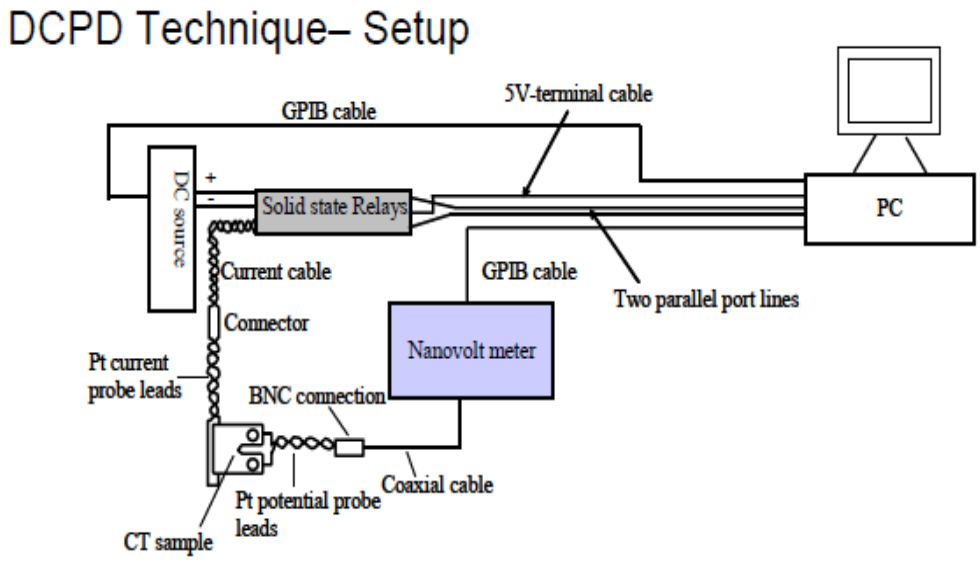

Figure 4.8. DCPD Connection to CT Specimen [129].

For the entire exact evaluation of the result in this connection, we need

• A high-stability DC source and nano-volt meter to ensure better resolution and accuracy.

• Pt probes to improve the data reliability.

• A solid-state relay to reverse the current.

• Coaxial cables and BNC connections to reduce the electric noise.

• Software to control the measurement process.

All of these requirements were provided with the CORTEST equipment with the exception of Pt-wires and appropriate coaxial cables and BNC connections to reduce noise.

The placement of probes on the specimen is given below. The placement of the probe leads was optimized to obtain the best accuracy and reproducibility of the DCPD measurement.

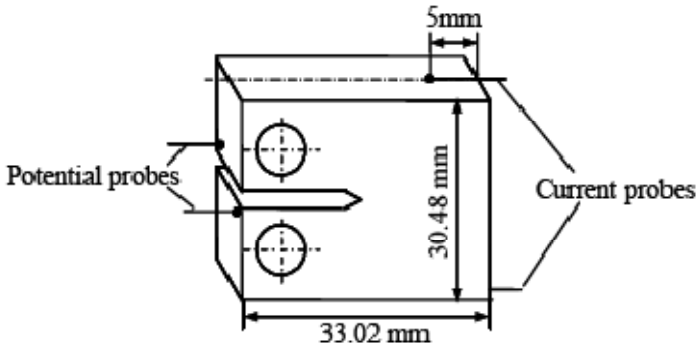

Figure 4.9. CT Specimen with the Placement of Wire Connections for Best Results.

The dimensions given in the diagram are not the dimensions of our specimen.

4.1.2.1.3 ***Test Procedure***

4.1.2.1.3.1 CT-specimen preparation

Duplicate crack propagation tests were performed using CT specimens machined from the base piping X70 steel material. Material composition and mechanical properties for the steel are given in Tables 2.9 and 2.10 in Chapter 2.

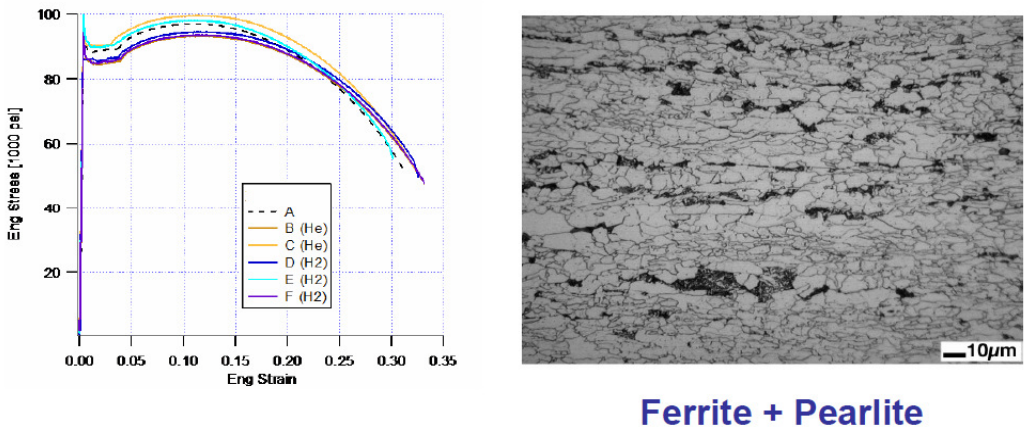

Figure 4.10. Stress-Strain Curve of X70 Carbon Steel in Different Environments with its Metallographic Ferrite-Perlite Microstructure [130].

The tests were performed with pre-cracked compact type (CT) specimens loaded under cyclic load conditions. Testing was performed with R ratio (ratio of minimum to maximum load) of 0 and a frequency of the Hertz found in Ocean City, Maryland seawater (with 7.2 gr. chloride per liter) plus 250 ppm $Na_2S_2O_3$, substitute for H_2S since the lab is not equipped for using the actual harmful H_2S, electrolytes at 110 ^{0}C. The applied load in the tests was 100 MPa=1317 Kgf, which corresponds to a maximum stress intensity factor of 62.436 MPa$\sqrt{m}$. This K value is typical of a large sub-critical flaw in an operating gas pipeline [131]. Crack growth was monitored using an electric potential drop (EPD) technique. With this crack growth monitoring technique, a DC current was passed through the specimen, and crack extension was assessed by measuring the change in potential drop across the crack. The testing was performed in an air- and liquid-tight auto-clave cell. The test specimen was electrically isolated from the loading clevises and cell hardware. To prevent the crack propagation in undesirable directions, two grooves were made along the specimen parallel to the notch direction.

A DC current of 5 amperes was used for the crack growth measurements. The current was continuously applied during the test, and the polarity was not reversed. A data acquisition unit recorded time, load, load line displacement, and potential drop of the specimen every 1.5 minutes during the test. The data were analyzed using a proprietary program, according to the Cortest software. The program calculates crack length from the EPD data using the Johnson Equation (ASTM Standard E 647-88a [132]).

Input data for the computer programs for each test included machined notch length, fatigue pre-crack length, specimen width (W), thickness (B), net thickness (BN), load, load line displacement, and EPD.

After ending the test, the specimens were metallographically mounted, polished, and examined.

4.1.2.1.3.2 Dimensions of X70 -1/2 – CT specimen

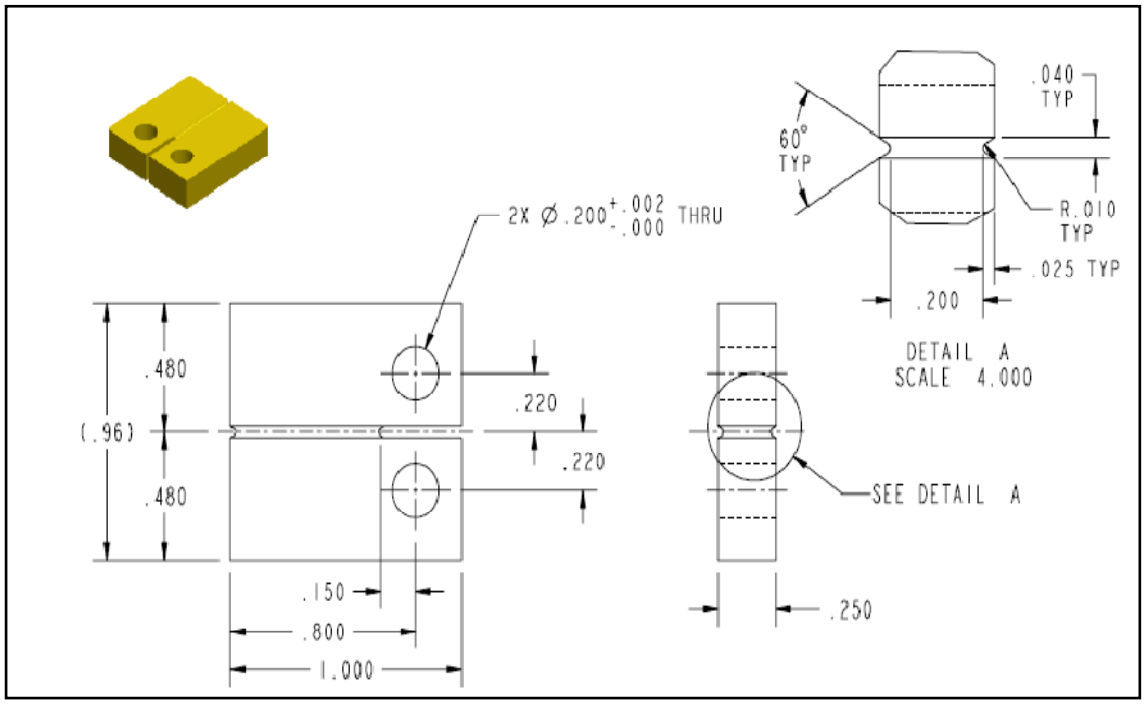

Figure 4.11. ½ CT Specimen Prepared by the Metal Company.

The ½ CT specimen was prepared with the following dimensions:

Specimen length = 24.384 mm ,

Specimen width = 20.32 mm ,

Initial crack length = 5.5626 mm ,

Specimen depth = 6.35 mm ,

Half voltage lead-spacing = 4.064 mm

4.1.2.1.3.3 Pre-cracking of the specimens

Two specimens were pre-cracked by Metcut Research Inc. of Ohio, performed in K-control using the DC electric potential drop method of crack measurement following ASTM E-647 requirements. The pre-crack summary is given in the following table.

Table 4.1. Pre-Crack Summary.

specimen	Test #	Ki_{max}/Pi_{max}	a_0 (inches)	Kf_{max}/Pf_{max}	a_f (inches)	Cycles
A	**1-265**	**20/1000**	**0.144**	**15/572**	**0.219**	**101,821**
B	**2-265**	**20/1004**	**0.142**	**15/573**	**0.219**	**101,012**

K_{max} is given in (ksi)x(inch)$^{0.5}$ and P_{max} is given in (lbf).

4.1.2.1.3.4 The Connection of the Leads to the specimen

The leads to the specimens were connected by screwing threaded ends into the specimen. Pt.-wires are the best material for current and voltage connection to the specimen because of their good resistance in corrosive environments. In the figure below, I= 5mm from the edge is the Pt-connection for the 5A current, and 2y is the (screwed) distance for the ~ 20V voltage applied.

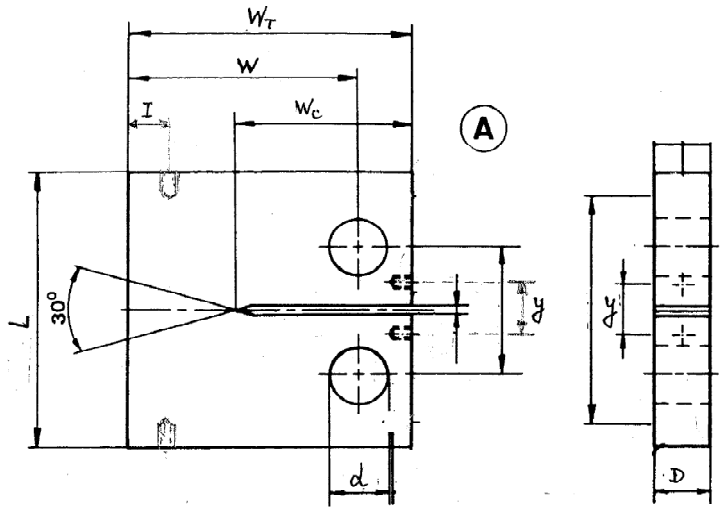

Figure 4.12. Screwed Places on the Specimen for Applying Current(I) and Voltage(y).

4.1.2.1.3.5 CT – Specimen Loading

The pre-cracked CT specimen was installed between the grips and fixed into them by two ceramic-coated pins. Ceramic coatings (0.005 mm) were made to prevent the specimen contacting the grips and lowering the noises that could come from the current applied to the specimen. The specimen holder in the autoclave with their Pt-connections is shown in the following figure. After fixing the specimen in the holder, the Pt-connection was fixed on the specimen. The connection leads on the outside of the autoclave would be ready for further current and voltage supply. The autoclave with the installed specimen in it was filled with a fixed amount of corrosive liquid, closed, and separated from the outside.

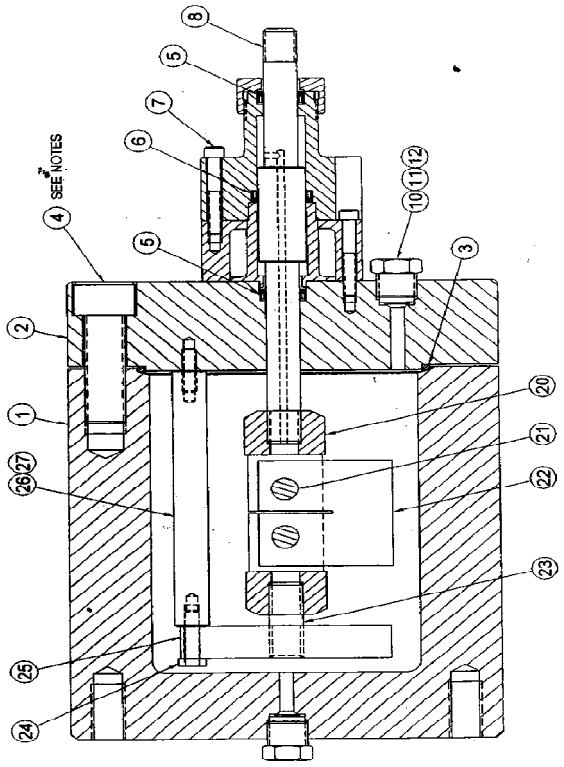

Figure 4.13. Auto-Clave with the Specimen Holder.

4.1.2.1.3.6 Procedure for Corrosion-Fatigue test

The step-by-step procedure for the corrosion-fatigue test from the beginning to the end—i.e., up to the breaking of the specimen—is given in the Cortest Operating Manual [133].

4.1.2.1.4 *Results*

Evaluations of the data occurred according to the Johnson equation, and plots of the data are shown in Appendix C.

4.1.2.2 **Pitting-Corrosion Test**

4.1.2.2.1 *Preparation of Carbon Steel X70 Specimen for Corrosion Experiment*

The X70 carbon steel specimen was cut from a pipe that is normally used in refinery pipelines. The sample dimension had a 5 cm length, 1.98 cm width and 0.2 cm thickness. The sample was polished at different stages with the polishing machine in the material science department laboratory with different sand papers according to the following time steps:

1. One hour with the 200-mesh sand paper;
2. Three hours with 400-mesh sand paper;
3. Three hours with 600-mesh sand paper;
4. One hour with 1000-mesh sand paper;
5. One hour with 1500-mesh sand paper.

After each step, the sample was observed under the optical microscope; at the end of the polishing process (polishing with 1500-mesh sand paper), pictures were taken at different magnifications under the same optical microscope (located in CALCE laboratory, under Mr. Ahmed Amin's supervision).

The optical microscope specification is an inverted metallurgical microscope (ZEISS-Axiovert- 135 model) equipped with an X-Y micrometer stage for scanning specimen, connected to a computer which, in turn, is equipped with a digital camera and AMSCOPE-3.0 image processor.

The software captures pictures with different pixels. The X70 carbon steel has a complex ferritic perlite micro-structure, which is shown in Appendix D.

The specimens, shown in Appendix D, were shiny enough, without pits, and ready for further corrosion tests. The next steps were:

1. Fixing the specimens in a holder (designed by us),
2. Immersing them in a corrosive environment (seawater) at 90-100 degrees Centigrade for at least five hours.
3. Observing them under a microscope to see the surface for further research.
4. In the case that the surfaces were free from pits, the test would be repeated until pitting occurred.
5. Then, the pit length, pit depth and pit densities was measured under the microscope.

4.1.2.2.2 ***Apparatus***

A bent-beam specimen holder was designed for determining the corrosion behavior of the X70 carbon steel specimens under stress in a variety of environments such as seawater, and other electrolytes containing chloride or H_2S. Because it is dangerous to work with hydrogen sulfide in the laboratory experiments, we chose to work with natrium-thiosulfide, which can be substituted for H_2S.

The specimen holder had a four-point loaded configuration [134] and is shown schematically in the figure below.

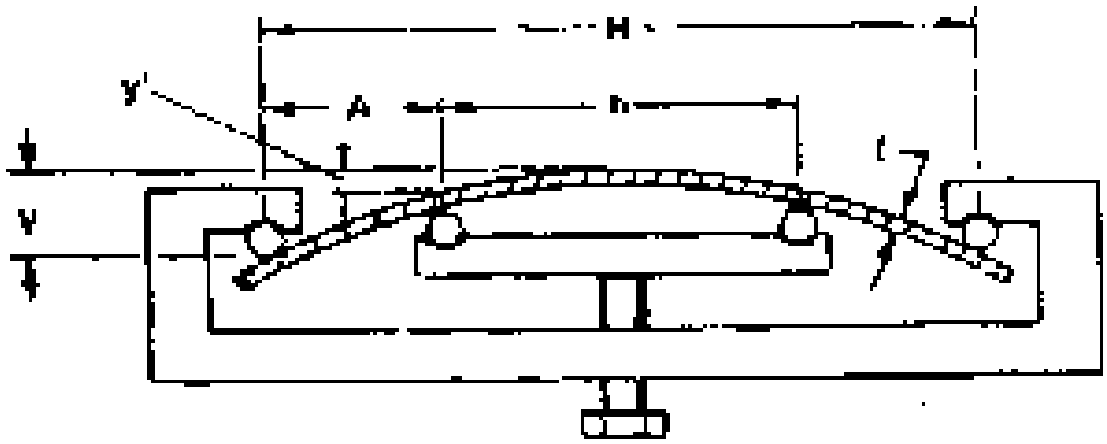

Figure 4.14. Four-Point Loaded Specimen [129].

The holder was made of steel material that could withstand the influence of the environment without deterioration or change in shape. When the stress-corrosion test was conducted by immersion in an electrolyte, galvanic action between specimen and holder had to be prevented [134]. There are different ways to do this:

1. Make the holder of the same material as the individual specimens.
2. Insert electrically insulating materials between the specimen and holder at all points of contact (many plastics can be used, especially in short-term tests).
3. Make the entire holder out of a nonmetallic material.
4. Coat the holder with an electrically non-conducting coating that effectively prevents contact between holder and electrolyte.

We chose the first and second way and covered the entire holder with a plastic tape and inserted plastic sheets between the specimen and covered holder parts.

4.1.2.2.3 *Stress Calculation*

All the stresses applied on the specimen had to be below the elastic limit of the material, i.e., below the engineering yield strength (0.2% offset). The yield strength of X70 carbon steel is 485 MPa. The equations applied according to the ASTM standard [134], are applicable only under the yield strength of the material. The applied stress was determined by specimen dimensions and the amount of bending deflection.

The four-point loaded specimen is a flat strip typically 20 mm wide and in our case was 50 mm long with a thickness of 2 mm. We supported the specimen at the ends and bent the specimen by forcing two inner supports against it in a fashion shown in the figure above. The two inner supports were located symmetrically around the midpoint between the outer supports.

The elastic stress for the mid-portion of the specimen (between contact points and the inner support) can be calculated according to the following equation:

$$\sigma = \frac{12 * E * t' * y}{(3H^2 - 4A^2)} \qquad 4.2$$

where σ = maximum tensile stress, E = modulus of elasticity, t' = thickness of the specimen, y = maximum deflection (between outer supports), H = distance between

outer supports, and A = distance between outer and inner supports. The dimensions are often chosen so that $A = H/4$. An alternative method of calculation for the elastic stress between the inner supports can be given by the equation [129]:

$$\sigma = \frac{4*E*t*y'}{h'^2} \quad 4.3$$

where h' = distance between inner supports, and y' = deflection between inner supports. This equation is a special case of the first one when $A = 0$.

By substituting the values from our holder and the estimation of the amount of bending or curvature of the specimen in the holder together with the Young's modulus of the specimen in the above equations, we get an approximate value of 620 MPa for the applied stress on the specimen during the corrosion-fatigue testing. The values for the parameters are given below,

E= 2.07GPa

t = 2.5cm, y = 0.005cm, H = 4.25cm,A=1cm $\Rightarrow$ σ =618.68 MPa

h=3cm, y'=0.0027cm. $\Rightarrow$ σ =621 MPa

4.1.2.2.4 *Experimental set-up for Pitting Corrosion*

Two specimens of API-5L X70 carbon steel with the dimensions given above were immersed in a seawater solution (with 500ppm H_2S=$Na_2S_2O_3$+5H_2O) in a set up given

below. One of the specimens was under stress in a grip according to the procedure given in ASTM, and the other, without applied stress, hung free in the solution. The experimental set-up is shown in the figure below,

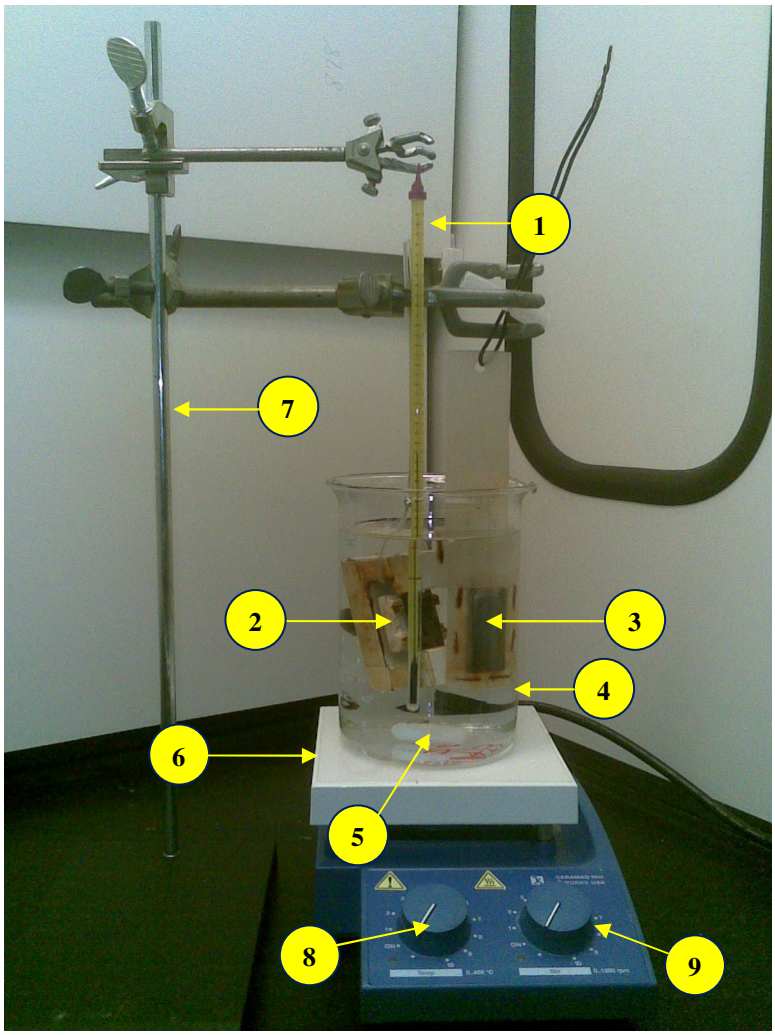

.

Figure 4.15. Experimental Set-up for Pitting Corrosion.

From Figure 4.15:

1. Thermometer
2. Specimen under stress in the gripe [93]
3. Specimen free (unstressed) in the corrosive liquid environment [135]
4. Beaker
5. Stirrer
6. Hot plate
7. Stand with grips for holding the thermometer and specimens
8. Nob for temperature regulation
9. Nob for regulation of movement of stirrer

The applied stress to the specimen was measured by measuring the amount of the curved deflection compared to the original form under the microscope. The holder form and the measuring process are given above.

4.1.2.2.5 ***Corrosion Experiment***

According to the measuring dimensions of the deflections in the metallurgical microscope a maximum tensile stress of 7 MPa was applied to the fixed specimen in the holder, and the specimen with the holder was immersed in the seawater in a beaker at a temperature of 80 ^{0}C for 3 hours. The liquid in the beaker was stirred with a magnetic stirrer and the temperature was estimated with a laboratory thermometer. After 3 hours the specimen was removed from the holder and examined by the metallurgical microscope. The pictures of the pitted specimens after the test are given in Appendix D.

The electron microscopic pictures from the specimen are given in Appendix D. These pictures show the pit morphology at much higher magnifications. As it is visible, the pits have a nearly hemispherical shape with a small degeneration at one side. It looks as if some inclusions dissolved play a critical role for stable pitting corrosion. In some literature it is suggested that the dissolved MnS inclusions in a chloride environment and at 90 ^{0}C are responsible for such a deformation of the hemispherical morphology [136].

It should be mentioned here that the composition of the bottom of the pit is given by an EDX – estimation in the SEM electron-microscope. In Figure H, shown in Appendix D, we counted nearly 14 pits in an area of 250×250 μm^2 (0.0625 mm^2) on the specimen.

4.1.2.2.6 *Pit Depth Measurement*

Pit depth can be determined by vertically sectioning through pre-selected microscopic visible pits by mounting the cross-sectioned pit metallographically and polishing the surface. The depth of the pit was measured on the flat, polished surface with a microscope with a calibrated eyepiece. We used a metallographic microscope with a magnification range from 50X to 1000X and a calibrated fine-focus knob (1division = 0.001mm). We recorded the initial reading from the fine-focusing knob on the surface and refocused on the bottom of the pit with the fine-focusing knob and recorded the reading. The difference between the initial and the final readings on the fine-focusing knob was the pit depth. For a X70 carbon steel specimen in seawater for 3 hours under a

stress of approximately equal to 7 MPa and at a temperature of 80 ^{0}C, we got the results shown below (by a magnification of 200X). It should be mentioned that the following results were made with 5 measurements for five different pits and averaged over the region's location. These measurements were made in 5 different regions on the specimen surface:

Focus	108	107	104	106	107	
Defocus	116	116	114	114	115	average = 8.8
Focus	105	109	104	104	108	
Defocus	114	118	114	115	119	average = 9.6
Focus	108	104	105	105	104	
Defocus	114	114	114	112	112	average = 7.4
Focus	107	108	104	104	104	
Defocus	118	118	113	112	114	average = 9.6
Focus	100	101	102	105	108	
Defocus	110	110	114	118	118	average = 10.8

(Mean of the 5 averages/ values) = 9.24 by a magnification of 200 X.

The repeatability of pit-depth measurements on a single pit for different magnifications was our next goal. We expected an exponential reduction of pit depths with increased magnifications, according to similar results from the ASTM standard G 46-94 [137].

As mentioned before, the difference between the initial and the final readings on the fine-focusing knob is the measured pit depth. The focusing knob has 200 scaling grads, and by rotating the knob ten times the whole stage gets a vertical displacement of 1 mm. Thus,

200 x 10 = 2000		windings grads correspond to	1 mm
	9.24	corresponds to	0.00462 mm

9.24 at 200 magnification = (0.00462 / 200) = 2.31×10^{-5} mm

$= 2.31 \times 10^{-2}$ μm

The corresponding estimated mean values from the reading of the focusing and defocusing of objectives on the stressed and unstressed specimens is given in the following tables.

Table 4.2. Unstressed Specimen

Time[hr.]	No. of scale	Pit Depth [μm]
3	6.19	1.55E-02
10	7.87	1.97E-02
72	14.93	3.73E-02
120	18.845	4.71E-02
168	22.93	5.73E-02

Table 4.3. Stressed Specimen

Time[hr.]	No. of scale	Pit Depth [µm]
3	9.24	2.31E-02
10	14.83	3.71E-02
72	24.13	6.03E-02
120	32.16	8.04E-02
168	33.02	8.26E-02

4.1.2.2.7 ***Results***

Table 4.4. Estimated Pit Depth at Different Times for Unstressed Specimen

Time [hr.]	Mean Pit Depth [µm]
3	6.19
10	7.87
72	14.93
120	18.845
168	22.93

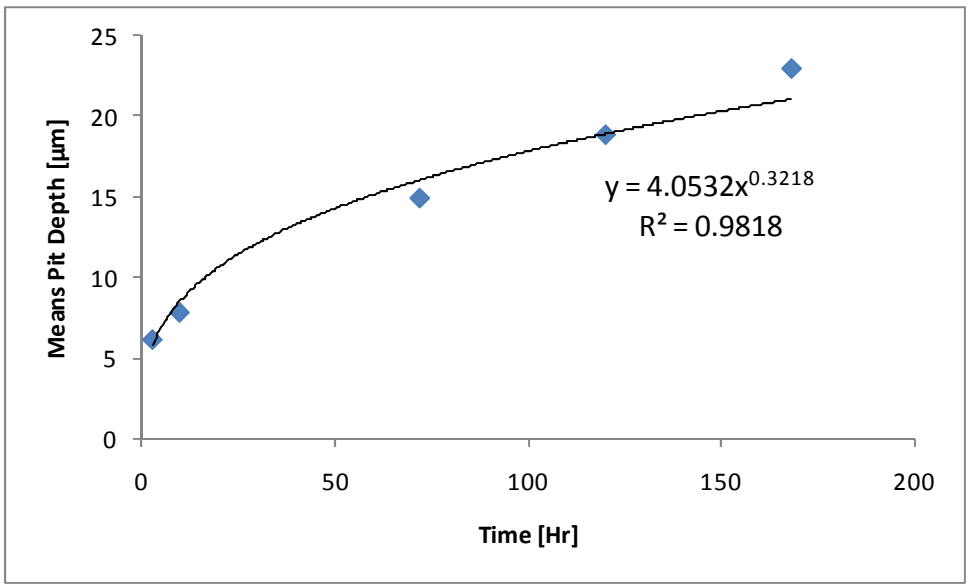

Figure 4.16. Pit Depths Measured as Function of Time for the Carbon Steel. Ordinate is the Difference in Focus and Defocus Differences in the Microscope by 200X Magnification.

Table 4.5. Estimated Pit Depth in [µm] at Different Times for Unstressed Specimen

Time [hr.]	Pit Depth [µm]
3	0.0155
10	1.97E-02
72	3.73E-02
120	4.71E-02
168	5.73E-02

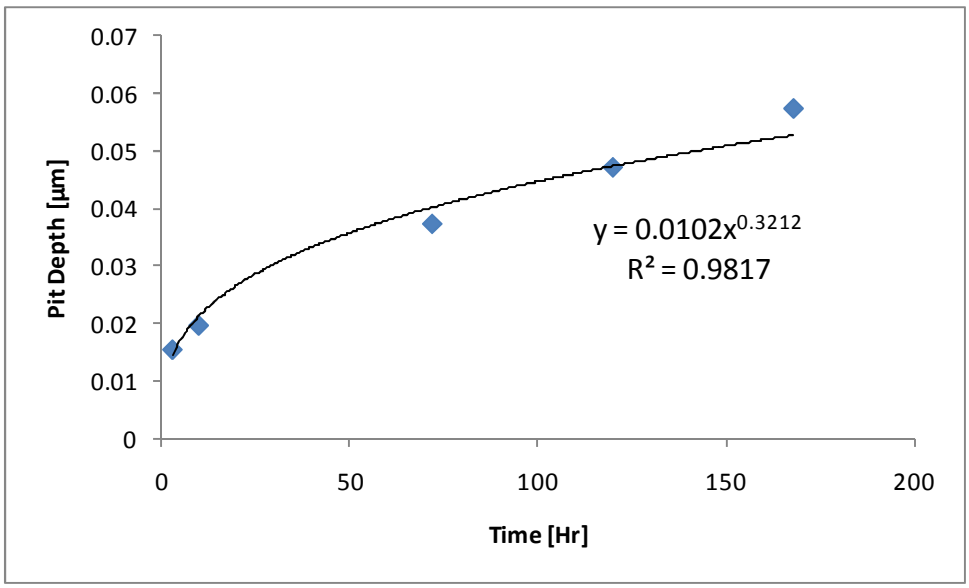

Figure 4.17. Pit Depth Measurement in Seawater + 500ppm H2S for Unstressed Specimen at 800C Given in [µm] versus time [hr].

Table 4.6. Estimated Pit Depth at Different Times for Stressed Specimen

Time [hr.]	Mean Pit Depth [µm]
3	9.24
10	14.83
72	24.13
120	32.16
168	33.02

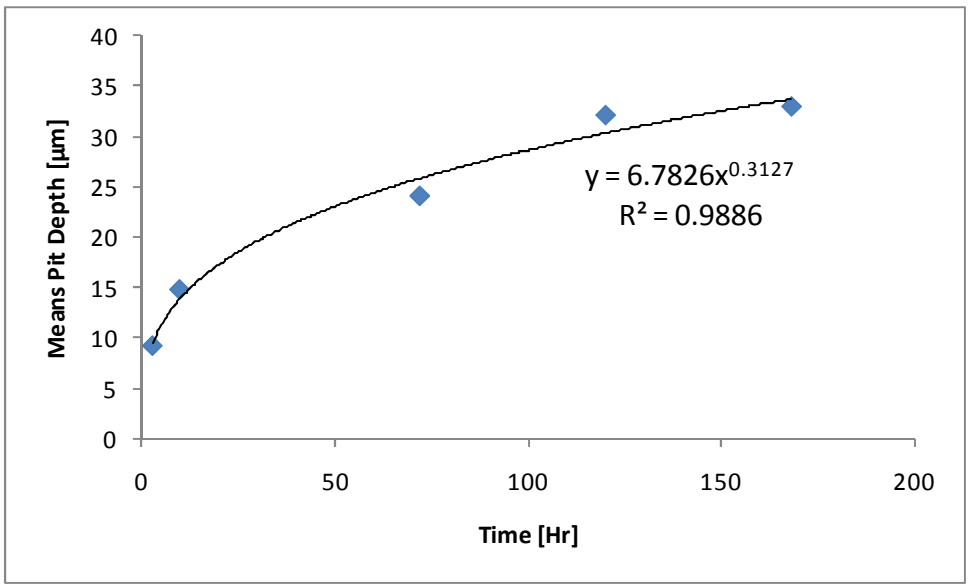

Figure 4.18. Pit Depths Measured as Function of Time for the Stressed Specimen. Ordinate is the Difference in Focus and Defocus Differences in the Microscope by 200X Magnification.

Table 4.7. Estimated Pit Depth at Different Times for Stressed Specimen

Time [hr.]	Means Pit Depth [µm]
3	0.0231
10	3.71E-02
72	6.03E-02
120	8.04E-02
168	8.26E-02

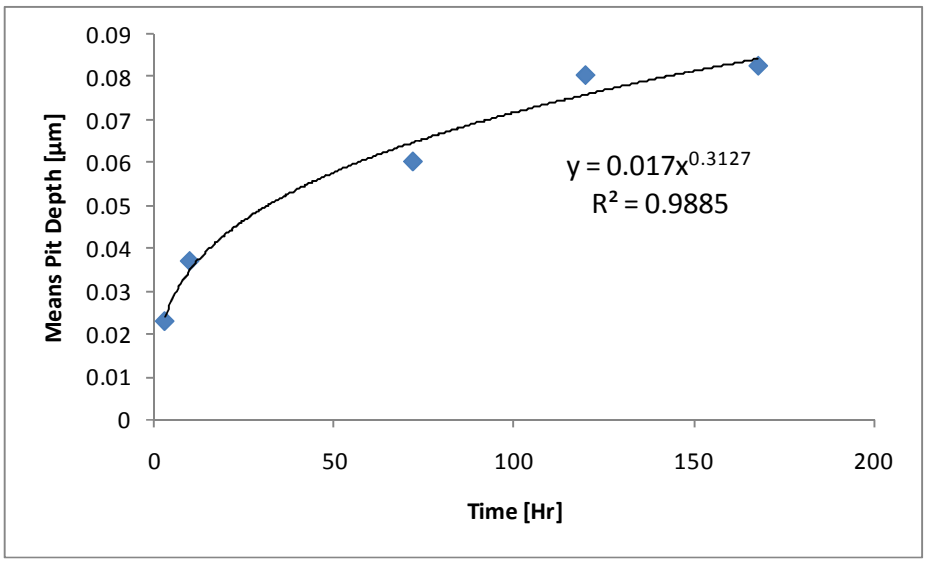

Figure 4.19. Pit Depth Measurement in Seawater + 500ppm H2S for Stressed Specimen at 800C given in [µm] versus Time [hr].

The results show that the pitting corrosion proceeded according to the time power law given in the literature from Hoeppner [13] and Kondo [12] with a 1/3 exponent. This is what we assumed for initiation and growth of cracks in our corrosion-fatigue experiments. In the figure below, the growth of pit depth [µm] with time for stressed and unstressed specimens are compared.

Table 4.8. Comparison Table for Unstressed and Stressed Specimen

Time [hr.]	Unstressed Pit Depth [µm]	Stressed Pit Depth [µm]
3	0.0155	0.0231
10	1.97E-02	3.71E-02
72	3.73E-02	6.03E-02
120	4.71E-02	8.04E-02
168	5.73E-02	8.26E-02

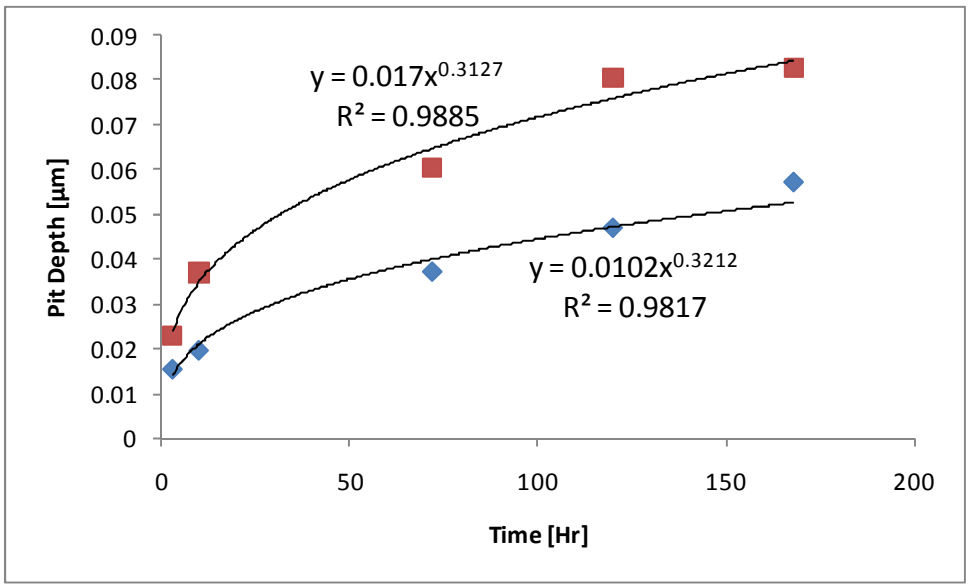

Figure 4.20. Pit Depth Growth with Time for Stressed (red) and Unstressed (blue) Specimens Immersed in Seawater (Chloride) + 500ppm H2S at 800C.

4.2 *Summary*

Pitting corrosion testings at ITS (outsourced lab) and the in-house experiments have several resembling features in both the set-up and the results. However, the equipment used at ITS (profilometer) to measure pit depth has better accuracy than the optical technique used in-house. But, the accuracy in the pit measurement did not prevent applying them for subsequent analysis since it is considered minor and both techniques are susceptible to many varying factors. On the other hand, corrosion-fatigue testing was carried out totally different in both locations. The in-house set-up was superior to the ITS due to a state-of-art equipment availability and environment control feature it offered, but the test was much slower in generating results. ITS set-up was able to

produce sufficient amount of data in a faster time frame, but with highly accelerated (harsh) regimes which would compromise the results desired. Nevertheless, the combination of both data from the two locations (after some streamlining) should be adequate to run the upcoming analysis to estimate the distribution of the proposed empirical model two uncertain parameters.

CHAPTER 5

ANALYSIS & PRACTICAL VALIDATION

5.1 *Introduction*

Earlier a simplest structure for a combined pitting and corrosion-fatigue degradation mechanisms was proposed. However, practical validation of this model in the context of a specific material, use, and environmental characteristic is yet to be accomplished before it can be deployed for actual site usage. The data necessary to achieve this task has been collected as detailed in Chapter 4 which would assist validate (i.e., estimating the two parameters) the proposed empirical model. But, a proper approach to carry out this validation is still need to be determined. Bayesian approach being a powerful mathematical tool that could estimate the two parameters with minimum amount of data was used for this purpose. The generic data generated while simulating Wei's superposition model will play a vital role in the Bayesian approach (i.e., they will help propose prior estimates for the two parameters of the empirical model). At end of this chapter, the proposed empirical model would be practically validated and the two uncertain parameters would be estimated that reflects the actual pipeline variability.

This chapter will begin with a sensitivity analysis to investigate the proposed empirical model's most sensitive parameters. The acquired data in the Chapter 4 will be utilized for the practical estimation of the two uncertain parameters of the proposed empirical

model. Bayesian approach in the form of the accelerated life concept will be jointly applied to estimate the joint distribution of the uncertain parameters.

5.2 *Sensitivity Analysis*

The impact of the various physical and non-physical parameters in the proposed empirical model on the outcomes, mainly the crack size "a," is investigated in this section. To begin the sensitivity analysis, a set of base values was selected for all parameters along with a lower bound and upper bound as shown in Table 5.1.

Table 5.1. Empirical Model Parameters Selected ranges for Sensitivity Analysis.

Parameter	Base Value	Lower Bound	Upper Bound
Temperature (T), K	373	273	1000
Frequency (ν), Hz	3	1.00E-07	10
Loading Stress (σ), Mpa	100	1	200
Corrosion Current (Ip), A	1E-06	1.00E-08	1.00E-04
Number of Cycles (N)	10000	1	1.00E+05
A (mean)	1.324E-05	1.00E-06	1.00E-04
B (mean)	1.443E-19	1.00E-20	1.00E-18

A computer program called TopRank was deployed to run the sensitivity analysis. This program in Excel approaches sensitivity analysis by recalculating the spreadsheet many times for different inputs, as in Table 5.1 above. After running the TopRank program, Figures 5.1 and Tables 5.2/5.3 were produced as shown below.

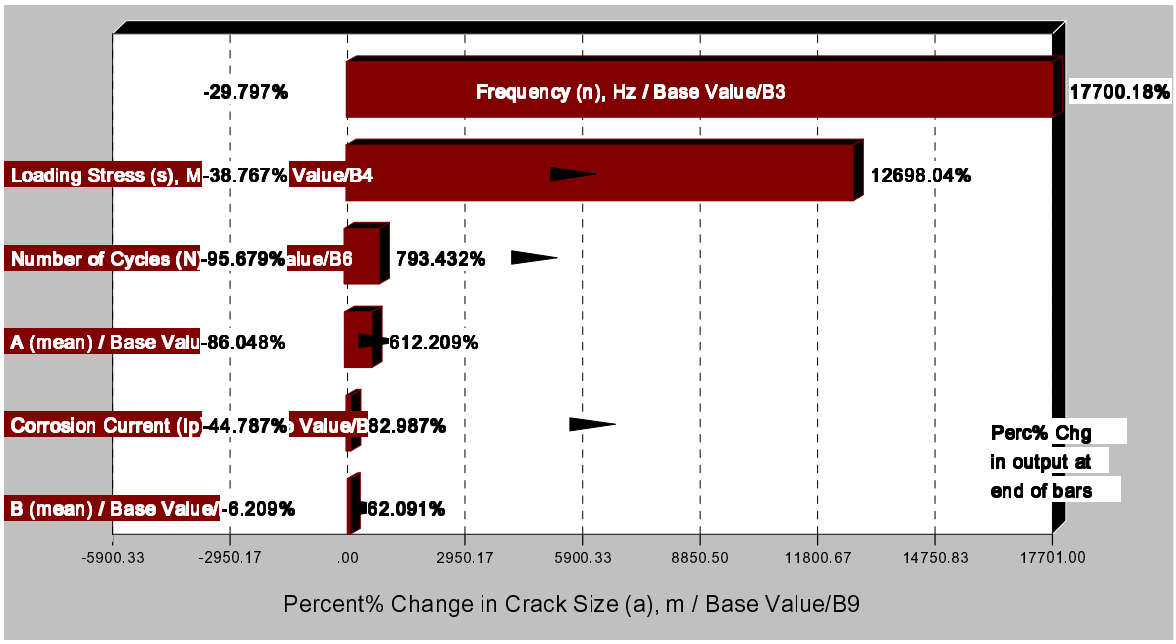

Figure 5.1. Tornado Graph for Crack Size "a."

Table 5.2. Ranking of Crack Size "a" for Most Significant Inputs from What-if Results for Sensitivity Analysis in Percent Outputs.

Rank	Cell	Name	Output Max	When Input Value=	Output Min	When Input Value=
#1	B3	Frequency (ν), Hz / Base Value	17700.18%	1E-07	-29.80%	10
#2	B4	Loading Stress (σ), Mpa / Base Value	12698.04%	100	-38.77%	1
#3	B6	Number of Cycles (N) / Base Value	793.43%	100000	-95.68%	1
#4	B7	A (mean) / Base Value	612.21%	0.0001	-86.05%	0.000001
#5	B5	Corrosion Current (I_p), A / Base Value	82.99%	0.001	-44.79%	0.00001
#6	B8	B (mean) / Base Value	62.09%	1.00E-14	-6.21%	1.00E-16

Table 5.3. Ranking of Crack Size "a" for Most Significant Inputs from What-if Results for Sensitivity Analysis in Actual Outputs.

Rank	Cell	Name	Output Max	When Input Value=	Output Min	When Input Value=
#1	B3	Frequency (ν), Hz / Base Value	0.006137	1E-07	0	10
#2	B4	Loading Stress (σ), Mpa / Base Value	0.004413	100	0	1
#3	B6	Number of Cycles (N) / Base Value	0.000308	100000	0	1
#4	B7	A (mean) / Base Value	0.000246	0.0001	0	0.000001
#5	B5	Corrosion Current (I_p), A / Base Value	0	0.001	0	0.00001
#6	B8	B (mean) / Base Value	0	1.00E-14	0	1.00E-16

The tornado diagram in Figure 5.1 clearly indicates that the proposed empirical model is most sensitive to the number of frequency parameter. Note that "N" was treated deterministically rather than probabilistically distributed, since in real situations it is a variable single figure reflecting either a cycle to failure or targeted operation duration. On the other hand, all other parameters had fallen way behind "N" for many possible reasons that are difficult to assess due to the nature of the sensitivity analysis. The selected bases and lower/upper bounds fundamentally affect the outcome of the sensitivity analysis in the TopRank program. Altering the ranges for empirical model parameters would produce different results showing the proposed empirical model sensitive to a different parameter each time. Nevertheless, this non-coherence in the outcomes of the sensitivity analysis indicates that a correlation does exist among all the empirical model parameters that affect the sensitivity analysis outcomes. Also, the non-

linear form of the proposed empirical model calls for more advanced calculating tools to run the sensitivity analysis, which is beyond the scope of this research and does not have a fundamental impact on the major outcomes of this research.

5.3 *Bayesian Estimation*

In this research, the ranges of the proposed empirical model parameters A and B have been estimated from generic data available in literature. A great analytical tool that enables us to integrate the new evidence with the existing knowledge and produce update knowledge is Bayes' theorem. Also, Bayesian estimation is advantageous in the case of sparse data, which does exist in our case. Obtaining data for corrosion-fatigue degradation or conducting experiments has proven to be difficult and very expensive. As such, the Bayesian estimation method was applied in this research to estimate parameters A and B of the proposed empirical model. In this section, a brief discussion of this approach is provided and readers are encouraged to review [138,139] for details about the Bayesian method.

As a useful tool to calculate conditional probability, Bayes' theorem has the following general form:

$$\Pr\left(\underline{\theta}\middle|t\right) = \frac{\Pr\left(\underline{\theta}\right)\cdot Pr(t|\underline{\theta})}{\Pr\left(t\right)} \qquad 5.1$$

where $Pr(\underline{\theta})$ is the prior probability and $Pr(\underline{\theta}|t)$ is the posterior probability given the evidence of t. Thus, the probability of a vector parameters, $\underline{\theta}$, is updated based on the

availability of evidence t , and this updating process can be repeated continuously as more evidences t emerges. If $\underline{\theta}$ is a continuous random variable, then Bayes' theorem would be written in the following form,

$$f(\underline{\theta}|t) = \frac{h(\underline{\theta})\cdot l(\underline{\theta}|t)}{\int_{-\infty}^{\infty} h(\underline{\theta})\cdot l(\underline{\theta}|t)d\underline{\theta}} \quad 5.2$$

where $h(\underline{\theta})$ is the continuous prior pdf of $\underline{\theta}$, $l(\underline{\theta}|t)$ is the likelihood function based on sample data t, and $f(\underline{\theta}|t)$ is the posterior pdf of $\underline{\theta}$.

Since parameters A and B of the empirical model are continuous random variables, Equation 5.2 was applied in the updating process. The most challenging part in our analysis was the denominator, which cannot be expressed in a closed form, so a numerical integration was required. To accomplish this task, WinBUGS software program was employed to run the Bayesian analysis. Subsequent sections describe the use and outcomes of this program.

5.4 *WinBUGS Routine Program for Estimating A & B Distributions*

In Chapter 3, parameters A and B of the proposed empirical Equation 3.15 were initially estimated using the generic data produced from Wei's superposition model in MATLAB. This estimation requires further validation before it can be deployed for additional analysis. Hence, Bayesian approach was utilized to investigate the validity of this prior estimation and then was applied to the updating procedure.

The generic data of crack size "a" vs. number of cycles "N" generated from the superposition model in MATLAB was applied in the Bayesian approach. Here the concept of the accelerated life along with the Bayesian approach would jointly estimate A and B distributions. Figure 5.2 displays the crack size "a" conditions at three stress levels.

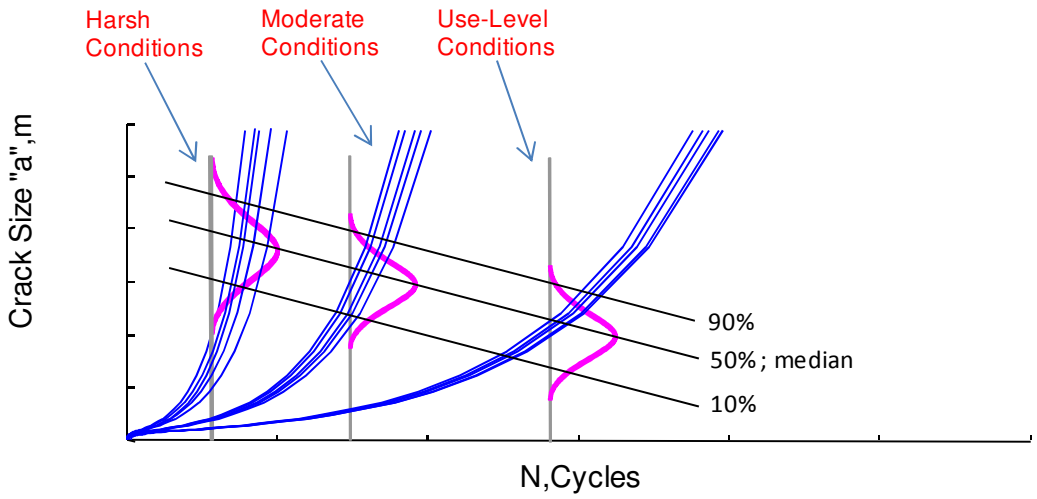

Figure 5.2. Crack Size "a" Distributions at Three Different Stress Levels.

Each stress level in Figure 5.2 is influenced by a set of conditions:

$$\text{Conditions} \begin{cases} \sigma_i \\ T_i \\ \nu_i \\ Ip_i \\ N_i \end{cases} \rightarrow \quad a_i$$

The likelihood equation of the crack size is assumed to follow a lognormal distribution, and the stress-life relationship for different percentiles of this distribution is expressed with the proposed empirical model:

$$f(a_i) = LN(\mu_i, s_i) \tag{5.3}$$

Where, "*s*" is the standard deviation.

Since the median of the crack size "a_i" μ_i, maybe replaced with the natural logarithm of the median life (i.e. 50%), one can therefore conclude,

$$\mu_i = \ln[f(\sigma_i, T_i, \nu_i, Ip_i, N_i)] \tag{5.4}$$

Here, $f(\sigma_i, T_i, \nu_i, Ip_i, N_i)$ is the proposed empirical Equation 3.15. The choice of the median to represent μ_i of the crack size lognormal distribution is due to the fact that as applied stresses change, the various percentiles of the distribution (see Figure 5.2) form parallel lines which would allow extrapolating to other stress levels. This is an inherent characteristic of acceleration and if the percentile lines are not paralleled then it is likely that a mechanism shift may have occurred. Conversely, the mean of the distribution would not be a practical choice since it will not produce the paralleled lines for the various percentiles.

So, the median, μ_i, can be rewritten as follows:

$$\mu_i = ln\left[A \cdot \sigma^{0.182} \cdot \nu^{-0.288} \cdot I_p^{0.248} \cdot N^{1/3} + B \cdot \sigma^{3.24} \cdot \nu^{-0.377} \cdot I_p^{0.421} \cdot N^2 e^{\left(4\times10^{-10}\cdot\sigma^{2.062}\cdot\nu^{0.024}\cdot N\right)}\right] \quad 5.5$$

Substituting equation 5.5 into the lognormal distribution, the distribution function of the crack size "a" can be presented as follows:

$$L(a) = f(a) = \frac{1}{s\cdot a\sqrt{2\pi}} exp\left[-\frac{1}{2s^2}\left(lna - ln\left(A \cdot \sigma^{0.182} \cdot \nu^{-0.288} \cdot I_p^{0.248} \cdot N^{1/3} + B \cdot \sigma^{3.24} \cdot \nu^{-0.377} \cdot I_p^{0.421} \cdot N^2 e^{\left(4\times10^{-10}\cdot\sigma^{2.062}\cdot\nu^{0.024}\cdot N\right)}\right)\right)^2\right] \quad 5.6$$

When data (i.e. crack size, stress, temperature, frequecy and corrosion current) become available, Equation 5.6 will simply serve as the likelihood of data given parameters A and B. Having the likelihood of data developed in Equation 5.6, one can derive the posterior distribution of parameters A and B utilizing Bayes' conditional probability theorem as follows:

$$f(A,B,s|a_i) = \frac{f_o(A,B,s)\cdot L(A,B,s|a_i)}{\int f_o(A,B,s)\cdot L(A,B,s|a_i) dA dB ds} \quad 5.7$$

where

- $f_o(A, B, s)$ is the subjective prior distribution (e.g. non-informative uniform distribution). This prior distribution was later updated using the experimental data from ITS and in-house experiments.
- The likelihood $L(A, B, s|a_i)$ is representing each data point i. The individual likelihood functions can be multiplied to create the global likelihood of data based on the independency assumption:

$$L(A, B, s|a_i) = \prod_{i=1}^{N} \ln(\mu_i, s_i) \quad 5.8$$

In the general form, there is no analytical solution available for Equation 5.7. In this application, Bayesian posteriors of $\underline{\theta}$ are usually estimated using sophisticated sampling approach, such as the Markov Chain Monte Carlo (MCMC) [140]. In this method the posterior function is recreated by generating enough samples rather than by direct integration. In this method, a sample drawn from a generating distribution is modified through a series of conditional probability calculations until becomes a sample of the target posterior. The WinBUGS program [141] is a windows-based environment for MCMC simulation. This program has been previously used in uncertainty management [142] as well as accelerated life testing data analysis [143] and has proved to be a reliable tool for such calculations. In this research the WinBugs platform was used for Bayesian updating and related numerical simulations. Figure 5.3 describes the algorithm of the Bayesian inference implemented in WinBUGS.

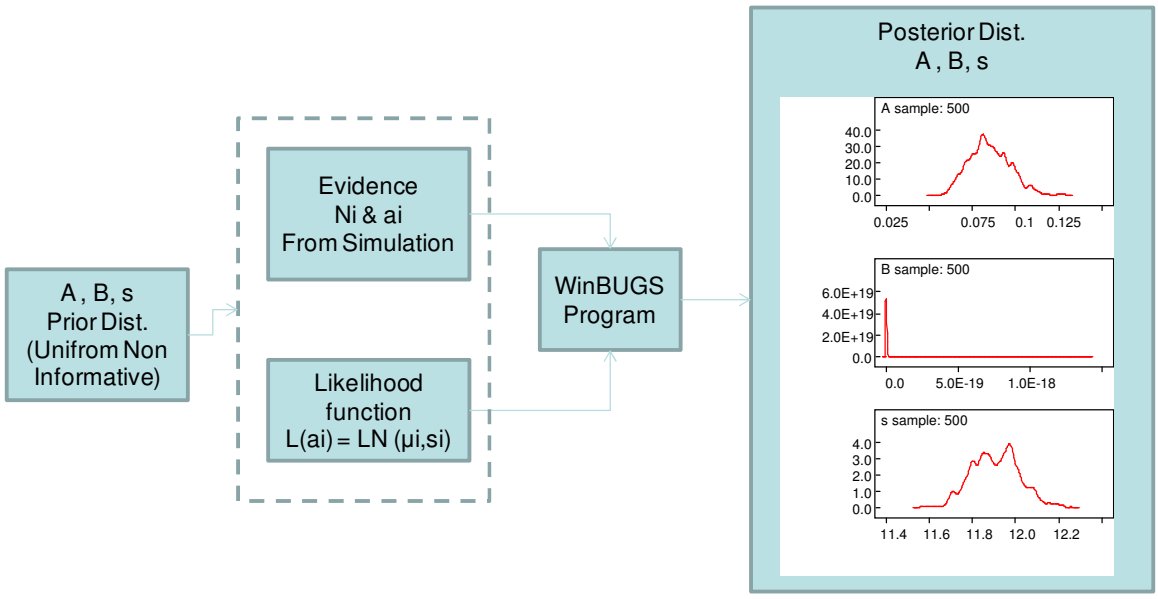

Figure 5.3. Basic Algorithm for the WinBUGS Program to Calculate A, B, and s Posterior Distributions.

The first run for the WinBUGS program revealed a convergence problem to obtain the joint distributions for A, B, and s. To investigate, it was necessary to look into the plot of crack size "a" versus number of cycles "N" generated from Wei's superposition model once again.

Figure 5.4 shows the plot of "a" vs. "N" on a log-log scale.

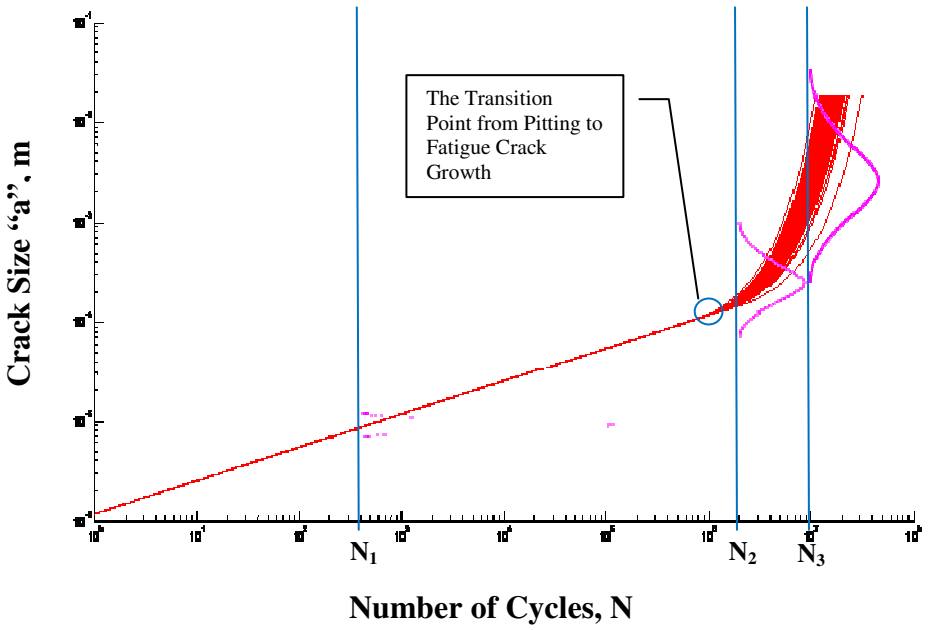

Figure 5.4. Plot of Crack Size "a" vs. Number of Cycles "N" on Log-Log Scale.

As shown in above figure, the pitting corrosion segment has no uncertainty, since the crack size model at this region is basically a deterministic mode. Thus, A shows no uncertainty, and if it did, it would simply be because of the nature of proposed empirical model where the variability over B reflects on A. On the other hand, a relatively wide uncertainty in the fatigue crack growth part is basically influenced from uncertainty considered in parameters C_c, C_r, and κ_o. This uncertainty is for the most part captured with parameter σ in the lognormal distribution, leaving no room for parameters A and B to take part in uncertainty of "a". The deterministic nature of the pitting corrosion section of the simulation requires a closer look at the transitional point in Bayesian numerical simulation.

To capture this evidence in the WinBUGS program to obtain more competent results for the empirical model parameters, the second derivative of the proposed empirical model was necessary. The change in the transition point from the pitting corrosion region to the fatigue crack growth region needed to be well addressed in the program. As evident from Figure 5.4, the slope of the pitting corrosion part of the curve tends to be positive until it reaches the transition point, where it changes to negative for the fatigue crack growth part. Thus, taking the second derivative of the proposed empirical model will aid in segregating the pitting corrosion data from the fatigue crack growth data for a better uncertainty management. So by taking the 2nd derivative of Equation 3.15 we get

Set,

$$\alpha = \sigma^{0.182} \cdot \nu^{-0.288} \cdot I_p^{0.248}$$

$$\beta = \sigma^{3.24} \cdot \nu^{-0.377} \cdot I_p^{0.421}$$

$$\gamma = 4 \times 10^{-10} \cdot \sigma^{2.062} \cdot \nu^{0.024}$$

Then Equation 3.15 could be rewritten,

$$a = A\alpha N^{1/3} + B\beta N^2 e^{\gamma N}$$

Taking the 2nd derivative,

$$\frac{\partial a}{\partial N} = \frac{1}{3} A\alpha N^{-2/3} + 2B\beta N e^{\gamma N} + \gamma B\beta N^2 e^{\gamma N}$$

$$\frac{\partial^2 a}{\partial N^2} = -\frac{2}{9} A\alpha N^{-5/3} + 2B\beta e^{\gamma N} + 2B\beta\gamma N e^{\gamma N} + 2\gamma B\beta N e^{\gamma N} + \gamma^2 B\beta N^2 e^{\gamma N} \quad 5.9$$

$\frac{\partial^2 a}{\partial N^2} = 0$ at the transition point, so Equation 5.7 could be rearranged as,

$$\frac{2}{9} A\alpha N^{-5/3} = 2B\beta e^{\gamma N}\left(1 + 2\gamma N + \frac{1}{2}\gamma^2 N^2\right) \quad 5.10$$

Now Equation 5.10 could be loaded in the earlier written WinBUGS program to generate the more relevant results for the A and B distributions and discarding other results.

5.5 *Bayesian Approach & Practical Validation*

In Chapter 4, the pitting and corrosion-fatigue tests for the X70 carbon steel CT specimens generated the data needed to update the empirical model parameters A and B. Here, the Bayesian approach is the key tool for achieving the updating process for A and B estimations that were generated earlier using generic data. The general steps in the new coded routine program in WinBUGS resembled that in Figure 5.3, where now instead of using evidence from simulation for a_i and N_i, now it is the new evidence obtained from experiment. Figure 5.5 displays these modified steps to obtain the posterior distributions of the A and B parameters of the proposed empirical model.

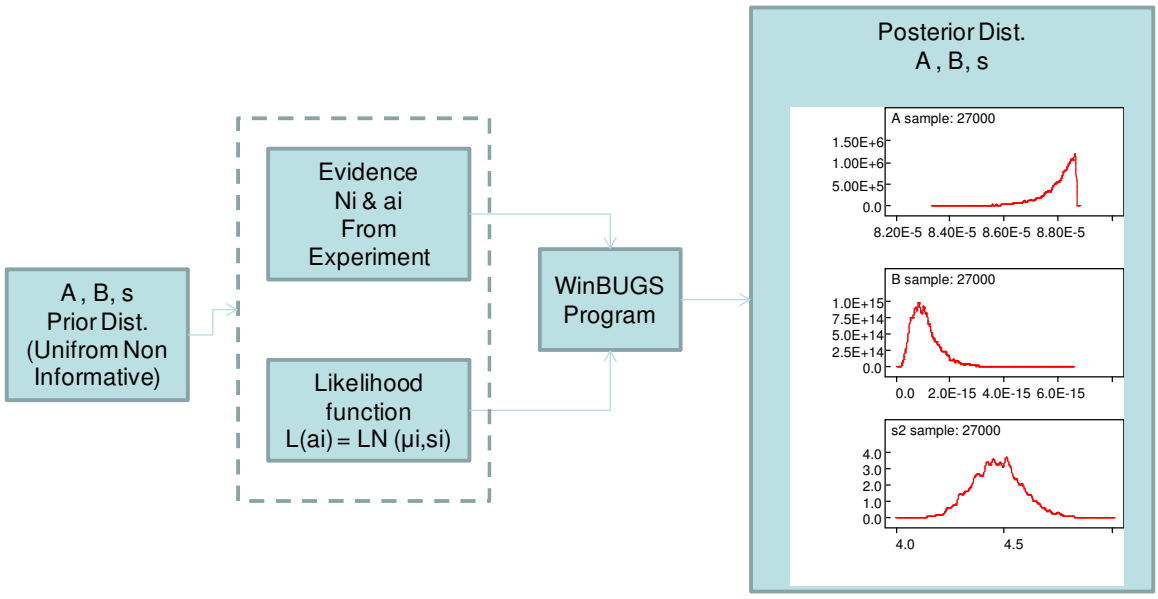

Figure 5.5. Algorithm for the Bayesian Approach in the WinBUGS Program to Calculate A, B, and s Posterior Distributions.

With the experimental data now available, the posterior distributions for A and B parameters were estimated and shown in Table 5.4 and Figure 5.6.

Table 5.4. A, B, and σ Posterior Distributions as Calculated in WinBUGS for 27000 Samples.

node	mean	sd	MC error	2.5%	median	97.5%	start	sample
A	8.795E-5	7.048E-7	1.353E-8	8.601E-5	8.817E-5	8.866E-5	4001	27000
B	1.096E-15	1.0E-10	6.086E-13	3.725E-16	9.977E-16	2.445E-15	4001	27000
logA	-9.339	0.008074	1.549E-4	-9.361	-9.336	-9.331	4001	27000
logB	-34.56	0.4771	0.006674	-35.53	-34.54	-33.64	4001	27000
s2	4.468	0.1188	0.001511	4.244	4.466	4.711	4001	27000

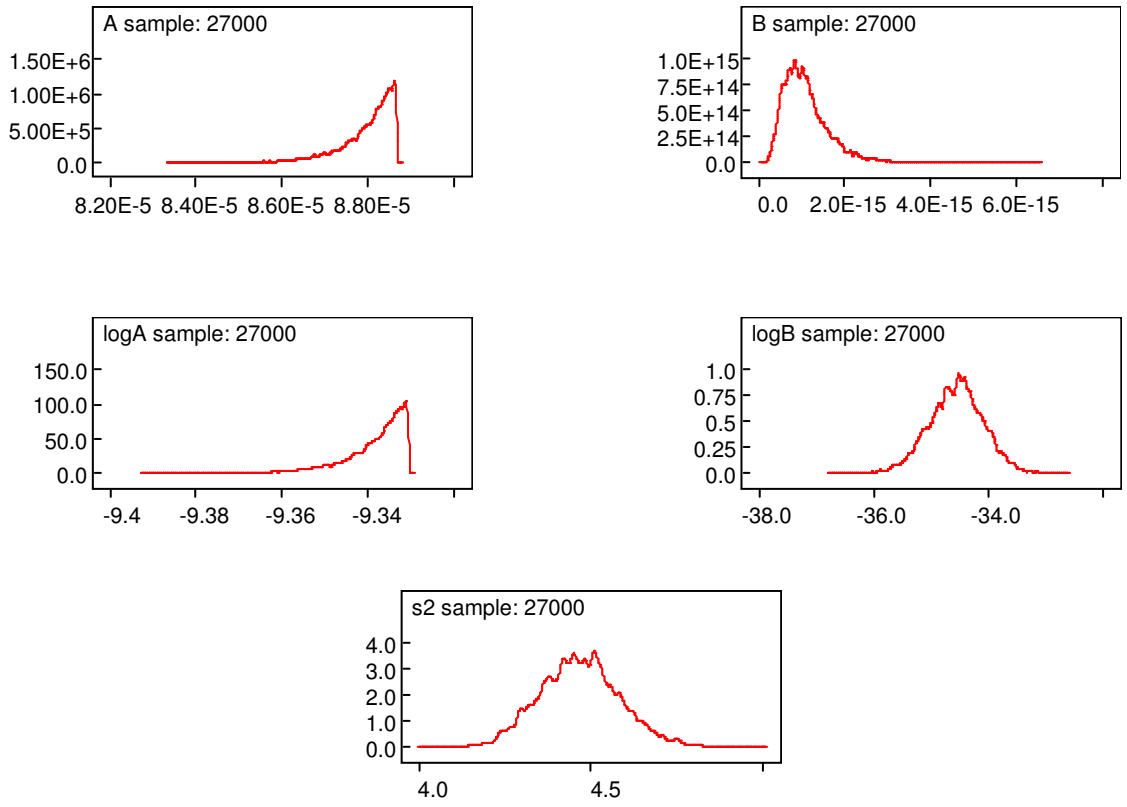

Figure 5.6. A, B, and σ Posterior Distributions as Calculated in WinBUGS.

So from above it could be argued that A, B, and s can be obtained by using again a uniform non-informative distribution. This was examined by another run in WinBUGS to reveal very close answers supporting the argument. Nevertheless, the generated posterior distributions for A and B now reflect the actual distributions for the X70 carbon steel pipelines in the refinery.

5.6 *Summary*

The data gathered from the experiments as detailed in Chapter 4 played a vital role in practically estimating the joint posterior distributions for uncertain parameters A and B of the proposed empirical model. The Bayesian approach implemented via the WinBUGS program and jointly with the accelerated life modeling concept had facilitated estimation of the joint distributions of A, B, and *s* especially when the prior data assumed to be non-informative uniform distributions. Now the proposed empirical model parameters A and B accounts for the real variability in the pipeline (assuming an aqueous medium with Cl^- and H_2S being the main corrosive species). So, with the newly obtained A and B distributions, our proposed empirical model has been validated and its parameters estimated. It can be used to estimate the remaining life of the pipeline probabilistically, which will be discussed in Chapter 6.

CHAPTER 6

EMPIRICAL MODEL APPLICATION

6.1 *Introduction*

This research was inspired by the degradation phenomena of pitting and corrosion-fatigue in pipelines. The ability to predict the remaining life of these pipelines was the ultimate objective. Now that the empirical model has been proposed and validated experimentally, the task that remains is to show actual applications of the model to existing pipelines. There are more chemical agents at work in the oil pipelines, however this model was only validated and the model parameters estimated in a water-based aqueous solution (with Cl^- and H_2S being the only corrosive species). This is an approximation which is generally a good one. Corrosion-fatigue failures of pipelines supposedly occur following a long period of service, but there are also cases where failures can occur in shorter periods if accelerating factors such as a very high pressure, high frequency, and high concentrations of corrosive agents exist. In this chapter the proposed empirical model with the values of A and B estimated from an aqueous environment will be deployed to probabilistically estimate the remaining life of an existing pipeline in a refinery (Ruwais refinery located in Abu Dhabi, UAE).

6.2 *Scenario Description & MATLAB Routine Program*

In this section, the selected scenario would be for long-servicing pipelines, which account for the most common operation mode in the refinery. The data for the example application was collected and investigated from the Ruwais Refinery located 220 Km west of capital of the United Arab Emirates, Abu Dhabi. In brief, the Ruwais refinery was built and brought on-line in 1981 with 186,000 barrels/day capacity, having only Hyrotreater and Hydrocracker processing units. In 1999, condensate processing units were added to increase the capacity of the refinery to 450,000 barrels/day. The cracking unit in the Hydrocracker processing plant had a case of corrosion-fatigue failure. The vent pipeline for the HVGO (heavy vacuum gas oil) pump (103-TG-01) discharge line cracked at the weld joint. The refinery investigation for the failure revealed the possibility of corrosion-fatigue as being the driving degradation mechanism. This line served from 1982 to 2007 for a total of 25 years. The following pipeline operating conditions and specification were gathered:

- Pipeline material: carbon steel (API 5L Grade B)
- Medium flow: heavy vacuum gas oil
- Operating temperature (T): 443 K
- Operating pressure (P): 6 Kg/cm^2 ~ 1.547 MPa
- Loading frequency (ν): 4.76×10^{-7} Hz
- Wall thickness (a_f): 0.00635 meters
- Service life (N): 375.2784 cycles

Adopting the methodology presented in [144], the cyclic service life of the pipeline was determined from the flow digital records of the pump as shown in Figure 6.1.

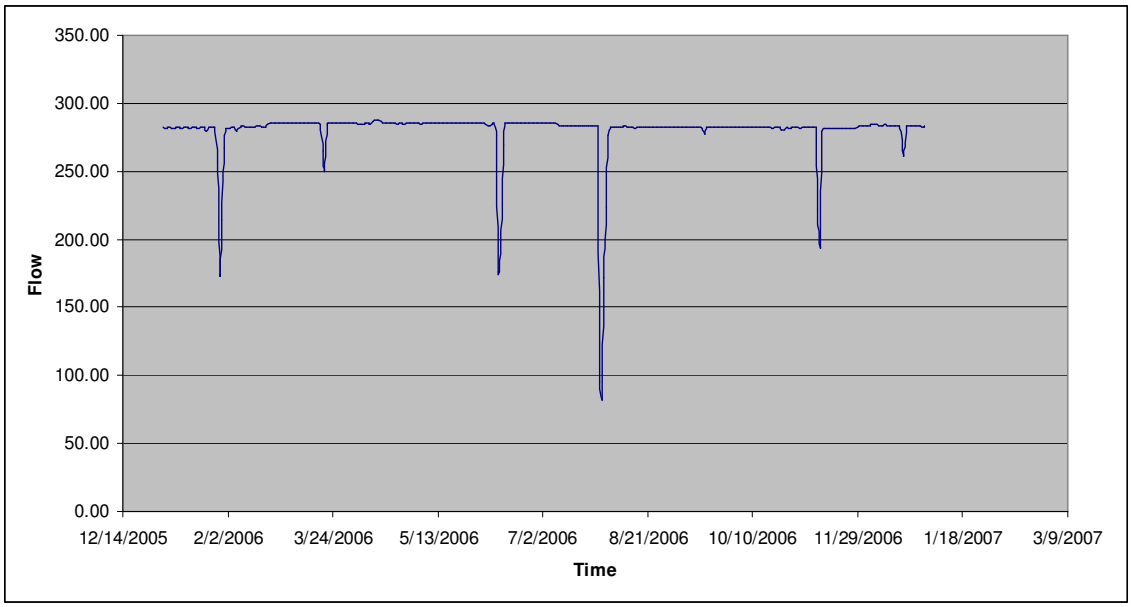

Figure 6.1. Flow Records for One Year of Pump 103-TG-01 (Courtesy Ruwais Refinery).

The cycles in the profile were counted for all the interrupted operation, shutdown, and upset conditions. The crack-size growth record was not available since only the laboratory setting was capable of providing such record. Hence, the above inputs are missing only the empirical model parameters A and B for running the simulation to assess the pipeline remaining life. In Chapter 5, the Bayesian analysis generated the empirical model parameters A and B Lognormal distributions based on the experimental data. They are:

$$A \begin{cases} \mu = -9.34 \\ s = 7.41\times10^{-3} \end{cases} \qquad B \begin{cases} \mu = -34.5234 \\ s = 0.4686 \end{cases}$$

All the gathered and generated data was incorporated into MATLAB to produce the desired result. Figure 6.2 depicts the flow diagram for the routine program written in MATLAB.

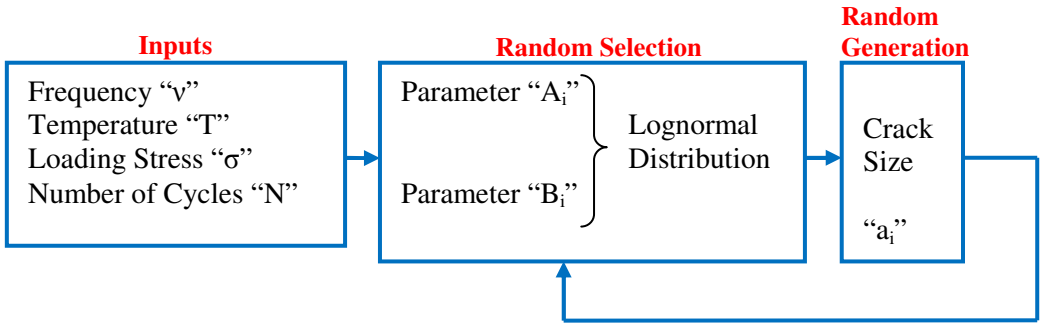

Figure 6.2. Flow Chart for the MATLAB Routine Program to Generate the Crack Size Distribution.

6.3 *Probabilistic Risk Assessment Analysis*

The updated empirical model was utilized to run the simulation and obtain the crack size "a_i" values, which were then fitted normally (see Figure 6.3). The following were the outcomes.

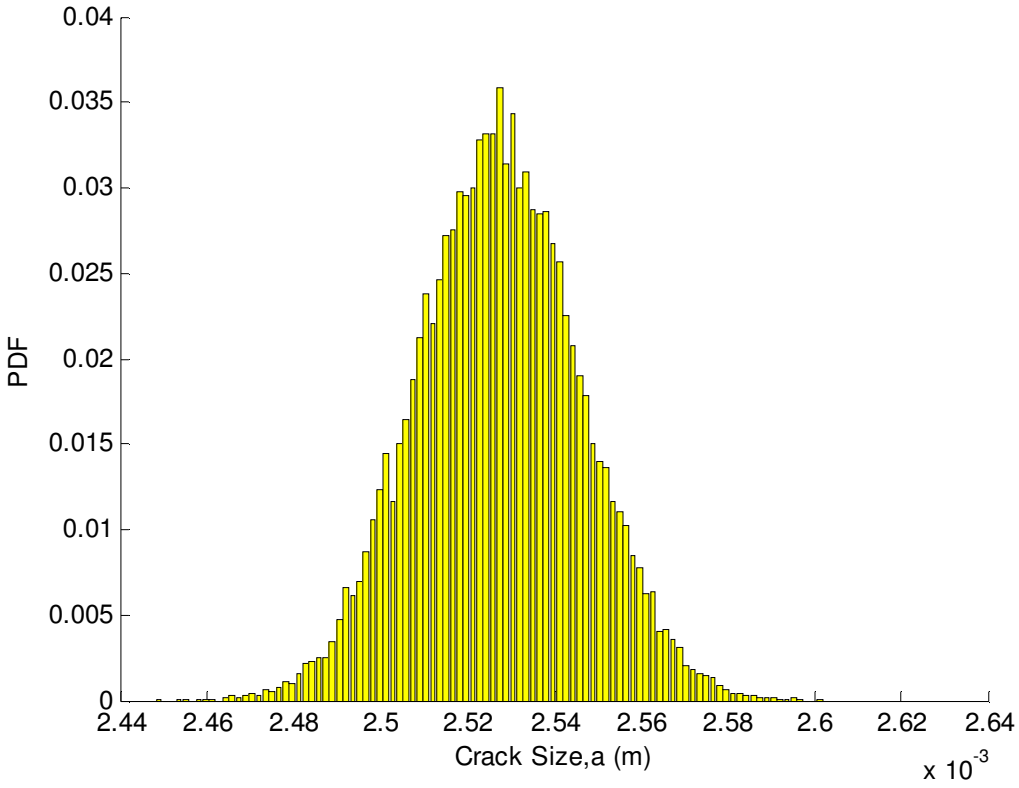

Figure 6.3. Normal pdf of the Crack Size "ai."

- Parameters for "ai" Normal distribution: $\mu = 0.0025$; $s = 1.8736 \times 10^{-5}$
- The cdf value for a crack size of 0.00635 m was near 1

From the outcomes, the probability of a crack reaching the surface of the pipeline for complete fracture is negligible. This almost nil probability is what we expected, knowing such type of pipeline failure happens extremely rarely. The corrosion-fatigue phenomenon does occur over a long period of time and eventually if the crack goes undetected; it will cause a complete crack-through. However, over the past 25 years there

have been only rare occasions of such incidents; and our model outcome is consistent with the industry's historical experience.

To estimate applications that are varied from conditions of the above refinery pipeline life, the conditions were altered. Consider a case where the frequency is 0.0015 Hz. Thus, with the newly assumed frequency for the pipeline loading, the new number of cycles for 25 years of pipeline service is 1182600 cycles. Once again, the empirical model was utilized to run the simulation and obtain the crack size "a_i" values, which were then fitted lognormally (see Figure 6.4). The following were the outcomes.

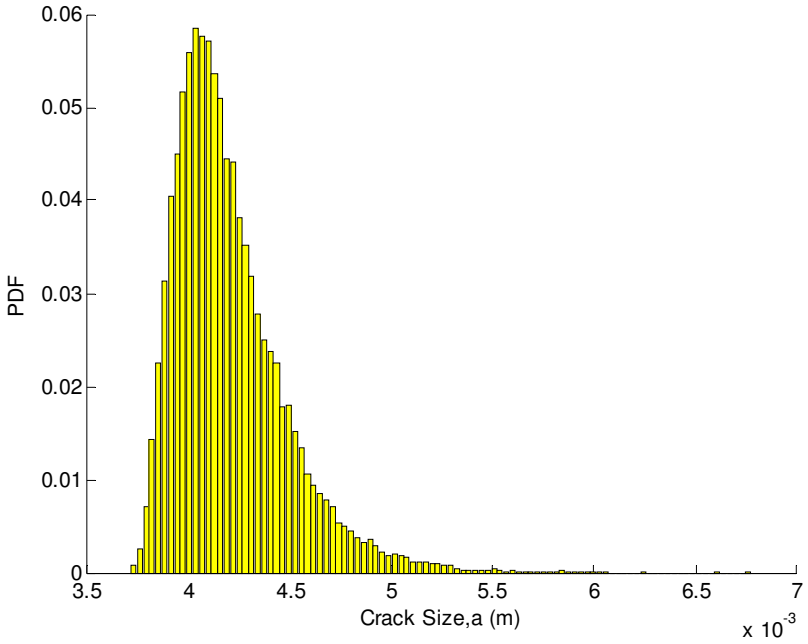

Figure 6.4. Lognormal pdf of the Crack Size "ai" for Higher Loading Frequency.

- Parameters for “ai” lognormal distribution: μ= -5.47 ; s=0.06
- The cdf value for a crack size of 0.00635 m was near 1

From the outcomes, the probability of a crack reaching the surface of the pipeline for complete fracture is 3.3×10^{-11} which is a negligible probability. However, this probability is merely for assessing the pipeline with the assumption of having only one pit. Whereas, a particular type of refinery pipeline resembling the one in the above example would amount for large lengths accounting more pits. Hence, the above exercise needs to be extended to investigate the actual probability of the whole bulk of the pipeline.

In Chapter 4, the conducted pitting corrosion testing revealed counting 14 pits per μm^2 of specimen area which is equivalent to 2.24 pits per dm^2. Assuming a Poisson distribution, the probability of observing specific number of pits was estimated which is shown in Figure 6.5,

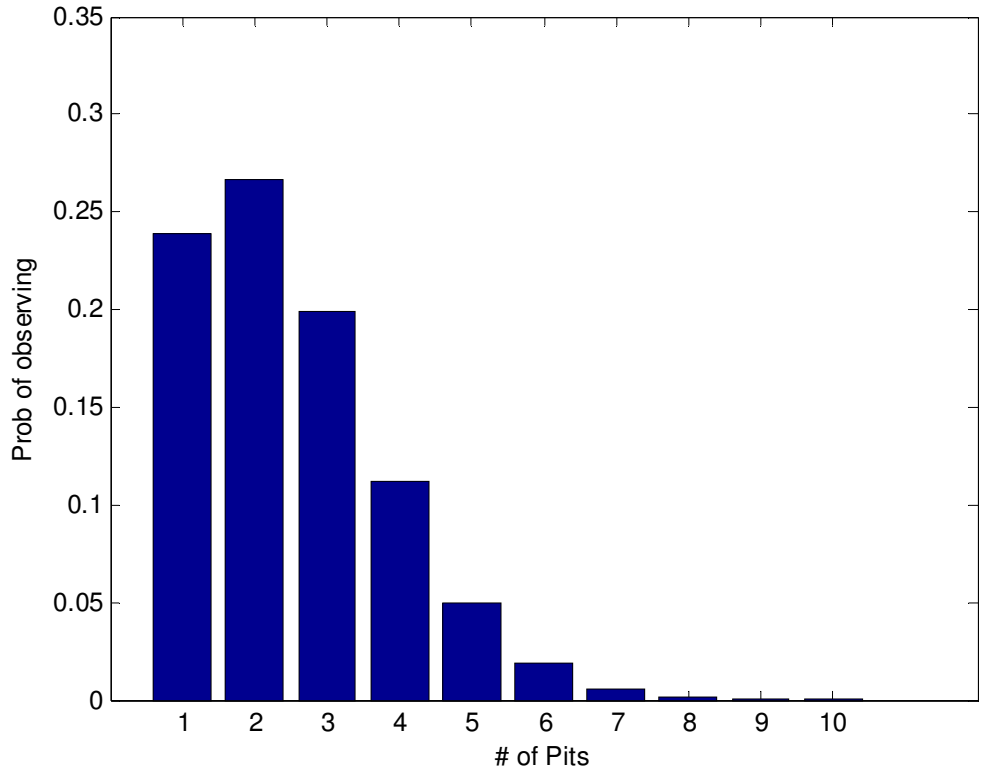

Figure 6.5. Probability of Observing Specific Number of Pits for Refinery Pipeline.

As can be seen in Figure 6.5, fewer number of pits reflects a higher probability of observance compared with the larger numbers and this consistent with assumed Poisson distribution expectation. Now, the result in Figure 6.5 is combined with the earlier calculated probability of exceeding, 3.3×10^{-11}, the assumed crack size in the refinery pipeline example, which is 0.00635m, to estimate the frequency of exceedance for each number of observed pits as shown in Figure 6.6,

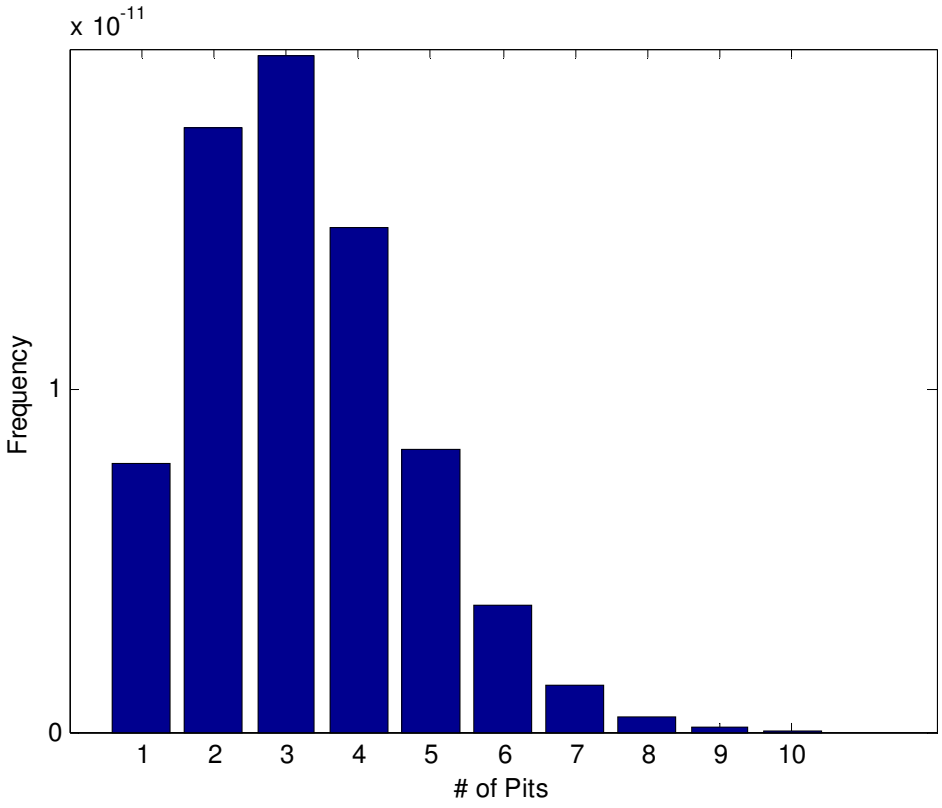

Figure 6.6. Frequency of Exceedance for Each Observed Number of Pits in the Refinery Pipeline.

Figure 6.6 reveals again higher frequency of exceedance for the fewer observed pits as compared with the larger observed ones. The results in Figure 6.6 were aggregated to estimate the frequency of exceedance for all observed pits in the pipeline which is 7.4×10^{-11}. Now, assuming having a one mile long pipeline, which is just about the same typical total length in a refinery, the total frequency of exceedance for the bulk pipeline is estimated to be 9.4×10^{-6} pipeline failure/25 yrs life of pipeline. So, increasing the pipeline loading frequency while keeping all other loading conditions unchanged; augmented the probability of pipeline failure giving a high likelihood that any segment of this pipeline would experience a failure due to a corrosion-fatigue cracking.

Now, consider a harsher environment that accounts for a more corrosive flow medium, higher H_2S and Cl^- concentrations, translated to a higher corrosion current equivalent to 1.0×10^{-5}A. In this case, the empirical model would produce the following lognormal distribution of "a_i",

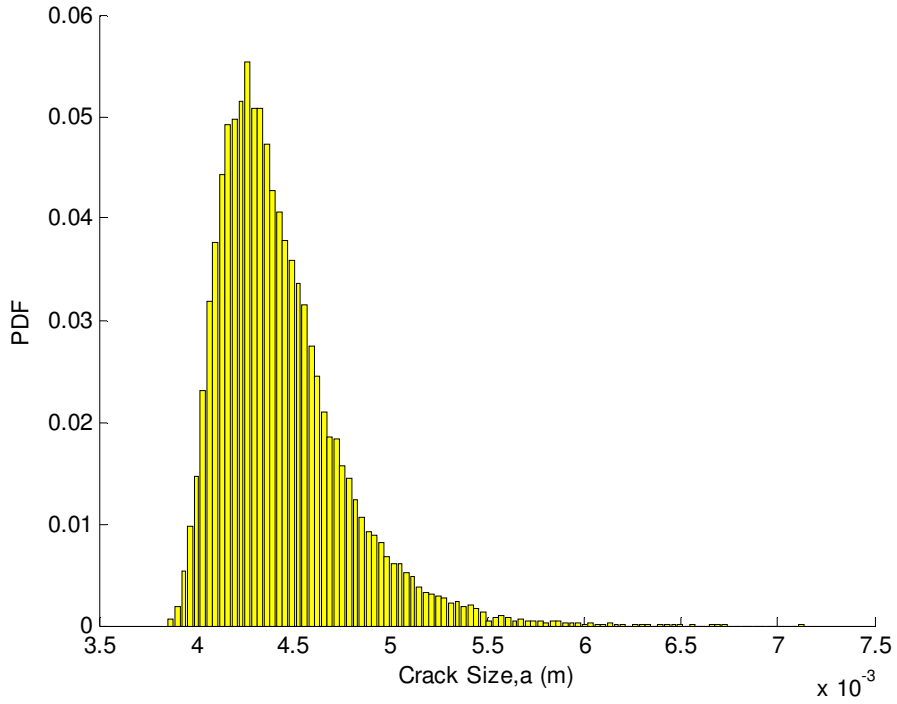

Figure 6.7. Lognormal pdf of the Crack Size "ai."

- Parameters for "ai" lognormal distribution: $\mu = -5.42$; $s = 0.07$
- The cdf value for a crack size of 0.00635 m was near 1

From the outcomes, the probability of a crack reaching the surface of the pipeline for complete fracture is 2.0×10^{-7} which is again a negligible probability. However, this is the probability of observing only one pit. So by repeating the earlier exercise, the probability of observing number of pits and the frequency of exceedance for each observed pit is shown below respectively,

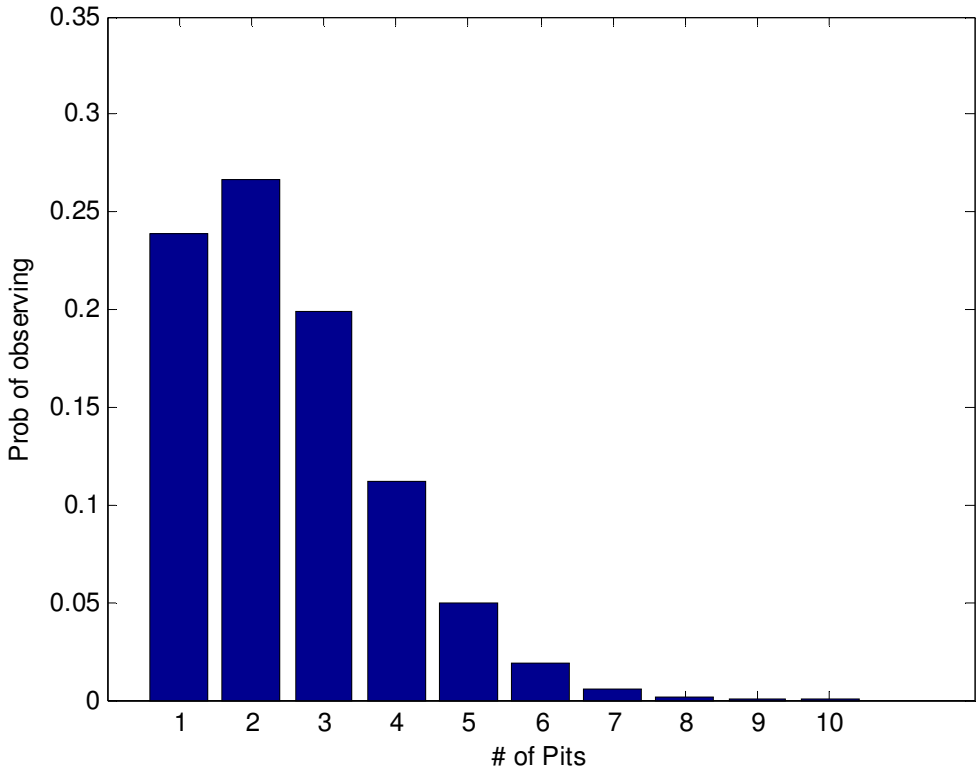

Figure 6.8. Probability of Observing Specific Number of Pits for Refinery Pipeline for Harsher Environment (High Corrosive Concentration).

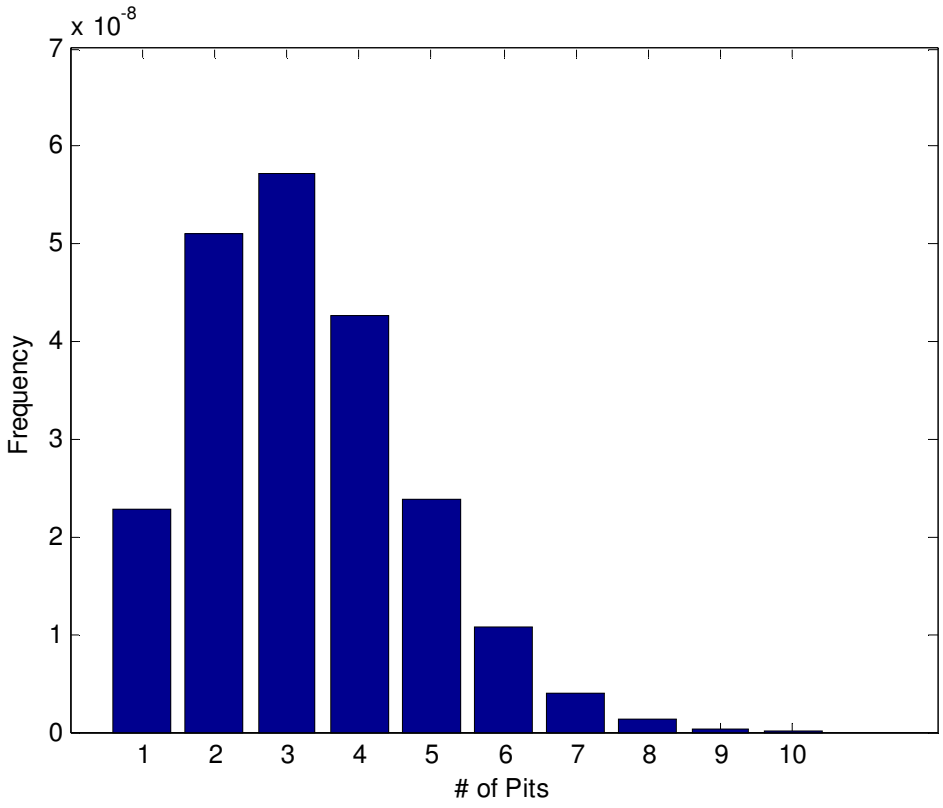

Figure 6.9. Frequency of Exceedance for Each Observed Number of Pits in the Refinery Pipeline for Harsher Environment (High Corrosive Concentration).

.

Summing the results in Figure 6.9 produces 4.48×10^{-7} as the total frequency of exceedance for all observed number of pits in the pipeline. So for a one mile long pipeline, the total frequency of exceedance for the bulk pipeline is estimated to be 0.057 pipeline failure/25 yrs life of pipeline. So, imposing a harsher environment on the pipeline had increased the probability of failure.

Consider the scenario where now the loading stress has increased to a value 1.8 MPa (18 bar). In this case, the empirical model would produce the following lognormal distribution of "a_i",

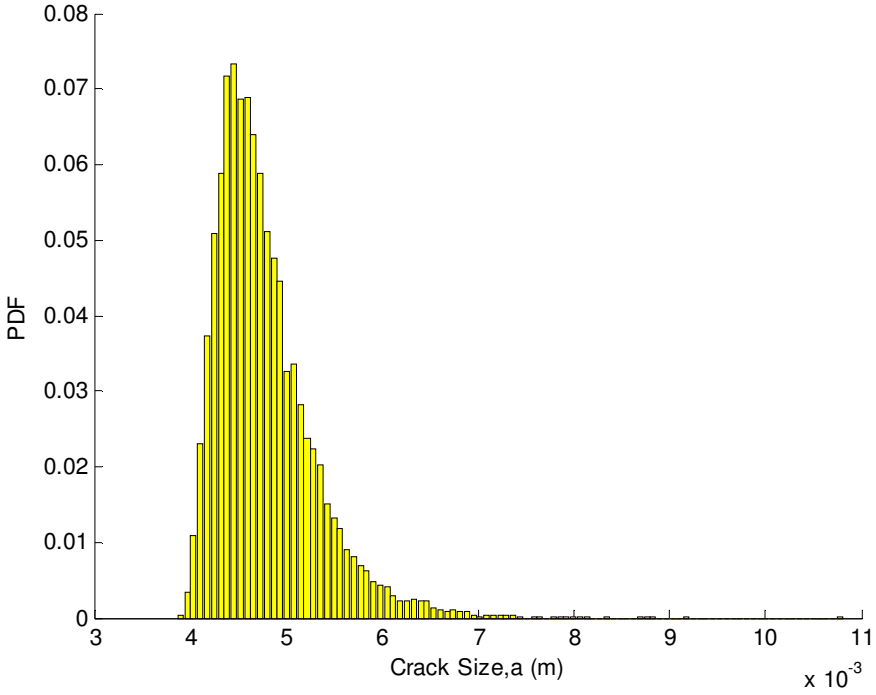

Figure 6.10. Lognormal pdf of the Crack Size "ai."

- Parameters for "ai" lognormal distribution: $\mu = -5.39$; $s = 0.1$
- The cdf value for a crack size of 0.998 m was near 1

From the outcomes, the probability of a crack reaching the surface of the pipeline for complete fracture is 0.002. However, this is the probability of observing only one pit. So by repeating the earlier exercise, the probability of observing number of pits and the frequency of exceedance for each observed pit is shown below respectively,

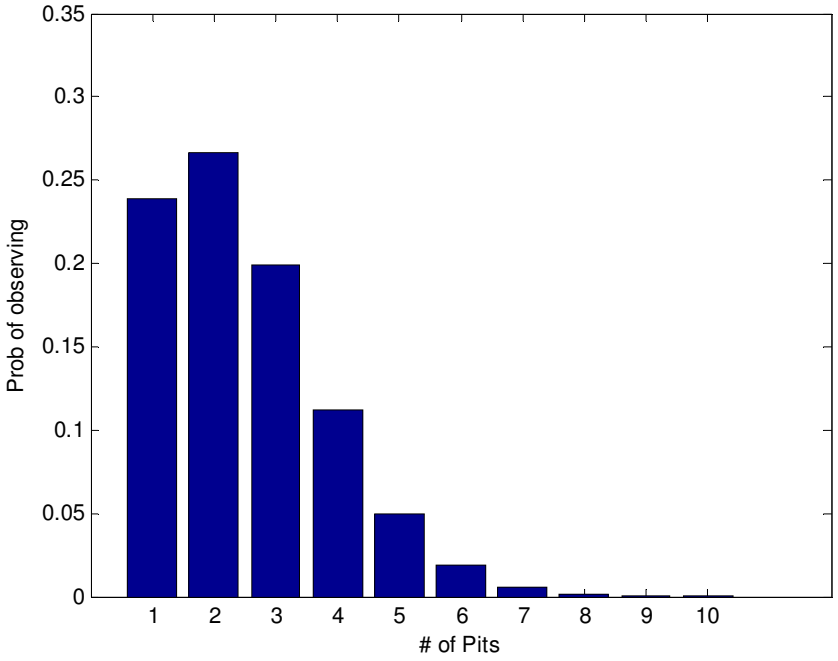

Figure 6.11. Probability of Observing Specific Number of Pits for Refinery Pipeline for Harsher Environment (High Loading Stress).

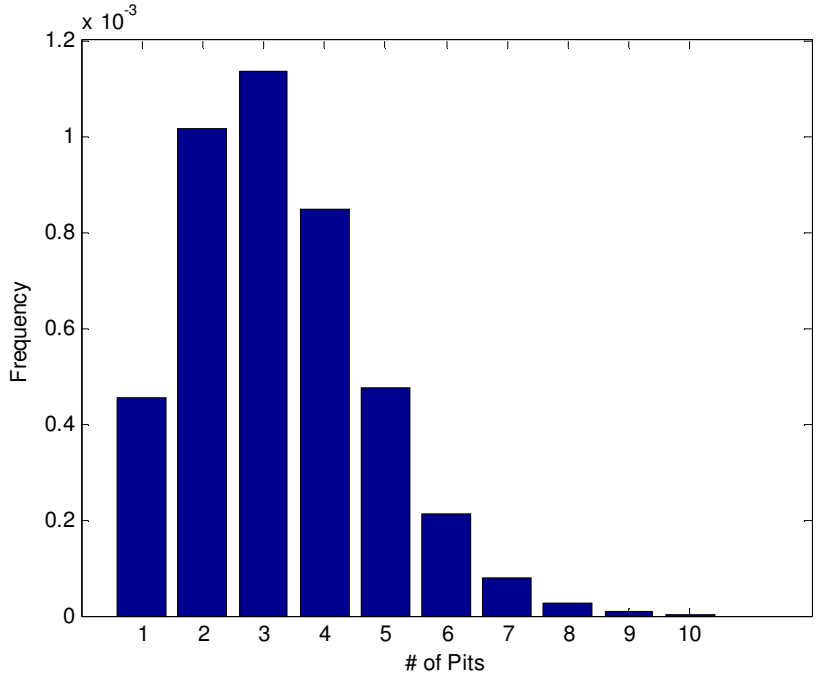

Figure 6.12. Frequency of Exceedance for Each Observed Number of Pits in the Refinery Pipeline for Harsher Environment (High Stress Loading).

Summing the results in Figure 6.12 produces 0.004 as the total frequency of exceedance for all observed number of pits in the pipeline. So for a one mile long pipeline, the total frequency of exceedance for the bulk pipeline is estimated to be 21 pipeline failure/year life of pipeline. So, imposing a harsher environment, by increasing the loading stress, on the pipeline had increased the probability of failure drastically.

6.4 *Summary*

A real example of an operating pipeline from an existing refinery has been utilized to demonstrate the practical use of the proposed empirical model. The outcomes of the simulation using the proposed empirical model had revealed satisfactory results that could be used to predict the remaining life of the pipeline with the assumption of having an aqueous medium where Cl^- and H_2S are the major contributors for corrosion. In conclusion, the proposed empirical model had successfully demonstrated it is ability to assess the life remaining of a pipeline under certain operating conditions which would assist to set appropriate inspection and maintenance preventive schemes.

CHAPTER 7

CONCLUSIONS & RECOMMENDATIONS

7.1 *Conclusions*

Pipelines in the oil industry have a long history of experiencing significant degradation processes that result in economic losses due to interrupted operation, diminished production, and increased maintenance and inspection costs. A significant factor of the pipeline degradation process is the corrosion-fatigue phenomenon. Recent results from several research activities have shown to be promising in modeling the corrosion-fatigue mechanism. The research reported in this dissertation contributes to these results by proposing a simple empirical corrosion-fatigue model which can be developed with high fidelity using experimental results. The process of pitting corrosion leading to initial crack forms the first term of the empirical model, while the second term accounts for the dominating degradation process of fatigue crack growth. The integration of these two degradation mechanism into one simple model was possible by means of utilizing a benchmark model outcome. Also, the transition point from pitting corrosion to corrosion-fatigue was identified during the phase of empirical model development which helped suggest the form of the proposed empirical model in this research.

The number of uncertain parameters was satisfactorily condensed to only two in the proposed empirical model which allowed implementing the probabilistic characterization

of them. The proposed empirical model correlated crack growth and crack size with physical and environmental stress factors of stress amplitude (due to pressure change inside the pipeline), frequency of the stress application, corrosion current, and the number of applied stress cycles. Assuming an aqueous medium flowing inside the pipeline with only Cl^- and H_2S being the major corrosive agents, it was possible to propose a closed form for the corrosion current that accounts for the temperature contribution in the degradation process both pitting and corrosion-fatigue.

Scarcity of field data directed the research efforts toward erecting a testing laboratory. Thus, an in-house state-of-art corrosion-fatigue testing was acquired to conduct the required tests and generate the data needed for estimation of the two critical parameters of the proposed empirical model. At the same time, pitting corrosion testing went in parallel to furnish the data that accounts for the first term of the empirical model. Prior to in-house equipment arrival, an outside laboratory facility capable of conducting corrosion-fatigue and pitting corrosion tests was used to independently perform similar tests. The combined data from both in-house and outside lab facilities were sufficient to estimate the two parameters.

A Bayesian approach clubbed with the concept of accelerated life was adapted to estimate the joint distribution of A and B, the uncertain parameters of the proposed empirical model. The available experimental data combined with a prior of non-informative uniform distribution for A, B, and σ (standard deviation of crack size lognormal distribution) was employed in WinBUGS (window based computer software

for MCMC) to calculate the posterior estimate of the parameters A & B. These posteriors represent the joint distributions of A, B, and *s* that accounts for both epistemic and aleatory uncertainties. Hence, Bayesian approach implemented through WinBUGS had led to the most satisfactory outcomes which coincides with the fact that dependency between A and B does exist and it was accounted for.

To demonstrate the viability of the proposed empirical model, it was essential to show its use. An existing operating pipeline in a refinery was selected and the model was used to estimate the remaining life of a typical pipeline. Hence a candidate pipeline from an existing pipeline was used to assess the applicability of the empirical model. Different operating conditions, from benign to harsh environments, were selected to asses outcomes predicted by the empirical model. In all cases, the empirical model performed satisfactorily and to predicted the expected remaining life of the pipeline in hand.

So, the proposed simple empirical model, having only two uncertain parameters, had achieved the intended objective which in turn could complement the efforts made in this research field of modeling corrosion-fatigue degradation mechanism probabilistically.

7.2 *Recommendations for Future Direction*

- More controlled tests are needed to generate more data.

- Since the corrosion current is dependent on temperature and in this research temperature was considered as a constant, one may add the aleatory variability due to temperature in the future.
- The assumption for making the n_c and n_r, the fatigue exponent and corrosion-fatigue exponent respectively, could be eased by considering them as random variables. This would be quite cumbersome in the computational analysis, but would bring the proposed empirical model closer to the realistic domain.

- The crack growth in the proposed empirical model was assumed to have a constant shape factor for the crack size distribution. Nevertheless, adopting a varying crack shape factor would enhance the outcomes of the empirical model.
- The proposed empirical model did not consider two critical processes: pit nucleation and pit-to-crack transition. These two processes are still under investigation, and a solid acceptable modeling for them has yet to be determined. To include these two processes in the proposed empirical model would mean building an almost complete empirical model that could be further developed to a physical model.
- The empirical model was mainly developed using generic data of high-strength carbon steel that is widely common in the oil and gas industry fields. In addition, the on-going tests were mainly applied to the same material due to various limiting criteria. Hence, testing the empirical model application against other ferrous and non-ferrous material used in the oil and gas industry would provide more global applications of the proposed empirical model.

- The widely acceptable superposition model of Wei had been employed as a benchmark model in the development of the empirical model. The corrosion-fatigue part of the model assumed the simplest fatigue crack model for fracture mechanics, the Paris model. The effect of the following should be considered in future:
    - Stress ratio
    - Plasticity at crack tip
    - Thickness effect
    - Limitation for small cracks
    - Sequence effects
    - Crack closure
- The corrosion current in the proposed empirical model represents the corrosion effect of two major species: chloride and sulphate. These two species were selected due to the vast acceptance in the industry of their widespread effect in many failing pipelines. However, other degrading corrosive species could be considered such as napthanic acid, oxygen, caustic, and sulphate-reducing bacteria (SRB). Though these species tend to be related to very specific applications, the resulting damage perhaps quite intense. Hence, developing empirical models tailored specifically to account for these species would help avoid failures in critical applications of oil and gas industry.
- The rotating machinery in the oil and gas industry plays a major role in sustaining the plants operation. Thus, considering the dynamics of this machinery in the modeling process would be a great life-assessment tool for the end-user.

- More advanced sensitivity analysis could be implemented to capture the correlation between the physical parameters of the pipeline.

APPENDIX A

STATIC STRESS CORROSION SPECIMEN #1 SURFACE CORROSION

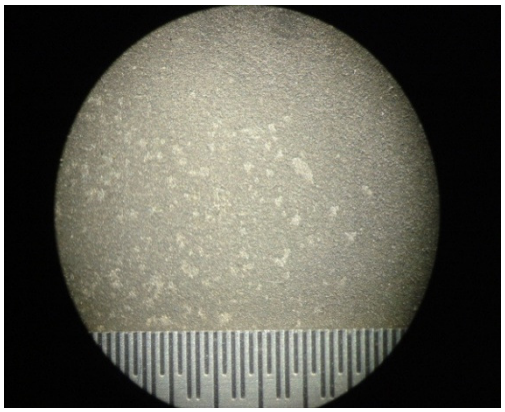

Day (5)

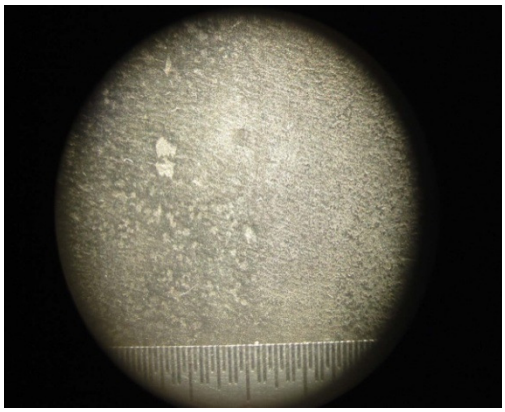

Day (13)

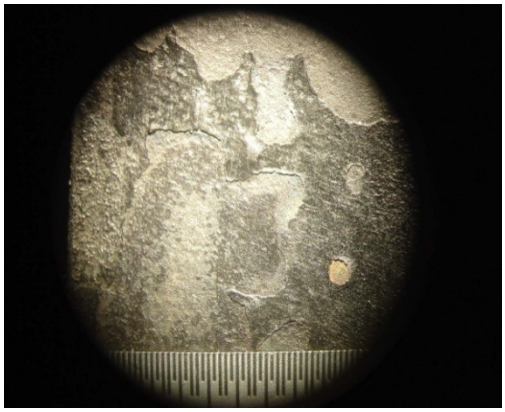

Day (20)

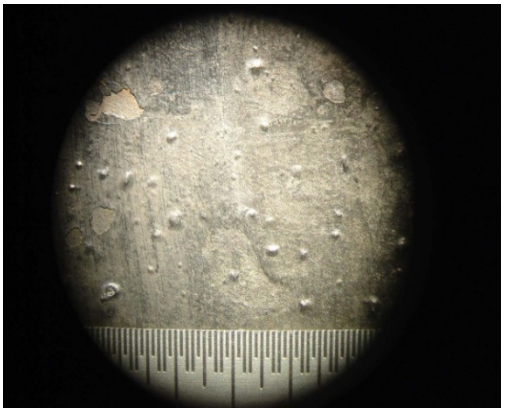

Day (27)

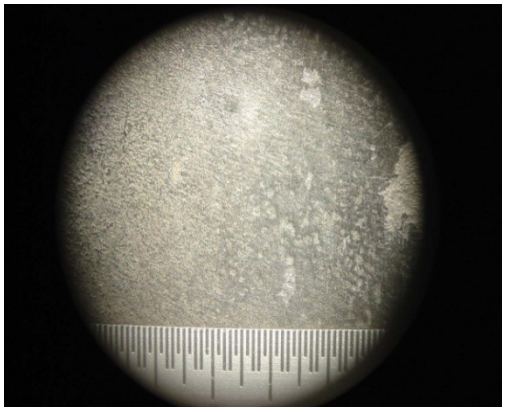

Day (34)

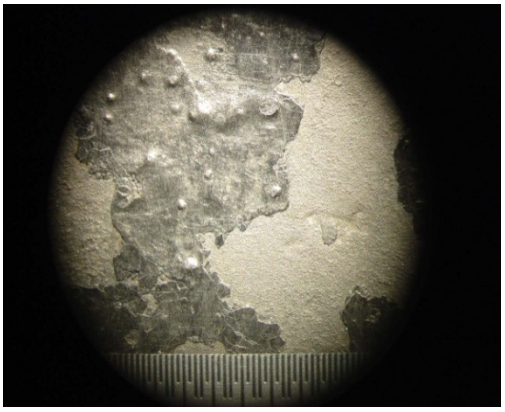

Day (40)

STATIC STRESS CORROSION SPECIMEN #2 SURFACE CORROSION

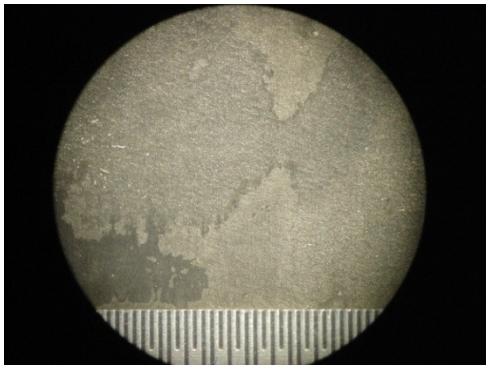

Day (5)

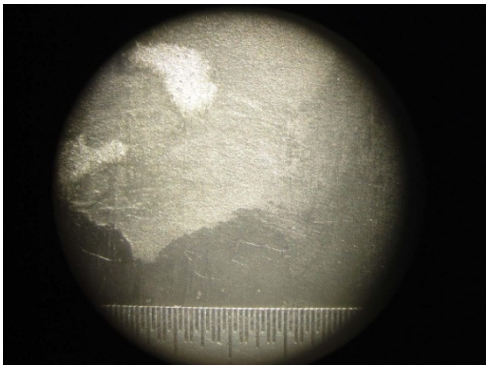

Day (13)

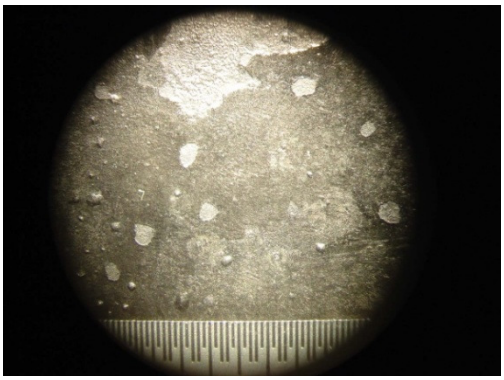

Day (20)

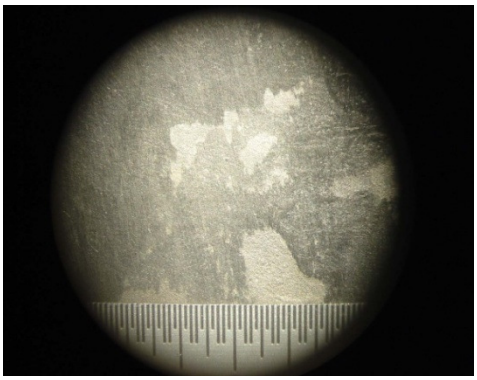

Day (27)

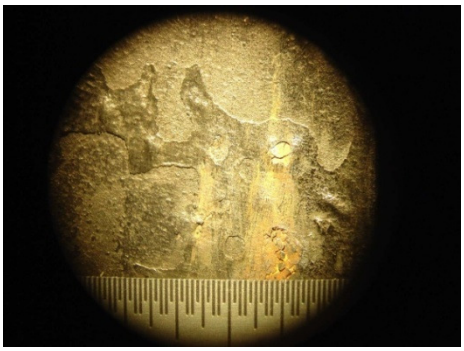

Day (34)

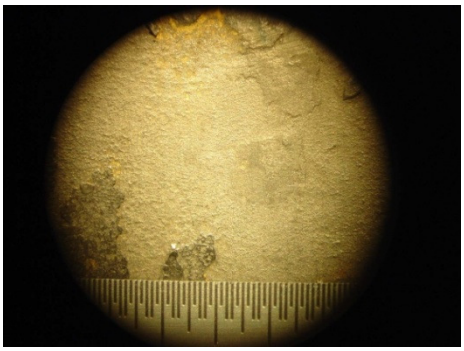

Day (40)

STATIC STRESS SPECIMEN SURFACE PIT SIZE VS. TIME

704 Corporations Park
Scotia, NY 12302
Ph.: (518) 688-2851
Fax: (518) 688-2855
url: www.its-inc.com

Innovative Test Solutions Program (081-08105)

Static Stress Sprecimen #1 Pitt size vs. Time (1/19/09-3/01/09)

X-70 in Substitute Sea Water w/ $Na_2S_2O_3$-$5H_2O$ @ 90C

Customer: Mohamed Chookah

Company: University of Maryland

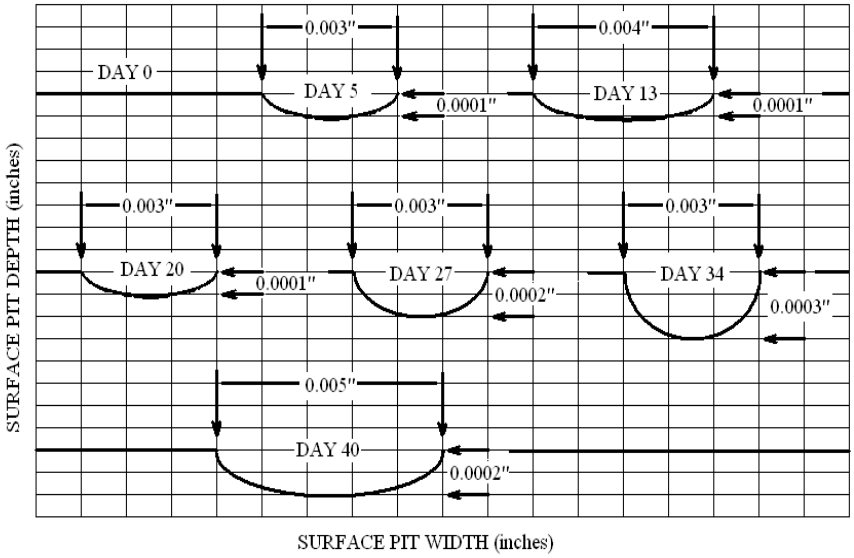

704 Corporations Park
Scotia, NY 12302
Ph.: (518) 688-2851
Fax: (518) 688-2855
url: www.its-inc.com

Innovative Test Solutions Program (081-08105)

Static Stress Sprecimen #2 Pitt size vs. Time (1/19/09-3/01/09)

X-70 in Substitute Sea Water w/ $Na_2S_2O_3$-$5H_2O$ @ 90C

Customer: Mohamed Chookah

Company: University of Maryland

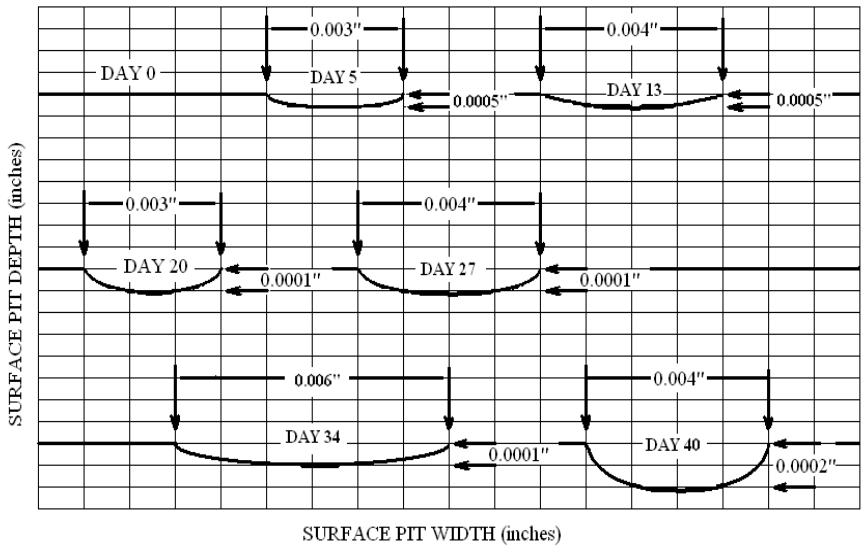

APPENDIX B

704 Corporations Park
Scotia, NY 12302
Ph.: (518) 688-2851
Fax: (518) 688-2855
url: www.its-inc.com

Innovative Test Solutions Program (081-08105)

W=0.8 CT Fatigue Crack Growth Test Data
Specimen: X-70 #6, Environment: Air
Stress Int.: 41 to 73 Kmax, Temperature: 90C
Customer: Mohamed Chookah, PhD.
Company: University of Maryland

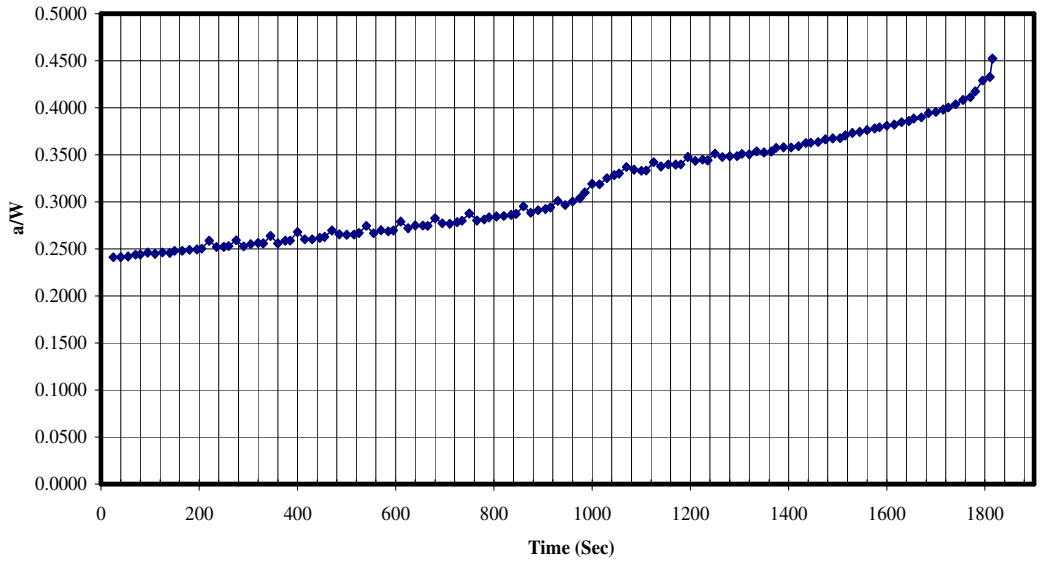

704 Corporations Park
Scotia, NY 12302
Ph.: (518) 688-2851
Fax: (518) 688-2855
url: www.its-inc.com

Innovative Test Solutions Program (081-08105)

W=0.8 CT Fatigue Crack Growth Test Data
Specimen: X-70 #6, Environment: Air
Stress Int.: 41 to 73 Kmax, Temperature: 90C
Customer: Mohamed Chookah, PhD.
Company: University of Maryland

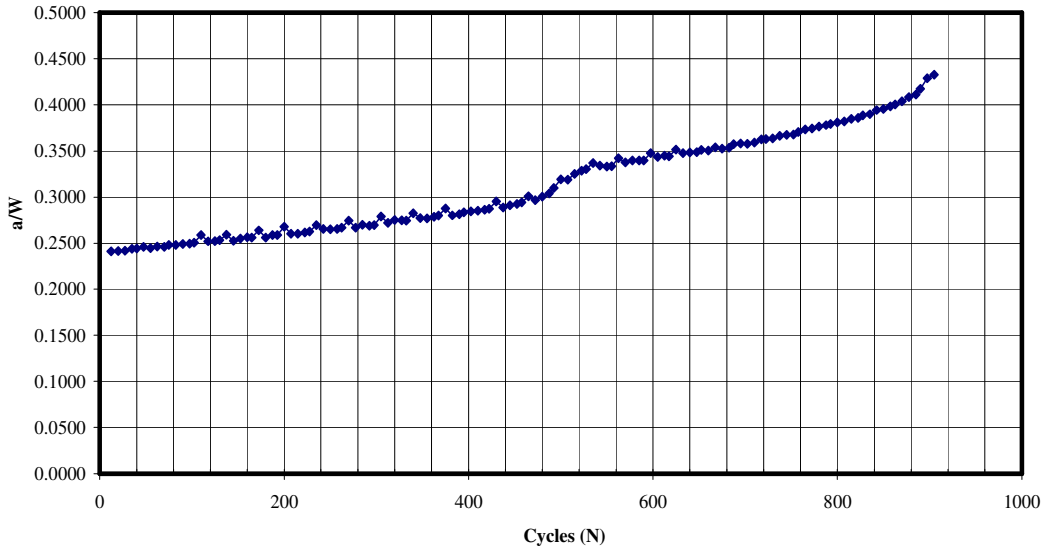

704 Corporations Park
Scotia, NY 12302
Ph.: (518) 688-2851
Fax: (518) 688-2855
url: www.its-inc.com

Innovative Test Solutions Program (081-08105)

W=0.8 CT Fatigue Crack Growth Test Data
Specimen: X-70 #6, Environment: Air
Stress Int.: 41 to 73 Kmax, Temperature: 90C
Customer: Mohamed Chookah, PhD.
Company: University of Maryland

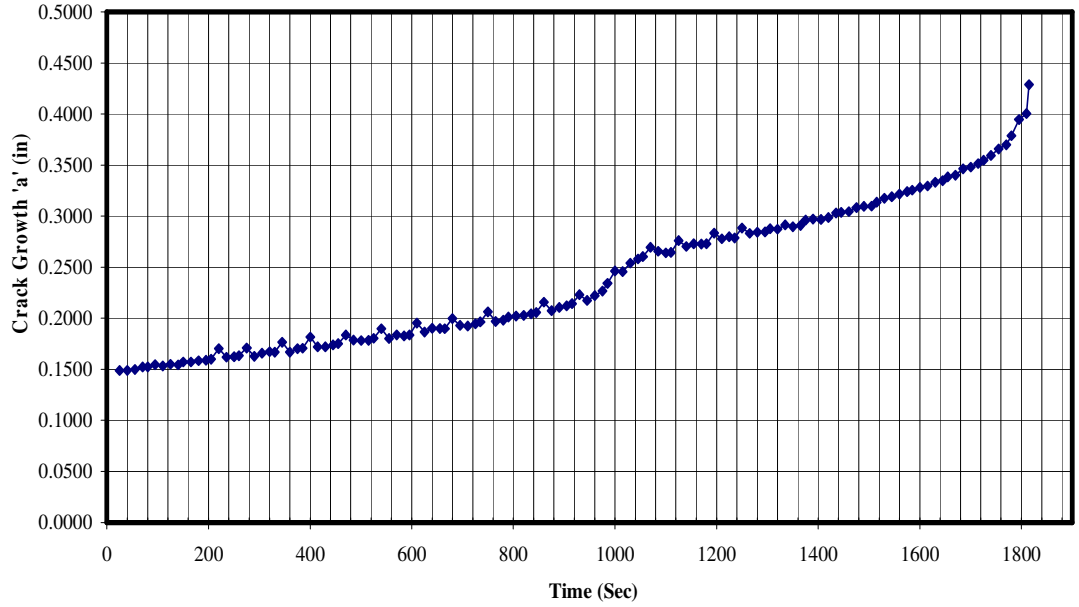

704 Corporations Park
Scotia, NY 12302
Ph.: (518) 688-2851
Fax: (518) 688-2855
url: www.its-inc.com

Innovative Test Solutions Program (081-08105)

W=0.8 CT Fatigue Crack Growth Test Data
Specimen: X-70 #6, Environment: Air
Stress Int.: 41 to 73 Kmax, Temperature: 90C
Customer: Mohamed Chookah, PhD.
Company: University of Maryland

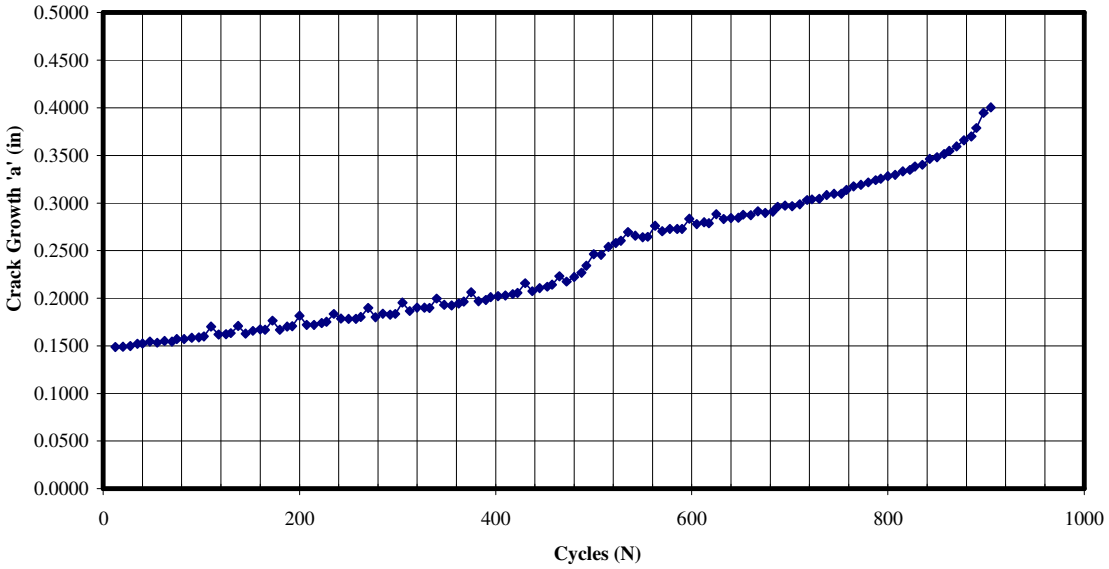

APPENDIX C

The Plot from Cortest Corrosion-Fatigue Testing System for Crack Length vs. Number of Cycles.

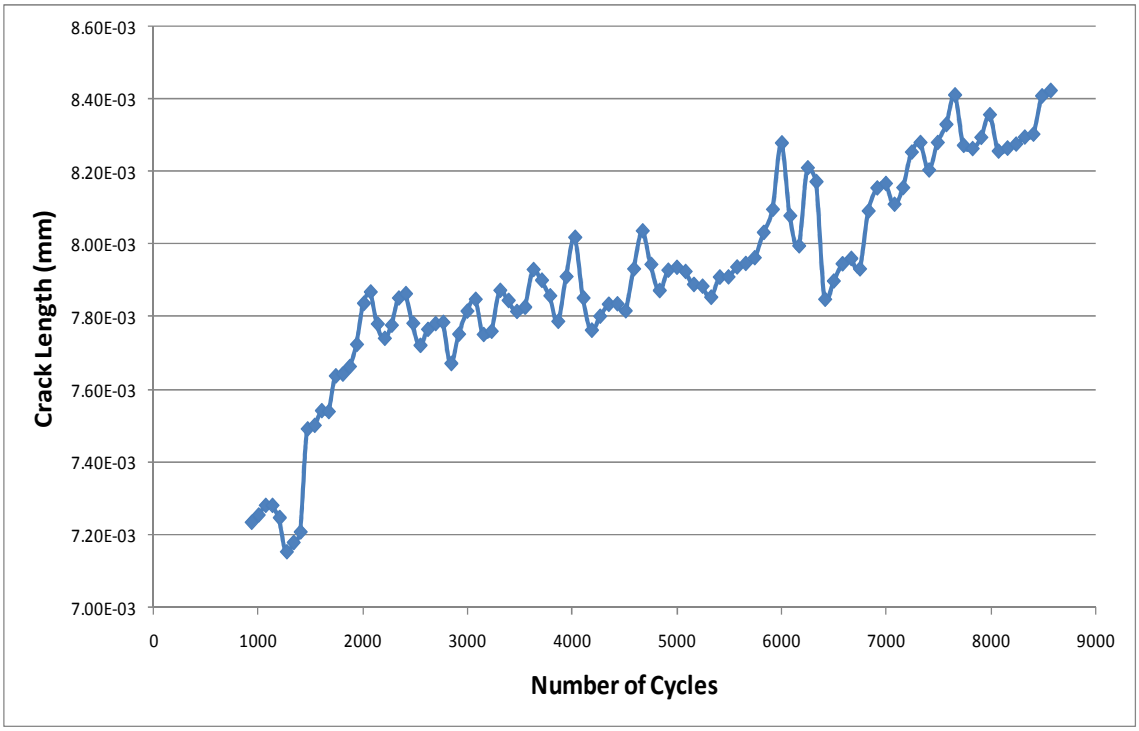

APPENDIX D

The X70 Carbon Steel Specimen Microstructure past Polishing Process at Different Magnifications.

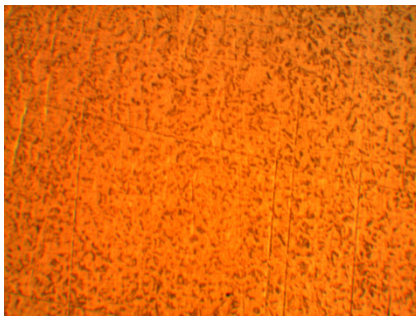

50X Magnification

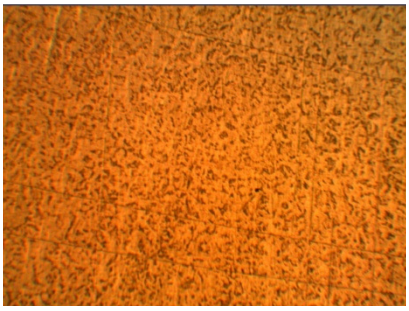

50X Magnification

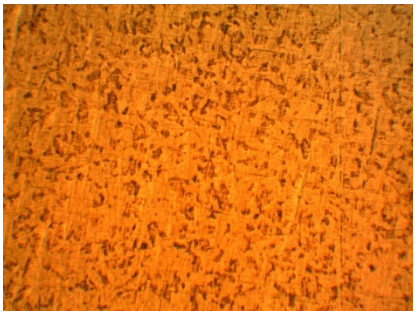

100X Magnification

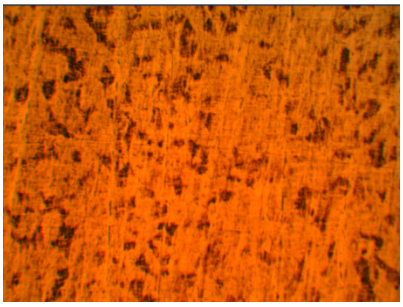

200X Magnification

200X Magnification

500X Magnification

Pitting Morphology of X70 Crbon Steel after 3Hr. at 80 ^{0} C

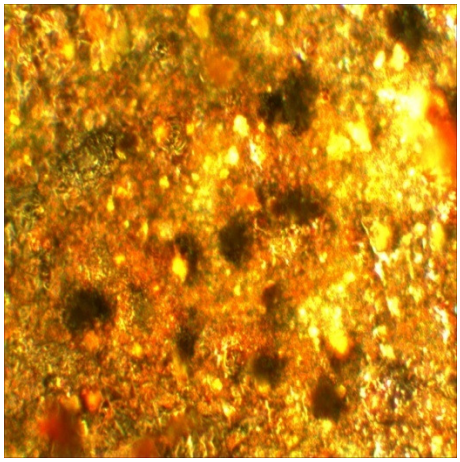

(A)

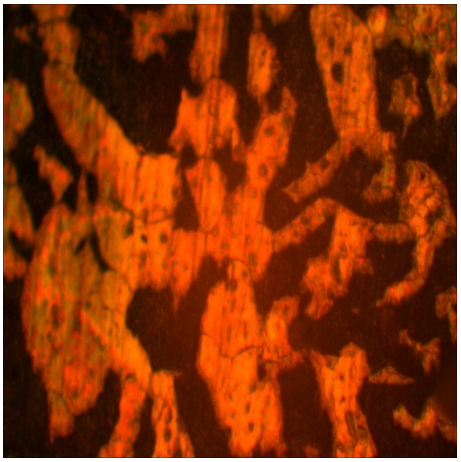

(B)

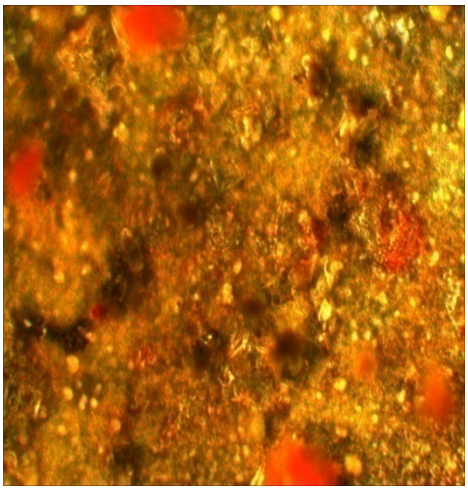

(C)

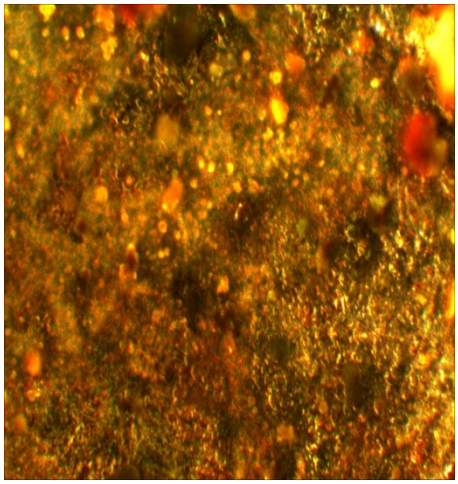

(D)

The Energy-dispersive –X-ray image (EDX) from the SEM microscope the Fe and Mn X-ray picks are given from the bottom of the pit

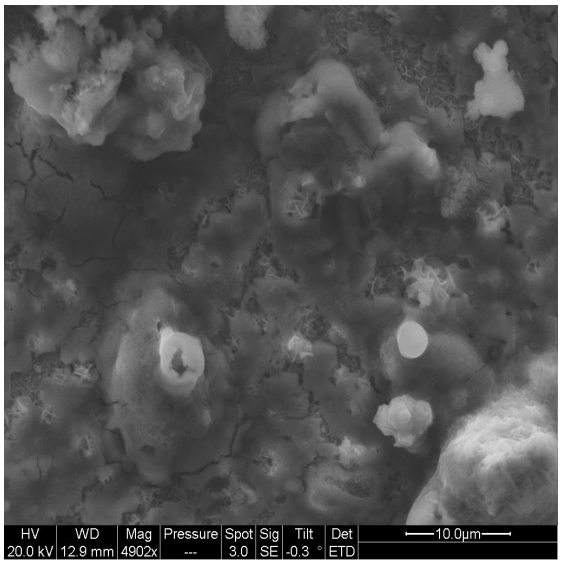

(E)

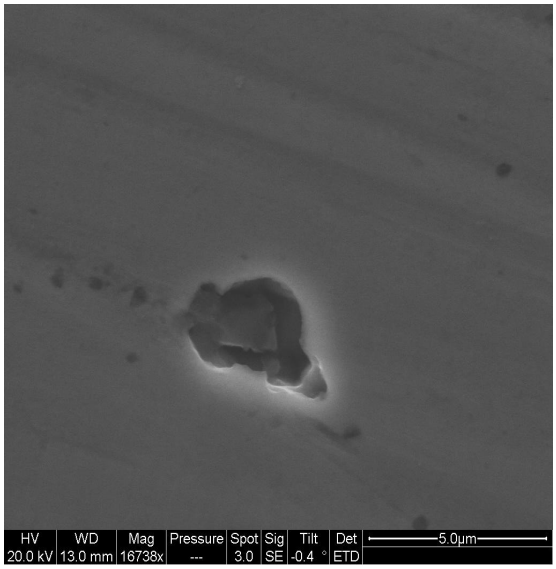

(F)

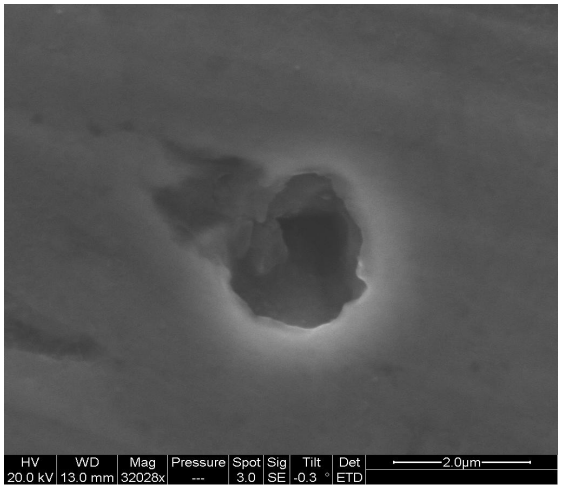

(G)

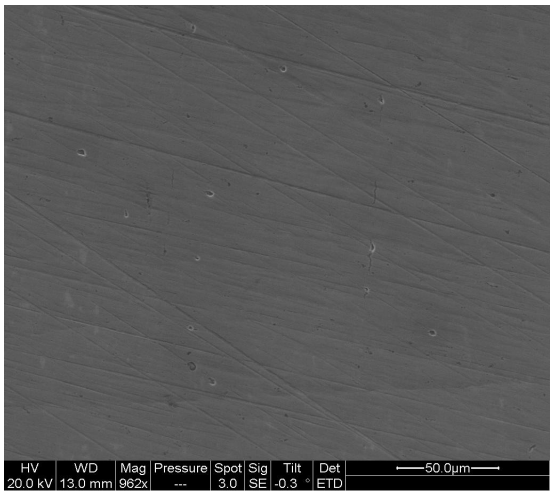

(H)

REFERENCES

[1] ASME-B31G (1991). Manual for determining the remaining strength of corroded pipelines, A supplement to ASME B31G code for pressure piping. New York: American Society for Mechanical Engineers.

[2] Lee, O. S., Kim, D. H. and Choi, S. S. (2006). Reliability of buried pipeline using a theory of probability of failure. *Solid State Phenomena*, 110, 221-230.

[3] Pandey, M. D. (1998). Probabilistic models for condition assessment of oil and gas pipelines. *NDT & E International*, 31(5), 349-358.

[4] Pereguda, A. I. and Soborova, I. A. (1999). Probabilistic model of the reliability of a Du-500 pipeline. *Atomic Energy*, 87(6), 892-898.

[5] Castaneda, H., Alamilla, J. and Perez, R. (2004). Life prediction estimation of an underground pipeline using alternate current impedance and reliability analysis. *Corrosion*, 60(5), 429-436.

[6] Sheikh, A. K., Boah, J. K. and Hansen, D. A. (1990). Statistical modeling of pitting corrosion and pipeline reliability. *Corrosion*, 46(3), 190-197.

[7] Sinha, S. K. and Pandey, M. D. (2002). Probabilistic neural network for reliability assessment of oil and gas pipelines. *Computer-Aided Civil and Infrastructure Engineering*, 17, 320-329.

[8] Caleyo, F., González, J. L. and Hallen, J. M. (2002). A study on the reliability assessment methodology for pipelines with active corrosion defects. *International Journal of Pressure Vessels and Piping*, 79, 77-86.

[9] Cagno, E., Caron, F., Manucini, M. and Ruggeri, F. (2000). Using AHP in determining the prior distribution on gas pipeline failures in a robust Bayesian approach. *Reliability Engineering and System Safety*, 67, 275-284.

[10] De Leon, D. and Macías, O. F. (2005). Effects of spatial correlation on the failure probability of pipelines under corrosion. *International Journal of Pressure Vessels and Piping*, 82, 123-128.

[11] Macdonald, D. D. (1992). "The Point Defect Model for the Passive State," *J. Electrochem. Soc.*, Vol. 139, No. 12, pp. 3434-3449.

[12] Kondo, Y. (1989). "Prediction of Fatigue Crack Initiation Life Based on Pit Growth," *Corrosion*, Vol. 45, No. 1, pp. 7-11.

[13] Hoeppner, D. W. (1971). "Corrosion-
Fatigue: Chemistry, Mechanics and Microstructure " Nace-2, p 3.

[14] Hoeppner, D. W. (1979). "Fatigue Mechanisms," ASTM Special Technical Publication No. 675, p 841.

[15] Goswami, T. K., and Hoeppner, D. W. (1995). "Pitting Corrosion-Fatigue of Structural Materials," *Structural Integrity in Aging Aircraft*, The 1995 ASME International Mechanical Engineering Congress and Exposition, AD-Vol. 47, pp. 129-134, San Francisco.

[16] Harlow, D. G., and Wei, R. P. (1995). "Probability Modeling for the Growth of Corrosion Pits," *Structural Integrity in Aging Aircraft*, The 1995 ASME International Mechanical Engineering Congress and Exposition, AD-Vol. 47, pp. 185-194, San Francisco.

[17] Chen, G. S., Wan, K.-C., Gao, M., Wei, R. P., and Flournoy, T. H. (1996). "Transition from Pitting to Fatigue Crack Growth – Modeling of Corrosion-Fatigue Crack Nucleation in a 2024-T3 Aluminum Alloy," *Material Science and Engineering*, A219, pp. 126-132.

[18] Kondo, Y., and Wei, R. P. (1989). "Approach on Quantitative Evaluation of Corrosion-Fatigue Crack Initiation Condition," *International Conference on*

*Evaluation of Materials Performance in Severe Environment*s, EVALMAT 89, Takamura, J.-I., ed., The Iron and steel Institute of Japan, Tokyo, Vol. 1, pp. 135-142.

[19] Turnbull, A., McCartney, L. N., and Zhou, S. (2006). "A Model to Predict the Evolution of Pitting Corrosion and the Pit-to-Crack Transition Incorporating Statistically Distributed Input Parameters," *Corrosion Science*, Vol. 48, pp. 2084-2105.

[20] Kawai, S., and Kasai, K. (1985). "Consideration of Allowable Stress of Corrosion-Fatigue (Focused on the Influence of Pitting)," *Fatigue Fract. Engng. Mater. Struct.*, Vol. 8, No. 2, pp. 115-127.

[21] Godard, H. P. (1960). "The Corrosion Behavior of Aluminum in Natural Waters," *Can. J. Chem. Engng.*, Vol. 138. p. 167.

[22] Ishikawa, Y. et al. (1980). "Application of Extreme Value Statistical Analysis to Actual Localized Corrosion Data from Some Operating Machine Components," *Corrosion Engng. (Boshyoku Gijitsu)*, Vol. 25, p. 502.

[23] Li, C. (1996). Probabilistic Modeling for Corrosion-Fatigue Crack Growth. *PhD Dissertation*, Lehigh University.

[24] Liu, H. W. (1963). Fatigue Crack Propagation and Applied Stress Range – An Energy Approach. *Journal of Basic Engineering*, 85, 116-122.

[25] Dowling, N. E. (1993). Mechanical Behavior of Materials. Prentice Hall, NJ.

[26] Modarres, M. (2005). Accelerated Life Testing – ENRE 641. Class Presentation Slides, University of Maryland, College Park.

[27] Paris, P. C., and Erdogan, F. (1963). A Critical Analysis of Crack Propagation Laws. *Journal of Basic Engineering*, 85, 528-534.

[28] Forman, R. G., Kearney, V. E., and Engle, R. M. (1967). Numerical Analysis of Crack Propagation in Cyclic-Loaded Structure. *Journal of Basic Engineering*, 89, 459-464.

[29] Walker, K. (1970). The Effect of Stress Ratio During Crack Propagation and Fatigue for 2024-T3 and 7075-T6 Aluminum. *Effects of Environment and Complex Load History for Fatigue Life*, *ASTM STP 462*, 1-14, Philadelphia: American Society for Testing and Materials.

[30] Hall, L. R., Shah, R. C., and Engstrom, W. L. (1974). Fracture and Fatigue Crack Growth Behavior of Surface Flaws and Flaws Originating at Fastener Holes. *AFFDL-TR-74-47, Air Force Dynamic Laboratory*, WPAFB, Ohio.

[27] Chamberlain, S., Modarres, M., and Chookah, M. (2004). " Development of a Probabilistic Mechanistic Model for Reliability Assessment of Gas Cylinders in Compressed Natural Gas Vehicles," *Proceedings of the Institution of Mechanical Engineers, Part O, Journal of Risk and Reliability*, Accepted for publishing on 12 June 2009.

[32] Gangloff, R. P. (1990). Corrosion-Fatigue Crack Propagation in Metals. Langley Research Center, NASA Contractor Report 4301, NASA.

[33] Wei, R. P., and Harlow, D. G. (1989). Mechanistically Based Probability Modeling, Life Prediction and Reliability Assessment. *Modeling and Simulation in Materials Science and Engineering*, 13, R33-R51.

[34] Gangloff, R. P. (1988). *Material Science Engineering*, A103, 157-166.

[35] Wei, R. P. (June 1987). Electrochemical Reactions and Corrosion-Fatigue Crack Growth. *Mechanical Behaviour of Materials – V*, proceedings of the Fifth International Conference, China, 129-140.

[36] Scott, P.M., Thorpe, T.W. and Silvester, D.R.V. (1983). *Corrosion Science*, Vol. 23, pp. 559-575.

[37] Gangloff, R.P. (1984). Embrittlement by the Localized Crack Environment, *TMS-AIME*, pp. 265-290.

[38] Wei, R.P., "Corrosion-Fatigue Crack Growth and Reactions with Bare Steel Surfaces", Corrosion 89, Paper No. 569, (Houston, TX: NACE, 1989).

[39] Meyn, D.A. (1971). *Met. Trans.*, Vol. 2, pp. 853-865.

[40] Austen, I.M. and Walker, E.F. (1984). *Fatigue 84*, EMAS, pp. 1457-1469.

[41] Wei, R. P., and Lands, J. (1969). Correlation between Sustained-Load and Fatigue Crack Growth in High Strength Steels. *Materials Research and Standards*, 9, 25-27.

[42] Wei, R. P., and Gao, M. (1983). Reconsideration of the Superposition Model for Environmentally Assisted Fatigue Crack Growth. *Scripta Metallurgica*, 17, 959-962.

[43] Harlow, D. G., and Wei, R. P. (1993). A Mechanistically Based Approach to Probability Modeling for Corrosion-Fatigue Crack Growth. *Engineering Fracture Mechanics*, 45, 1, 79-88.

[44] Jones, R. H. (1992). Stress-Corrosion Cracking, Materials Performance and Evaluation. ASM International, Materials Park, Ohio.

[45] Logan, H. L. (1952). *J. Res. Natl. Bur. Stand.*, Vol. 48, p. 99.

[46] Staehle, R. W. (1971). "Theory of Stress Corrosion Cracking in Alloys," North Atlantic Treaty Organization, p. 223.

[47] Staehle, R. W. (1977). "Stress Corrosion Cracking and Hydrogen Embrittlement of Iron Based Alloys," *NACE*, p. 180.

[48] Ford, F. P. (1988). *J. Press. Ves. Tech. Trans. ASME*, Vol. 110, pp. 113-128.

[49] Ford, R. P. (1984). "Embrittlement by the Localized Crack Environment," R. P. Gangloff, ed., (Warrendale, PA: TMS-AIME), pp. 117-147.

[50] Hudak, S. J. (1988). "Corrosion-Fatigue Crack Growth: The Role of Crack-Tip Deformation and Film Formation Kinetics," PhD Dissertation, (Bethlehem, PA: Lehigh University).

[51] Ford, F. P., and Andresen, P. L. (1989). "Advances in Fracture Research," K. Salema, K. Ravi-chandor, D.M.R. Taplin, and P. Ramo Rao, eds., (Oxford, UK: Pergamon Press), pp. 1571-1584.

[52] Ford, F. P. (1990). "Environment Induced Cracking of Metals," R. P. Gangloff and M.B. Ives, eds. (Houston, TX: NACE), pp. 139-166.

[53] Wei, R. P. (2002). Environmental Considerations for Fatigue Cracking. *Fatigue & Fracture of Engineering Materials & Structures*, 25, 8/9, 845-854.

[54] Harlow, D. G., and Wei, R. P. (2001). Life Prediction – The Need for Mechanistically Based Probability Approach. *Key Engineering Materials*, 200, 119-138.

[55] Lin, Y. K., and Yang, J. N (1983). On Statistical Moments of Fatigue Crack Propagation. *Engineering Fracture Mechanics*, 18, 243-256.

[56] Bogdanoff, J. L., and Kozin, F. (1985). Probabilistic Models of Cumulative Damage. Wiley and sons, NY.

[57] Sheikh, A. K., Boah, J. K., and Hansen, D. A. (1990). Statistical Modeling of Pitting Corrosion and Pipeline Reliability. *Corrosion*, 46, 3, 190-197.

[58] Caleyo, F., González, J. L., and Hallen, J. M. (2002). A Study on the Reliability Assessment Methodology for Pipelines with Active Corrosion Defects. *International Journal of Pressure Vessels and Piping*, 79, 77-86.

[59] Hall, P. L., and Strutt, J. E. (2003). Probabilistic Physics-of-Failure Models for Component Reliabilities Using Monte Carlo Simulation and Weibull Analysis: A Parametric Study. *Reliability Engineering and System Safety*, 80, 233-242.

[60] Strutt, J. E., Hall, P. E., and Allsopp, K. (2000). Unpublished work. *Reliability Engineering and Risk Management Center at Cranfield University*, UK.

[61] Goswami, T. K., and Hoeppner, D. W. (1997). "Review of Pit Nucleation, Growth, and Pitting Corrosion-Fatigue Mechanism," *Journal of Mechanical Behavior of Materials*, Vol. 8, No. 2, pp. 169-196.

[62] Harlow, D. G., and Wei, R. P. (1994). Probability Approach for Prediction of Corrosion and Corrosion-Fatigue Life. *AIAA Journal*, 32, 10, 2073-2079.

[63] Liao, C. M., et al (1998). In Situe Monitoring of Pitting Corrosion in a 2024 Aluminum Alloy. *Corrosion*, 54, 451-458.

[64] Atkins, P. W. (1994). Physical Chemistry. W. H. Freeman and Company, NY.

[65] Luis Manual Quej-Ake, et al. "EIS study of corrosion process of 1018 carbon steel in acid solutions typical of atmospheric distillation plants" www.electrochem.org/meetings/scheduler/abstracts/210/0848.pdf

[66] Crude Unit Overhead Corrosion page, www.setlaboratories.com/Overhead.htm.

[67] Distillation, SET Laboratories, Inc. www.setlaboratories.com/distilla.htm.

[68] Gutzeit, J., Merrick, R. D., and Scharfstein, L. R. "Corrosion in Petroleum Refining and Petrochemical Operations". Metals Handbook, ASM International, 9 Ed., Vol 13, Metals Park, OH.

[69] Jayaraman, A., and Saxena, R. C. "Corrosion and its Control in Petroleum Refineries – a Review". Corrosion Prevention & Control. pp 123-131. December 1995. Dehradun, India.

[70] Chen, H.N, Chen, . L.S., Lin, Q.H., and Long, X. (1999). *Corrosion*, **55**, p. 626.

[71] Pardo, A. Otero, E., Merino, M.C., López, M.D., Utrilla, M.V., and Moreno, F. (2000). *Corrosion*, **56**, p. 411.

[72] Romero, M., Duque, Z., Rincón, O., Pérez, O., Araujo, I., and Martinez, A. (2000). *Corrosion*, **56**, p. 867.

[73] Singh, I.B. (2001). *Corrosion*, **57**, p. 483.

[74] Laitinen, T. (2000). *Corros. Sci.* **42**, p. 421.

[75] Gabetta, G. (1997). *Corrosion*, **53**, p. 516.

[76] Yamakawa, K., and Nishimura, R. (1999). *Corrosion*, **55**, p. 24.

[77] Sierra, R.C., Sosa, E., Oropeza, M.T., and González, I. (2002). *Electrochim. Acta*, **47**, p. 2149.

[78] Carneiro, R.A., Ratnapuli, R.C., and Lins, V.F.C. (2003). *Mater. Sci. Eng. A*, **357**, p. 104.

[79] Omweg, G.M., Frankel, G.S., Bruce, W.A., Ramirez, J.E., and Koch, G. (2003). *Corrosion*, **59**, p. 640.

[80] Moraes, F.D., Bastina, F.L., and Ponciano, J.A. (2005). *Corros. Sci.*, **47**, p. 1325.

[81] Ren, C., Liu, D., Bai, Z., and Mater, T. Li. (2005). *Chem. Phys.*. **93**, p. 305.

[82] Kuzyukov, A.N., Nikhayenko, Y.Y., Levchenko, V.A., Borisenko, V.A., and Moisa, V.G. (2005). *Int. J. Hydrogen Energy*, 27, p. 813.

[83] Chen, Y.Y., Liou, Y.M., and Shih., H.C. (2005). "Stress corrosion cracking of type 321 stainless steels in simulated etrochemical process environments containing hydrogen sulfide and chloride," *Materials Science and Engineering*, A 407, pp. 114–126.

[84] Gutzeit, J. (2000). Effect of Organic Chloride contamination of Crude Oil on Refinery Corrosion. *Corrosion*, Paper No. 00694. www.nace.org/nacestore/assets/ConferencePapers/2000/00694.pdf

[85] Lin, C. J., et,al. Scanning Microelectrode Studies of Early Pitting Corrosion of 18/8 Stainless Steel, Corrosion, Vol 54, No.4, pp.265-270.

[86] Chapter 9. Pitting Corrosion, KAIST, http://corrosion.kaist.ac.kr

[87] Andijani, I.,et.al. (1999). Studies on corrosion of carbon steel in deaerated saline solutions in presence of scale inhibitor. Presented at the WSTA IV Golf Conference, Bahrain.

[88] Petek, A., et.al. (2007). Localized Dissolution Kinetics of Low Carbon Steel. *Acta Chim Slov*. 54, pp 725-729.

[89] Huisert, M. Electrochemical Characterization of Filiform. Corrosion on Aluminium Rolled Products. www.iospress.nl/html/9789040722363.php

[90] Joseph, C., Farmer, et.al. (1997) Crevice Corrosion & pitting of High-Level Waste Containers: Integration of Deterministic & Probabilistic Models, UCRL _JC_127980 Part 1.

[91] Mack, L.P., et.al. (1984). "Effect of Bromide Ions on the Electrochemical Behavior of Iron," *Corrosion*, Vol.40, No.5.

[92] Brossia, C.S., and Cragnolino, G.A. (2000). "Effect of Environmental Variables on localized Corrosion of Carbon Steel," *Corrosion*, Vol. 56, No. 5, pp.505-514.

[93] Szklarska-Smialowska Z. (1986). Pitting Corrosion of Metals, Houston, TX: NACE international.

[94] Mathieson, T., Nielsen, T. S., and Frantsen, J. E. (2006). "Influence of Various Surface Conditions on Pitting Corrosion. Resistance of Stainless Steel Tubes Typ e EN 1.4404," Presented at NACE International 2006, Paper No. 06095, San Diego, CA. http://www.force.dk/NR/rdonlyres/CBD67CC0-DB4C-427C-A15F-4396FB8F4B05/0/061201_pittingcorrosion.pdf

[95] Hucinska, J. "Influence of Sulphur on High Temperature Degradation of Steel Structures in the Refinery Industry" www.pg.gda.pl/mech/kim/AMS/012006/AMS01200602.pdf

[96] Snape, E. (1967). "Sulfide Stress Corrosion of Some Medium and Low Alloy Steels," *Corrosion*, pp.154-172.

[97] Sardisco, J. B., et.al. (1965). "Corrosion of iron in an H_2S-CO_2-H_2O system composition and protectiveness of the sulfide film as a function of pH," *Corrosion*, Vol. 21, pp. 350-354.

[98] Autolab Application Note. www.ecochemie.nl, www.autolabj.com/appl.files/appl%20note/appl014.pdf

[99] Ma, H.Y., Cheng, X. L., Chen, S. H., Li, G. Q., Chen, X., Lei, S. B., and Yang, H. Q. (1998). "Theoretical Interpretation on Impedance Spectra for Anodic Iron Dissolution in Acidic Solutions Containing Hydrogen Sulfide," *CORROSION*, **54**, No. 8.

[100] Lauvstad, G. Ø. (2007). "Breakdown in Passivity of Austenitic Stainless Steels in Cl^- AND H_2S – Modelling and Characterization of the Pot Initiation Process," *NACE Corrosion*, Paper No.07660.

[101] Wei, S., and Nesic, S. (2007). "A Mechanistic Model of H_2S Corrosion of Mild Steel," *NACE Corrosion*, Paper No. 07655.

[102] Noris_Dover Compnay. www.norrisrods.com/failure_09.asp

[103] Laitinen, T. (1999). "Thiosulfate pitting corrosion of stainless steels in the paper machine environment," VTT Technical research center of Finland , ESPOO.

[104] Lin, L. F., Chao, C. Y., and Macdonald, D. D. (1981). *J. Electrochem Soc*., 128, pp. 1194.

[105] Zuili, D., Broyce, G., and Rabiniaux (2005). "A case history of environmental cracking in sour service Sulphide-Chloride Stress Corrosion Cracking on 316L stainless steel," Paper No. O-698L, Eurocorr.

[106] Kounaves ,S. P. Voltammetric Techniques, Tufts University, Department of Chemistry, www.prenhall.com/settle/chapters/ch37.pdf

[107] Cyclic Voltammetry, www.potentiostat.com/tech/apn_cyclic.shtml

[108] Cells d Electrodes for Use with Potentiostats, www.bank- ic.de/en/zellen-e.html

[109] Electrochemical Measurement of Corrosion: www.edaq.com/Teaching_Application_4_Electrochemistry_-_Electrochemical_Measurement_of_Corrosion.html

[110] Lu, B.T., and Luo, J.L. (2005). "Crack initiation and early propagation of X70 steel in simulated near neutral pH groundwater," C*orrosion*, Vol. 62,No.8,2005.

[111] Fang, B. and et.al. (2005). "Mechanical and Environmental Influences on Stress Corrosion Cracking of an X70 Pipeline Steel in Dilute Near-Neutral pH Solutions," *Corrosion*, Vol. 63, No. 5.

[112] Yang, R. and et.al. (2006). "comparison of Corrosion Behavior of X70 and 16 Mn Steels, III. Corrosion-Erosion," Corrosion Science and Protection Technology, Vol. 18, No. 1.

[113] Crooker, and Leis. "Corrosion-Fatigue Mechanics, Metallurgy, Electrochemistry & Engineering - STP 801", *ASTM Publication*, pp. 408-409.

[114] Wei, R. P., and Speidel, M. O. (1972). "Phenomenological Aspects of Corrosion-Fatigue," *Corrosion-Fatigue: Chemistry, Mechanics, and Microstructure*, NACE-2, pp. 379-380.

[115] Derungs, W. A. (1956). "Naphthanic Acyd Corrosion – and Old Enemy of the Petroleum Industry," *Corrosion*, Vol. 12, pp. 617t-622t.

[116] Sorel, G., and et.al. "Collection and Correlation of High Temperature Hydrogen Sulfide corrosion Data," NACE 12th Annual Conference, The M.W. Kellogg Co., New York, N. Y.

[117] Ghosh, D. P. (2007). "Wet H2S Cracking Problem in Oil Refinery Processes – Material Selection and Operation Control Issues," *Tri Service Corrosion Conference*. http://www.corrdefense.org/Technical%20Papers/Wet%20H2S%20Cracking%20Problem%20In%20Oil%20Refinery%20Processes-Material%20Selection%20and%20Operation%20Control%20Issues.pdf

[118] NACE RP 0472 (2000): Methods and Controls to Prevent In- Service Environmental Cracking of Carbon Steel Weldments in Corrosive Petroleum Refining Environments.

[119] Vosikovsky, O. (1975). *J. Eng Mater Technol*, Trans ASME 97H, pp. 298–304.

[120] Truchon, M., and Rabbe, P. (1983). Mem etud Sci Rev Metall 80, pp. 117–130.

[121] Schmelzer, F., Schmitt, F.J., and Werkstofftech, Z. (1981). Vol. 3, pp. 90–96.

[122] Nakasa, K., Takei, H., and Kajiwara, K. (1981). *Eng Fract Mech*, Vol. 14, pp. 507–517.

[123] Venegas, V. (2007). " Role of Crystallographic Texture in Hydrogen- Induced Cracking of Low Carbon Steels for Sour Service Piping ," Metallurgical and Material Transaction A, Vol. 38, No. 5, pp. 1022-1031.

[124] Brickell, W.F., and et.al. "Corrosion of iron in H_2S-CO_2-H_2O system: influence of (single iron) crystal orientation on hydrogen penetration rate.

[125] Hoeppner (1971). Corrosion Doctors, http://corrosion-doctors.org/Journal-2000/No3/No3-table-2.htm.

[126] Cerny, I. (2004). "The use of DCPD Method for Measurement of Growth of Cracks in Large Components at Normal and Elevated Temperatures," *Engineerin g Fracture Mechanics*, 71, 837–848.

[127] Johnson, H. H. (1965). "Calibrating the Electric Potential Method for Studying Slow Crack Growth," *Mater Res Stand,*5(9), 442–5.

[128] Tada, H., Paris, P. C., Irwin, G. R. (1973). The Stress Analysis of Crack Handbook. Hellertown, Pensylvania: Del Research Corporation.

[129] The 3rd International Symposium on Supercritical Water-Cooled Reactors – Design and Technology (2007). Shanghai, China. *nsse.sjtu.edu.cn/.../1%20Stress%20Corrosion%20Crack%20Growth%20in%2031*

[130] Das, S. K. "Materials Solutions for Hydrogen Delivery in Pipelines" , *www1.eere.energy.gov/hydrogenandfuelcells/pdfs/pipeline_group_das_ms.pdf*

[131] Johnson, J. T. et al (2000). "Effects of O_2 and CO_2 on Near-Neutral-pH Stress Corrosion Crack Propagation", *corrosion*, No. 00356.

[132] ASTM Standard E 647-88a, "Standard Test Method for Measurement of Fatigue Crack Growth Rates."

[133] Cortest Operating Manual (2008).

[134] ASTM Standard G39-99.

[135] Williams,D.E.et al. (1991). Nature 350, 216.

[136] Park , J.O.et.al. (2002). "Effects of Temperature and Chloride Concentration on Pit Initiation and Early Pit Growth of Stainless Steel," *J. of the Electro. Chem. So ciety*, 149(2), pp. B34-B39.

[137] ASTM Standard G46-94.

[138] Modarres, M. (1999). Reliability Engineering and Risk Analysis A Practical Guide. Marcel Dekker, NY.

[139] Sander, P., and Badoux, R. (1991). Bayesian Methods in Reliability. Kluwer Academic Publishers. Dordrecht, Netherlands.

[140] Brooks, S. P. (1998). "Markov Chain Monte Carlo Method and its Application,"*The statistician*, Royal Statistical Society, Vol. 47, No. 1, pp. 69-100.

[141] Spiegelhalter, D., Thomas, A., Best, N., and Lunn, D. (2003). WinBUGS 1.4 Manual.

[142] Azarkhail, M., and Modarres, M. (2007). "A Noval Bayesian Framework for Uncertainty Management in Physics-Based Reliability Models," *Proceedings of IMEC2007*, 2007 ASME International Mechanical Engineering Congress and Exposition, Seattle, Washington, USA.

[143] Azarkhail, M., and Modarres, M. (2007). "Markov Chain Monte Carlo Simulation for Estimating Accelerated Life Model Parameters," *Annual Reliability and Maintainability Symposium (RAMS) Proceedings*, Orlando, FL, USA.

[144] Vosikovsky, O., and Cooke, R. J. (1978). "An Analysis of Crack Extension by Corrosion-Fatigue in a Crude Oil Pipeline," *Int. J. Pres. Ves. & Piping*, 6, pp. 113-129.